# Quantifying Endplate Deflection in Response to Cyclic Load Exposures Using a Porcine Cervical Spine Model

by

Michael Watson

A thesis

presented to the University of Waterloo

in fulfillment of the

thesis requirement for the degree of

Master of Science

in

Kinesiology

Waterloo, Ontario, Canada, 2025

© Michael Watson 2025

**Author's Declaration**

I hereby declare that I am the sole author of this thesis. This is a true copy of the thesis, including any required final revisions, as accepted by my examiners. I understand that my thesis may be made electronically available to the public.

## Abstract

The vertebral endplate is a thin layer of cartilage and bone that separates the intervertebral disc from adjacent vertebral bodies and facilitates the transmission of compressive force through the spine. Despite this essential function, it remains the weakest component of the vertebra-disc unit and is highly susceptible to mechanical failure. Endplate failure typically arises from localized tensile strains that manifest as deflection, defined as the out-of-plane displacement of the surface under load. While prior work has demonstrated inferior endplates of intervertebral joints exhibiting greater deflection and higher incidence of failure than their superior counterpart, current techniques for quantifying endplate deflection face notable limitations.

Early studies using metallic markers or displacement transducers required drilling channels into the vertebral body, potentially exaggerating deformation by weakening subchondral bone support. Imaging-based approaches, particularly micro-CT, offer high spatial resolution but are limited to static or stepwise loading due to temporal constraints. These static conditions do not capture the cyclic loading patterns experienced by the spine during daily activity, where repeated deformation can cause fatigue-induced microdamage and eventual failure. Additionally, static loading promotes excess fluid loss from the nucleus pulposus, altering endplate deflections in ways that do not reflect physiological motion. Consequently, existing measurement techniques may misrepresent true endplate behavior and are unable to evaluate changes in deflection as a function of cyclic load exposure. This study addresses these limitations by developing a unique method to assess endplate deflection during cyclic loading without requiring prolonged stepwise protocols or causing damage to the vertebral bone. By comparing superior and inferior endplates across different load magnitudes and cyclic durations, this work aims to clarify the mechanisms

underlying endplate vulnerability and further validate the porcine cervical spine as an experimental model for human lumbar spine deflection.

Eighteen porcine cervical spine functional units (C3C4, C4C5, and C5C6; n = 6 per level) were dissected to yield 36 individual vertebrae. High-resolution laser profilometry was then used to capture the topography of the caudal endplates of C3, C4, and C5 and the cranial endplates of C4, C5, and C6. Custom indenters, designed as negative molds of the nucleus-occupying endplate region, were created from the resulting surface scans and fabricated via 3D printing. Specimens were then oriented such that the tested endplate was in a neutral position and subjected to a normalized haversine waveform, ranging from 0.3 kN to 30% of the predicted ultimate compressive strength using a servohydraulic materials testing system. The cycle-dependent changes in endplate deflection were measured at 0, 1000, 3000, and 5000 total cycles. At each time point, endplate deflection measurements were captured via the indenter's displacement while specimens were exposed to a brief static force of 0.3 kN, 1 kN, and 3 kN, totaling 12 measurements per vertebra. Three separate linear mixed effects models were used to evaluate the impact of loading magnitude, loading cycles, endplate level and the proportion of the nucleus occupying endplate area on superior and inferior endplate deflection within each joint. A fourth linear mixed effects model was used to evaluate the impact of loading magnitude, loading cycles, and joint level on the magnitude of the differences between superior and inferior endplate deflection.

Utilizing this novel methodology, this study was the first to quantify endplate deflection under cyclic loading conditions, observing greater deflection of the inferior endplate across all spinal levels, except at baseline (0.3 kN, 0 cycles). This method also enabled comparison of deflection rates between endplates, with the C4C5 and C5C6 inferior endplates showing a significantly greater rate of deflection during the first 1000 cycles. Among joints, C4C5 exhibited

the largest difference in superior and inferior endplate deflection compared to C3C4 and C5C6. Endplate deflection was not influenced by the proportion of the nucleus occupying endplate area at any spinal level. Lastly, as the first study to examine endplate deflection in porcine cervical vertebrae, the observation of greater inferior endplate deflection being consistent with human cadaveric studies further supports the validity of this model. Overall, this study demonstrates the utility of a novel methodology for measuring and comparing superior and inferior endplate deflection under cyclic loading.

## Acknowledgements

I would like to sincerely thank my supervisor, Dr. Jack Callaghan, for being an outstanding mentor. From day one, it was clear you want nothing but the best for your students. You have never hesitated to provide guidance, especially during my occasional "quarter life crises", and your wisdom has helped me navigate both graduate school and personal challenges. Your calmness and sense of humour never get old, and I always feel better after having a meeting with you. Having asked you for a job as an undergraduate student was one of the best decisions I have made as you have not only taught me the scientific process but also how to approach life with curiosity and purpose.

Thank you, Drs. Nikolas Knowles and Clark Dickerson, as members of my committee. Your feedback and difficult questions have helped shaped this project for the better.

A big thank you to Dr. Jackie Zehr. Since my time as an undergraduate research assistant, you have been a constant source of inspiration, motivating me to strive for excellence. Your mentorship has been integral to my personal growth and I certainly would not have achieved even a fraction of my successes had it not been for your generosity.

Thank you to my lab mates and fellow graduate students for your support, positivity, and for showing me research is not just for nerds. It is full of hardworking, passionate, and genuinely fun people: Jessa Davidson, Justin Davidson, Lia Tennant, Brendan Pinto, Erinn McCreath Frangakis, Juliana Bossom, Kate Krivenko, Dylan Munn, and Adam Russin.

Thank you, Alica Nadon, for always promptly answering my panicked administrative related emails; Emma Dare, for procuring the copious number of things I request from Amazon (and Dr. Jack Callaghan, for approving it all); and Jeff Rice, for letting me constantly bother you to borrow tools and equipment.

Thank you to my parents Maria and Ian, my older sisters Chelsea and Sabrina, and the small pack of dogs we call pets (Mia, Pepper, Bri, and Yuki). I would be nothing without the foundation my family provides me and I am so fortunate to have such loving and caring people in my life.

Thank you to my good friend Dan Mateescu, who has always been there for "emergency tech support" and being a source of passion and creativity in my life. Thank you to Amy Lui and Brayson Cancel for acting as a family away from home.

Thank you to my wonderful partner, Lisa, for your endless love and support. Whether it's a weekly catastrophe involving my project or an existential crisis about the meaning of life, you have always been there for me. Your unwavering kindness and love have helped me overcome countless personal challenges and I am lucky to have you in my life.

I am thankful to have received funding from federal and provincial sources and am privileged to have had the opportunity to pursue an education with this support.

# Tables of Contents

List of Figures ..... ix

List of Tables ..... xi

List of Equations ..... xiii

Chapter 1 - Introduction ..... 1

1.1 Research Questions and Hypotheses ..... 4

Chapter 2 - Literature Review ..... 6

2.1 Intervertebral Disc Anatomy ..... 6

2.2 Viscoelastic Behavior of the Vertebral Endplate ..... 7

2.3 Porous Properties and Poroelastic Behaviour of the Vertebral Endplate ..... 8

2.4 Anatomical Factors Contributing to Discrepancies in Superior and Inferior Endplate Failure ..... 9

2.5 Comparative Impacts of Static and Cyclic Loading on Spinal Microdamage and Endplate Deflection ..... 11

2.6 Previous Approaches to Measuring Endplate Deflection ..... 14

Chapter 3 - Methods ..... 19

3.1 Overview of Study Design ..... 19

3.2 Specimens ..... 19

3.3 Specimen Preparation ..... 23

3.4 Surface Profilometry ..... 26

3.5 Indenter Modelling ..... 28

3.6 Indenter Fabrication ..... 30

3.7 Measurement Correction ..... 32

3.8 Cyclic Loading Protocol ..... 36

3.9 Statistical Analysis ..... 42

Chapter 4 – Results ..... 45

4.1 C3C4 Endplate Deflections ..... 45

4.2 C4C5 Deflections ..... 48

4.3 C5C6 Deflections ..... 52

4.4 Effect of Joint Level ..... 56

Chapter 5 - Discussion ..... 59

5.1 Comparison to Previously Measured Values ..... 59

5.2 The Validity of Assessing Injury Risk Through Endplate Deflection Patterns ..... 63

5.3 The Effects of Joint Level on Endplate Deflection ..... 64
5.4 The Limited Role of Nucleus-Endplate Contact Area ..... 67
5.5 Implications for the Validity of the Porcine Cervical Spine Model ..... 68
5.6 Experimental Cost and Accessibility Considerations ..... 69
5.7 Orthopedic Applications ..... 70
5.8 Limitations ..... 71
5.9 Sources of Curiosity and Future Avenues of Research ..... 74
Chapter 6 – Conclusions ..... 76
References ..... 78
Appendices ..... 86

## List of Figures

**Figure 2.5.1**: Loading protocol for FSUs used by Hulme et al., 2008 ..... 17

**Figure 2.5.2:** "Experimental procedure for mechanical testing and imaging." (Jackman et al., 2014) ..... 18

**Figure 3.2.1**: Illustration of endplate level terminology ..... 21

**Figure 3.2.2**: Schematic of tested endplate. ..... 22

**Figure 3.3.1**: Comparative images of specimen glare: without cornstarch (left) and with cornstarch (right). ..... 25

**Figure 3.3.2**: Non-testing endplate cleaned of cartilage and soft tissue in preparation to interface with potting ..... 25

**Figure 3.3.3**: Representative image of the positioning of image markers on the specimen surface. ..... 25

**Figure 3.3.4**: Specimen wrapped in saline-soaked gauze ..... 26

**Figure 3.4.1**: Custom constructed laser profilometry setup. ..... 27

**Figure 3.4.3**: The three-point leveling mechanism ensures the scan remains square relative to the specimen's surface. ..... 28

**Figure 3.5.1**: Example of a manually defined nuclear region of the endplate ..... 29

**Figure 3.5.2**: Sample of an indenter model generated from a 3D scanned endplate surface. ..... 29

**Figure 3.6.1**: Comparison in fidelity between the modelled and fabricated indenter ..... 31

**Figure 3.6.2**: Endplate of specimen loaded within the central region to failure (Right) using a non-representative indenter (Middle and Left) ..... 31

**Figure 3.6.3**: Verification of central endplate–indenter contact via ink transfer ..... 32

**Figure 3.7.1**: 6 mm diameter spherical marker affixed to the anterior surface of the specimen's epiphyseal plate ..... 35

**Figure 3.7.2**: Custom constructed laser profilometry setup interfacing with the material testing system apparatus ..... 35

**Figure 3.8.1**: A. Metallic Fixture, B. Indenter ..... 39

**Figure 3.8.2**: Normalized Haversine waveform representative of the force time pattern during a moderate demand repeated lifting task ..... 39

**Figure 3.8.3**: Nucleus load-pressure relationship (Peng et al., 2011) ..... 40

**Figure 3.8.4**: Automated static-ramp and scanning protocol ..... 40

**Figure 3.8.5**: Schematic of Cyclic Loading Protocol ..... 41

**Figure 4.1.1**: C3C4 endplate deflections measured throughout the experimental process. ..... 46

**Figure 4.1.2**: Estimated marginal means of C3C4 endplate deflection across loading cycles (0, 1000, 3000, 5000) at each loading magnitude (0.3, 1, and 3 kN) for visualizing differences in the rate of deflection. ..... 47

**Figure 4.2.1**: C4C5 endplate deflections measured throughout the experimental process with 95% confidence intervals. ..... 50

**Figure 4.2.2**: Estimated marginal means of C4C5 endplate deflection across loading cycles (0, 1000, 3000, 5000) at each loading magnitude (0.3, 1, and 3 kN) for visualizing differences in the rate of deflection. ..... 51

**Figure 4.3.1**: C5C6 endplate deflections measured throughout the experimental process with 95% confidence intervals. ..... 54

**Figure 4.3.2**: Estimated marginal means of C5C6 endplate deflection across loading cycles (0, 1000, 3000, 5000) at each loading magnitude (0.3, 1, and 3 kN) for visualizing differences in the rate of deflection. ..... 55

**Figure 4.4.1**: Comparison of differences in endplate deflections across C3C4, C4C5, and C5C6 joints with 95% confidence intervals. ..... 58

**Figure 5.1**: Interpolation of mean endplate deflection ..... 62

**Figure 5.3**: Superior and inferior endplate thicknesses and subchondral trabecular bone density. ..... 66

## List of Tables

**Table 3.1**: Sample Indenter Cyclic Load Calculation Table. ..... 41

**Table 3.2**: Sample Indenter Static Load Calculation Table. ..... 41

**Table 4.1**: Average Endplate Areas, Nucleus Area, Proportion of Nucleus Occupying Area, and Applied Force Magnitudes of superior C3 and inferior C4 endplates ..... 48

**Table 4.2**: Rate of change in deflection between superior C3 and inferior C4 endplates at differing cycle increments ..... 48

**Table 4.3**: Average Endplate Areas, Nucleus Area, Proportion of Nucleus Occupying Area, and Applied Force Magnitudes of superior C4 and inferior C5 endplates ..... 52

**Table 4.4**: Rate of change in deflection between superior C4 and inferior C5 endplates at differing cycle increments. *** ($p < 0.001$) * ($p < 0.05$) ..... 52

**Table 4.5**: Average Endplate Areas, Nucleus Area, Proportion of Nucleus Occupying Area, and Applied Force Magnitudes of superior C5 and inferior C6 endplates ..... 56

**Table 4.6**: Rate of change in deflection between superior C5 and inferior C6 endplates at differing cycle increment. *** ($p < 0.001$) ** ($p < 0.01$) ..... 56

Blank cells indicate no significance. ..... 56

**Table 5.1**: Comparison of Hulme et al.'s endplate deflection measurements at 1 and 1.75 kN with the present study's estimated endplate deflection at 0 cycles. ..... 62

**Table 8.1**: Outputs of linear mixed effects model comparing superior and inferior endplate deflection in the C3C4 joint. ..... 86

**Table 8.2**: Pairwise comparisons between endplates of the C3C4 joint within each loading magnitude × cycle combination (Tukey-adjusted) ..... 87

**Table 8.3**: Pairwise comparisons of changes in deflection between superior C3 and inferior C4 endplates across loading magnitudes and consecutive cycle intervals (Tukey-adjusted). ..... 88

**Table 8.4**: Outputs of linear mixed effects model comparing superior and inferior endplate deflection in the C4C5 joint. ..... 89

**Table 8.5**: Pairwise comparisons between endplates of the C4C5 joint within each loading magnitude × cycle combination (Tukey-adjusted) ..... 90

**Table 8.6**: Pairwise comparisons of changes in deflection between superior C4 and inferior C5 endplates across loading magnitudes and consecutive cycle intervals (Tukey-adjusted). ..... 91

**Table 8.7**: Outputs of linear mixed effects model comparing superior and inferior endplate deflection in the C5C6 joint. ..... 92

**Table 8.8**: Pairwise comparisons between endplates of the C5C6 joint within each loading magnitude × cycle combination (Tukey-adjusted)..... 93

**Table 8.9**: Pairwise comparisons of changes in deflection between superior C5 and inferior C6 endplates across loading magnitudes and consecutive cycle intervals (Tukey-adjusted)..... 94

**Table 8.10**: Outputs of linear mixed effects model comparing magnitude of differences between endplate of C3C4, C4C5, and C5C6 joints..... 95

**Table 8.11**: Pairwise comparisons of endplate deflection between joints for each magnitude × cycle combination (Tukey-adjusted)..... 96

## List of Equations

**Equation 1**: Formulaic representation of endplate deflection in this experimental protocol..... 35

**Equation 2**: Nuclear Stress to load conversion equation based on indenter area ..... 41

# Chapter 1 - Introduction

The vertebral endplate is a thin layer of cartilage and bone that separates the intervertebral disc from adjacent vertebral bodies (Agur & Dalley, 2017). The daily and traumatic stresses imposed on the spine facilitate endplate deflection, which aids in the transmission of compressive force. Despite this important function, the endplate is the thinnest and weakest element of the vertebra-disc unit, rendering it vulnerable to mechanical failure (Ferguson & Steffen, 2003; Perey, 1957). Previous literature has shown that within spinal joints, the inferior endplate experiences a higher incidence of failure compared to its superior counterpart (Fujiwara et al., 2019; Ortiz & Bordia, 2011). However, the mechanism for this discrepancy is still not fully understood.

While endplate failure arises from localized tensile strains within the structure (Fields et al., 2010; Zehr, Watson, et al., 2023), these tissue level-events are revealed by gross endplate deflection (Jackman et al., 2014). Deflection is the deviation from a reference point, reflecting both local deformation and bending of a structure relative to its static outer boundaries. Prior studies have noted that within spinal joints, the inferior endplate displays a greater tendency for deflection (Hulme et al., 2008; Jackman et al., 2014) which may partly explain variations in injury incidence (Fujiwara et al., 2019; Ortiz & Bordia, 2011). However, current methods for measuring this deformation have notable limitations. Some approaches have involved the implantation of metallic markers or displacement transducers beneath the centre of the endplate, which require channels to be bored through the adjacent vertebral body (Brinckmann et al., 1983; Holmes et al., 1993). While these techniques provide direct measurements, they also risk overestimating deflection due to localized removal of subchondral trabecular bone which provide essential structural support to the endplate. Alternatively, some studies have opted for imaging technologies, particularly micro-CT, given its minimally invasive nature and high spatial resolution (Hulme et al., 2008; Jackman et al.,

2014). Yet, these approaches are also constrained by their reliance on static mechanical testing and step wise loading, which are necessary due to the highly limited temporal resolution of micro-CT. Consequently, these existing methods may not fully capture the dynamic loading conditions that are typical of daily activity given there are clear differences in how static and cyclic loading influence load distribution patterns and mechanical properties within the joint (Lambers et al., 2013; Masuoka et al., 2007; McMillan et al., 1996).

Specifically, cyclic loading has been shown to play a significant role in the development of endplate injury due to its tendency to induce fatigue failure through repeated deflection. Unlike static loading, cyclic loading continuously aggregates microdamage causing for a progressive weakening in the structure over time (Zehr, Quadrilatero, et al., 2023; Zehr et al., 2024). With the vertebral endplate being composed of a cartilaginous layer and an underlying bony layer, micro damage transpires as the gradual separation between these layers (Zehr, Rahman, et al., 2022). Further, the underlying trabecular bone experiences fissures and collapse in the matrix composing the structure with repeated load exposure (Lambers et al., 2013; Wenzel et al., 1996). The cyclic paradigm thus offers a unique opportunity to observe how superior and inferior endplate deflection evolves with repeated load exposure. Another key distinction lies in the impact of long-term static loading which induces a progressive loss of fluid in the nucleus pulposus. Given the nucleus is largely responsible for applying stresses to the central region of adjacent endplates, reductions in fluid pressure relate to a decrease in endplate deflection (McMillan et al., 1996; van Dieën et al., 2001). Fluid loss of spinal joints is not exclusive to static loading, as it also occurs in cyclic contexts (Gooyers et al., 2012; Masuoka et al., 2007). However, existing literature has primarily measured endplate deflection using extended static loading protocols which theoretically, cause greater fluid loss from the nucleus pulposus than would occur under cyclic loading of equivalent

duration and load magnitude. This is because cyclic loading induces an accumulation of microdamage, which can compromise spinal joint integrity more readily than static loading under similar loading parameters. As a result, statically loaded joints are better able to maintain their integrity and survive longer under sustained loads, which allows for greater fluid loss compared to cyclically loaded joints. Of course, the relationship between joint fluid levels and loading type is also strongly influenced by the magnitude of applied force and displacement. Regardless, there is strong reason to believe that current endplate measurements may not accurately represent deflections occurring under physiologically relevant loading conditions.

While deflection has traditionally been studied under fixed static loads, evaluating deflection in response to varying cyclic load exposures offers an arguably more practical and relevant approach for assessing endplate mechanical behaviour. Consequently, critical gaps remain in understanding how endplate deflection relates to load magnitude and cumulative exposure, as well as how deflection trajectories of these structures evolve and differ over repeated cycles. Further, despite the porcine cervical spine acting as a widely used surrogate for the human lumbar spine, the specifics as to whether endplate deflections of this model mimic the human spine remain unknown and are yet to be explored. As a result, this work will contribute to our knowledge of the validity of the model in this respect. Lastly, there is a need for the development of non-invasive methodologies of the vertebral body that enable the studying of the effects of cyclic loading duration on the absolute changes in endplate deflection. Ultimately, these findings may provide insights into the design of intervertebral disc implants for improving their long-term efficacy and success.

### 1.1 Research Questions and Hypotheses

1. Within a spinal joint, comprising two adjacent vertebrae and the intervening intervertebral disc, how does both the absolute and rate of change in deflection differ between superior and inferior endplates under cyclic loading conditions?

**Hypothesis**: At each increment of cyclic and static load exposure, the inferior endplate is expected to exhibit greater deflection compared to the superior endplate. The inferior endplate is also hypothesized to display a higher rate of change in deflection between all increments of cyclic loading. This prediction aligns with its notably higher incidence of failure (Fujiwara et al., 2019; Ortiz & Bordia, 2011) and is supported by prior studies comparing endplate deflections under static loading conditions (Hulme et al., 2008; Jackman et al., 2014). Previous work has suggested that inferior endplates exhibit reduced thickness and less robust trabecular support compared to superior endplates (Zhao et al., 2009), which contribute to their mechanical vulnerability. However, the extent to which these differences manifest as deflection under cyclic loading has not been fully characterized. By examining this relationship in response to cyclic loading, the present study aims to determine whether the same asymmetry in endplate deflection persists when subjected to repeated loading cycles, thereby providing further insight into the mechanical basis of endplate vulnerability.

2. How does joint level influence the difference between superior and inferior endplate deflection?

**Hypothesis**: The most central joint (C4C5) will display greater differences between superior and inferior endplate deflections compared to C3C4 and C5C6 joints. Previous literature reports that superior bony endplates tend to thicken toward the lower lumbar levels, whereas inferior

endplates remain relatively uniform in thickness (Zhao et al., 2009). As a result, the discrepancies in endplate deflections are likely driven by variations in strength of the superior endplate. While middle level superior endplates have only a moderate thickness, the bone mineral density of this endplate is more pronounced at centrally positioned joints (Wang et al., 2011). Together, these anatomical factors suggest that central joints may exhibit greater asymmetry in deflection between superior and inferior endplates under mechanical loading.

3. Is the nucleus occupying area, when normalized relative to endplate size, a risk factor for increased endplate deflection?

**Hypothesis:** A greater proportion of the nucleus-occupying region relative to the total endplate area will lead to a reduction in deflection. The integrity of the endplate is non-homogeneous, with certain regions, particularly the center, being more prone to failure (Grant et al., 2001; Zhao et al., 2009). Consequently, despite applied loads being normalized to the nucleus-occupying region to maintain constant stress across specimens, a larger nuclear region relative to the total endplate area allows more stress to be distributed to the stronger peripheral regions of the endplate. This distribution is hypothesized to reduce overall endplate deflection.

# Chapter 2 - Literature Review

## 2.1 Intervertebral Disc Anatomy

The intervertebral disc is an anatomical structure situated between vertebrae, providing spinal flexibility and vertebral load distribution. Each disc consists of three main components: the nucleus pulposus, annulus fibrosus, and vertebral endplates. The nucleus pulposus, located at the disc's center, is a gel-like substance rich in proteoglycans and water, allowing it to absorb and redistribute compressive loads (Cassidy et al., 1989; Hickman et al., 2022). During loading, increased pressure within the nucleus is managed through bulging of the annulus fibrosus and deflection of the vertebral endplates (Brinckmann et al., 1983).

The vertebral endplates, thin structures interfacing the disc from the vertebral bodies, consist of two distinct layers: a cartilaginous and bony portion (Agur & Dalley, 2017; Crump et al., 2023). The cartilaginous layer, located directly adjacent to the nucleus pulposus and annulus fibrosus, is primarily composed of hyaline cartilage. Beneath the cartilaginous layer lies the bony endplate, which is a thin, porous layer of subchondral bone closely integrated with the vertebral body (Velnar & Gradisnik, 2023). Together, these layers play a critical role in distributing compressive stresses from fluid pressure generated from the nucleus while also facilitating nutrient diffusion between the vascularized vertebral body and the largely avascular disc (Xiang et al., 2024). Deflection of the endplate is primarily resisted by the underlying trabecular network, with literature demonstrating this subchondral structure being a large determinant of endplate failure (Jackman et al., 2014; Zehr, Watson, et al., 2023). The cortical shell of the vertebra may also experience deformation during compressional load, but is relatively minor compared to the central trabecular structures (Hulme et al., 2008).

## 2.2 Viscoelastic Behavior of the Vertebral Endplate

Similar to most organic tissues, the vertebral endplate possesses viscoelastic properties, meaning it exhibits both elastic and time-dependent viscous behavior when subjected to mechanical loading (MacLean et al., 2007; Zehr et al., 2020). Under load, the endplate initially deforms elastically, but if the applied stress exceeds its yield strength, it begins to deform plastically over time. This time-dependent deformation is characterized by creep, where the endplate gradually deforms under a constant stress, and stress relaxation, where the stress exerted by the tissue decreases as it adjusts to a fixed strain. The time-dependent mechanical response of the endplate also influences its stiffness in relation to the load rate. At higher load rates, the structure exhibits increased stiffness because the viscous components of the material have less time to respond. As a result, molecular rearrangements are reduced and deformation of the solid matrix is slowed due to internal friction. Hysteresis is another key feature of the endplate's viscoelastic behavior, where the loading and unloading curves do not overlap (Twomey & Taylor, 1982). This energy loss during cyclic loading results in residual deformation, indicating inefficiency in energy recovery and highlighting the irreversible nature of some endplate deformations under repetitive loading. Over time, repetitive loading can induce microdamage in the endplate (Zehr, Quadrilatero, et al., 2023; Zehr et al., 2024), contributing to plastic deformation and fatigue failure. This plasticity stems from the gradual accumulation of structural changes within the tissue, particularly in the solid matrix. As microdamage accumulates, the endplate becomes increasingly susceptible to further deformation, diminishing its ability to return to its original shape.

## 2.3 Porous Properties and Poroelastic Behaviour of the Vertebral Endplate

The porosity of the endplate enables the diffusion of material between the avascular intervertebral disc and the vascularized vertebral body. Permeability of the endplate varies depending on the structure's region with higher values typically found in the central areas aligned with the nucleus pulposus and lower values in the periphery (Nachemson et al., 1970; Zehra et al., 2015). The cartilaginous layer primarily governs the permeability of the endplate structure given its greater impermeability compared to its bony counterpart (Sampson et al., 2019; Wong et al., 2019). This collagen based structure is described as poroelastic, meaning its mechanical properties are influenced by the changes in the distribution of fluid contained within its porous solid matrix (Lee & Teo, 2004). In the context of the spinal endplate, this implies the cartilaginous layer responds to mechanical loading through a combination of solid deformation and fluid movement within its porous structure. Under low compressive forces, fluid is relatively free to exit the tissue. However, as compressive strains increase, the interstitial spaces in the cartilage decrease causing interstitial fluid to experience greater drag forces ultimately reducing the tissue's permeability (Lee & Teo, 2004; Mow et al., 1984; Wu et al., 2016). This impaired ability for fluid exchange increases the apparent stiffness of the endplate, making it more susceptible to failure under subsequent deformations, especially during dynamic or high rate loading (Watson et al., 2024). In addition to mechanical loading, factors such as aging and intervertebral disc degeneration significantly influence endplate permeability. Evidence suggests a relationship between reduced permeability of the cartilaginous endplate and disc degeneration severity (DeLucca et al., 2016). This decline is thought to be driven by anatomical changes such as calcification of the cartilaginous layer (Bernick & Cailliet, 1982; Roberts et al., 1996) or thickening and increased density of the endplate's collagen content (Ashinsky et al., 2020).

## 2.4 Anatomical Factors Contributing to Discrepancies in Superior and Inferior Endplate Failure

Medical imaging studies have noted the inferior endplate sustains injuries three to eight times more frequently than the superior endplate (Fujiwara et al., 2019; Ortiz & Bordia, 2011). While the exact source of this discrepancy remains unclear, anatomical differences between the two endplate structures likely play a significant role. For instance, some literature has reported the inferior endplate is approximately 11–14% thinner than the superior endplate with the most pronounced difference occurring at its center (Grant et al., 2001; Palepu et al., 2019; Zhao et al., 2009). This finding aligns with the increased likelihood of inferior endplate injury, as a reduction in the structure's thickness would increase its compliance, allowing it to reach yield stress more quickly and thus providing less resistance to the mechanical stress exerted by the nucleus during loading (Fields et al., 2011). Interestingly, the superior endplate is approximately 4% less porous than its inferior counterpart, a difference attributed to its greater thickness (Zehra et al., 2015). Generally, reduced permeability across the endplate limits fluid exchange, allowing the nucleus pulposus to maintain higher internal pressure and, in theory, exert greater stresses on the adjacent endplate (van Dieën et al., 2001). However, the increased thickness of the superior endplate appears to compensate for this potential rise in stress, conferring greater structural resilience overall.

Another structural variation is the relative curvature of the endplates with the superior level exhibiting greater concavity compared to the relatively flatter inferior endplate (Wang et al., 2012). Although the biomechanical implications of this curvature remain poorly understood, evidence suggests that concavity is linked to tensile strains experienced by the endplate (Fields et al., 2010). Drawing on structural engineering principles, a dome subjected to exterior compressive force

distributes stress along its meridian—the curved line connecting the apex to the base—to the periphery, enhancing strength (Aita et al., 2024). However, in the case of the superior endplate, compressive force from the nucleus applies stress internally, generating tensile strains that compromise its integrity. This tension should be particularly problematic given the superior bony endplate's organic composition, where the rigid mineral content and relatively low collagen proportion make it more susceptible to failure under tensile stress (Bevill et al., 2009; Hart et al., 2017; Niebur et al., 2000). Yet, this narrative does not seem to hold true as the inferior endplate appears to exhibit a greater predisposition to strain-related failure despite an inherently flatter structure that would in theory be able to better tolerate force application. Findings by Dudli et al. (2018) serve as a potential explanation for this oddity. Under high-rate impact loading, the superior endplate, with its larger concavity and volume, displayed a higher failure load. The authors hypothesized that the concavity allowed nuclear stress to be distributed over a larger area of the endplate thus reducing localized strain. This theory seems plausible as it is well documented that the superior endplate has a notably greater area to distribute nuclear stresses (Kishimoto et al., 2016). However, it should be considered that high-rate loading is more likely to induce vertebral body failure rather than endplate failure, which is more commonly observed under lower loading rates (Yingling et al., 1997). This raises the question of whether the observed differences in failure mechanisms were truly dictated by endplate curvature or influenced more significantly by variations in the quality of the underlying trabecular bone.

Regardless, the quality of the underlying trabecular bone is widely considered one of the most significant predictors of endplate injury. Trabecular bone provides structural support to the vertebral endplates, distributing stresses and strains to prevent injury. Its integrity depends on factors such as bone mineral content, apparent density, and volume fraction (Holmes et al., 1993;

Jackman et al., 2014; Zhao et al., 2009). A reduction in the trabecular density beneath the inferior endplate is likely another contributing factor in its greater incidence of injury (Zhao et al., 2009). Trabecular bone quality becomes particularly relevant given endplate injuries are often closely associated with degenerative bone conditions such as osteoporosis. This pathology creates an impairment in the trabecular structure through decreases in trabecular density and increased brittleness from a loss in toughness of the material (Osterhoff et al., 2016). However, the implications of endplate thickness may require a more nuanced approach than simply comparing absolute values. Due the age related changes to endplate thickness (Ferguson & Steffen, 2003; Roberts et al., 1997), a more insightful approach of future work might involve examining the relative decreases in thickness that each structure experiences with age. It is possible that the superior endplate becomes more vulnerable to injury once it reaches a proportional threshold of its original thickness, potentially making it susceptible to failure earlier than the inferior endplate. This highlights the importance of considering the synergy of multiple factors as structural variations beyond absolute thickness also play a critical role in endplate mechanics.

### 2.5 Comparative Impacts of Static and Cyclic Loading on Spinal Microdamage and Endplate Deflection

Two primary loading paradigms govern structural failure within materials: cyclic and static loads. Static loading involves the continuous application of a load at a given magnitude, whereas cyclic loading refers to the dynamic application and withdrawal of repetitive forces that fluctuate in magnitude. While both loading types contribute to intervertebral disc-related injuries (Hulme et al., 2008; Tsai et al., 1998; Zehr, Quadrilatero, et al., 2023), they also induce unique mechanical changes that affect endplate deflection.

A critical distinction between these loading types lies in the occurrence of microdamage within vertebral components. During cyclic loading, the repeated application of submaximal forces leads to fatigue failure in the endplate and the underlying trabecular bone (Lambers et al., 2013; Zehr, Quadrilatero, et al., 2023). In vertebral trabecular bone, fatigue failure manifests as microcrack accumulation in thinner regions of the osseous matrix where stress concentrations arise (Arlot et al., 2008). Overtime, this compromises the cancellous bone's capacity to provide adequate support to the endplate under compressive loads (Hulme et al., 2008; Jackman et al., 2014) Similarly, the endplate experiences microdamage in the form of voids and delamination of the hyaline cartilage layer from the subchondral bone causing for a reduction in both yield force and stiffness of the structure (Rodriguez et al., 2012; Zehr, Barrett, et al., 2022; Zehr, Quadrilatero, et al., 2023).

The occurrence of microdamage in spinal structures is not exclusive to cyclic loading as it also observed in static loading events (Jackman et al., 2014; Mirzaali et al., 2020; Nagaraja et al., 2005). While literature directly comparing the rate of microcrack accumulation of spinal structures during static versus cyclic contexts is scarce, one can surmise that static loading of submaximal magnitude and duration causes less microdamage than cyclic loading with equivalent parameters. This assertion operates under the logic that static loads reach an eventual equilibrium minimizing further microdamage, while cyclic loading continuously induces damage with each load repetition. Given that microdamage accumulation acts as a precursor to eventual injury (Lambers et al., 2013), gross structural failure is likely to occur sooner under cyclic loading conditions than static submaximal loads.

In other words, static loading paradigms enable spinal joints to be loaded for a duration that exceeds what would be possible with similar testing parameters in cyclic loading. This

distinction is important as loading duration directly influences intervertebral disc hydration (McMillan et al., 1996). Given the nucleus pulposus is primarily responsible for inducing endplate deflection (Holmes et al., 1993; Jackman et al., 2014), a loss of nuclear pressure impairs its capacity to induce deformation in the endplate. Furthermore, losses in nuclear fluid result in a reduction in spinal joint height. As joint height decreases, the endplates may contact one another in peripheral regions (Massey et al., 2012). This leads to the shunting of compressive forces away from the center of the endplate, more uniformly distributing stress across the surface and thereby further mitigating central deflection.

Given that the effects of cyclic loading on joint fluid loss is largely dependent on other dynamic loading parameters such as frequency, magnitude, and loading rate, predicting whether greater fluid loss occurs under static versus cyclic loading is difficult. In fact, some literature has demonstrated that in rat functional spinal units (FSUs), 1 Hz cyclic loading at a peak magnitude equal to that of a static load results in statistically insignificant differences in joint fluid loss (Masuoka et al., 2007). However, considering both that microdamage accumulation and endplate failure occur more quickly under cyclic loading and that fluid loss is time-dependent, it follows that static loading can induce more fluid loss simply because the joint can withstand static loading for durations unlikely to be survivable under cyclic loading. This touches on a key limitation of existing literature (further discussed in the following section) that seeks to quantify endplate deflection in FSUs through using static loading of magnitude ranging 1-3 kN over durations of 1 – 4 hours (Hulme et al., 2008; Jackman et al., 2014). Such measurements are inherently constrained, as the fluid loss observed in these tests likely exceeds what could occur under cyclic loading, thereby deviating from physiologically relevant conditions. This introduces a significant potential for inaccuracy in the reported endplate deflection measurements.

## 2.6 Previous Approaches to Measuring Endplate Deflection

The first notable attempt to estimate endplate deflection was by Brinckmann et al. (1983), who sought to determine the contribution of endplate deflection to the overall height change of spinal joints under load. In this study, human cadaveric FSUs were prepared by drilling 2 mm diameter bores from the exposed endplates to within 1 mm of the joint endplates. Metallic markers, 2 mm in diameter, were inserted into these bores along the central surface of the endplates. The specimens were mounted in a loading frame, with additional markers placed on the periphery of the apparatus. Incremental loading was applied in 1500 N steps, and roentgen stereophotogrammetry (RSA) was used to track the relative displacement of the markers. This methodology enabled calculation of the proportion of spinal joint height change attributable to endplate deflection. While proving endplate deflection to be an important factor in the spine's response to compression force, the accuracy of deflection measurements was largely limited. The insertion of metallic markers, which involved removing cancellous bone, likely led to an overestimation of deflection due to the crucial role of subchondral trabecular bone in supporting the endplate surface (Jackman et al., 2014; Watson et al., 2024). Furthermore, the assumption of symmetrical deflection between superior and inferior endplates was flawed, as these structures have been demonstrated to exhibit distinct mechanical behaviors and injury susceptibilities (Ortiz & Bordia, 2011; Zhao et al., 2009).

Sharing a similar methodology to Brinckmann et al. (1983), Holmes et al. (1993) implanted a displacement transducer beneath the center of the inferior endplate in lumbar discs, which remained attached to cranial and caudal halves of the adjacent vertebral bodies. Stepwise, undefined loads, described as "six roughly equal steps" to a maximum of 5.5 kN, were applied to the specimens. Following testing, bone ashing, a method to determine bone mineral content, was

performed on the trabecular structures beneath the transducer. Additionally, the nucleus water content was assessed by weighing it pre and post dehydration. Interestingly, this study concluded that rigidity of the underlying trabecular bone is a greater determinant of endplate deflection than the fluid content of the nucleus. However, the accuracy of its deflection measurements was limited. Similar to Brinckmann et al. (1983), drilling of a 1.6 mm diameter bore for transducer implantation likely caused an unnatural increase in deflection above the bore site. This limitation is especially relevant given the study itself concluded the importance of subchondral trabecular support for the deformation of the endplate. Furthermore, the exclusive implantation of the transducer in the inferior endplate precluded any comparison of superior and inferior endplate deflection.

Later work by Hulme et al. (2008) iterated upon previous attempts by avoiding the use of invasive methodologies and instead employed micro-CT imaging. Human osteoporotic cadaveric lower thoracic and lumbar FSUs were prepared with spherical glass fiducial markers adhered to the exterior cortical shell to account for cortical shell deformation during compression. FSUs were subjected to static loading in a stepwise manner at increments of 200 N, 1000 N, and 1800 N. For the 1000 N and 1800 N loads, a 45-minute static preload was applied to minimize stress relaxation, followed by a 1-hour whole-joint scan and an 8-minute scan of each endplate (Figure 2.5.1). The authors observed a greater deflection of the inferior endplate compared to the superior endplate across loading conditions. However, while the use of micro-CT was novel and enabled level specific endplate deflection measurements for both endplates within the joint, several limitations were noted. Firstly, the authors acknowledged that the poor temporal resolution of micro-CT required the joint to be loaded statically. As discussed in Section 2.4, prolonged static loading induces excessive fluid loss within the joint, likely exceeding what would occur under typical *in viv*o conditions. This reduction in nuclear fluid pressure likely led to underestimation of endplate

deflection at these loads. Additionally, the micro-CT system employed a relatively low nominal isotropic resolution of 82 microns to achieve faster scan times, which is problematic given that deflection measurements were reported to three decimal places. Although sub-voxel interpolation enhanced precision and reproducibility of deflection measurements, its accuracy was inherently limited as interpolation remains an approximation.

Jackman et al. (2014) adopted a similar approach, using stepwise loading to achieve 1 mm increments of compressive displacement, followed by 3–4 hours of whole-joint micro-CT imaging until failure (Figure 2.5.2). This extended scanning duration enabled higher-resolution imaging at 37 μm/voxel and enabled the evaluation of trabecular structural properties such as trabecular separation, apparent density, and volume fraction. By imaging endplate deflection and trabecular bone structures before and after vertebral fracture, the study also noted the inferior endplate's greater deflection and highlighted endplate deflection as a clinically relevant factor in identifying vertebral deformities and fractures. However, the study's deflection measurements faced significant limitations similar to those of Hulme et al. (2008), particularly due to the use of prolonged static loading. The extended scanning times exacerbated fluid loss in the joint under static loading, likely exceeding what would occur in physiological conditions. Additionally, the methodology overlooked the effects of microdamage accumulation and fatigue failure associated with cyclic loading, a loading pattern more representative of everyday spinal exposure.

Overall, current literature has established key principles such as endplate deflection and the structural integrity of the underlying trabecular bone as major contributors to vertebral failure. The inferior endplate has been shown to exhibit greater deflections under prolonged static loading, which is thought to contribute to its higher incidence of failure. However, many unknowns remain regarding the mechanisms underlying these observed differences. Specifically, the degree to which

superior and inferior endplates differ under cyclic loading, a condition notably distinct from static loading, remains unclear. The thresholds of cyclic exposure at which deflection rates begin to diverge and the trajectories of the deflection–cyclic exposure relationship have not yet been explored. Furthermore, while greater inferior endplate deflection is consistently observed in human cadaveric tissue, it is not yet known whether the porcine model demonstrates similar behavior. Finally, it remains uncertain whether the proportion of the nucleus pulposus occupying the endplate area represents a risk factor for endplate failure. Addressing these gaps will bring a stronger understanding to the time varying changes of superior and inferior endplate deflections and contribute to existing knowledge of vertebral failure mechanisms.

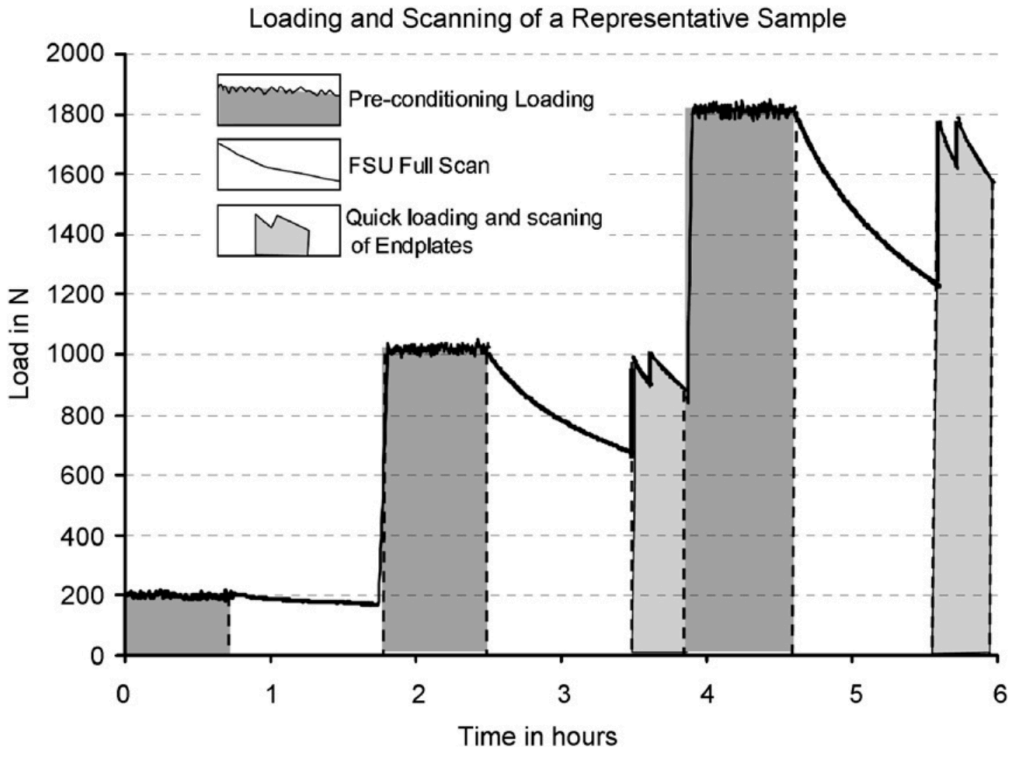



***Figure 2.5.1**: Loading protocol for FSUs used by Hulme et al., 2008*
*"Loads were chosen to reflect rest (200 N), standing (1000 N) and light manual work (1500–2000 N depending on vertebra size). Two scans were performed; a full FSU scan (approx. 60 min, "static") and a quick scan of the endplates alone (approx. 8 min, "quick"). Prior to the full FSU scan the specimen was pre-conditioned for 45 min to reduce stress relaxation during scanning." (Hulme et al., 2008)*

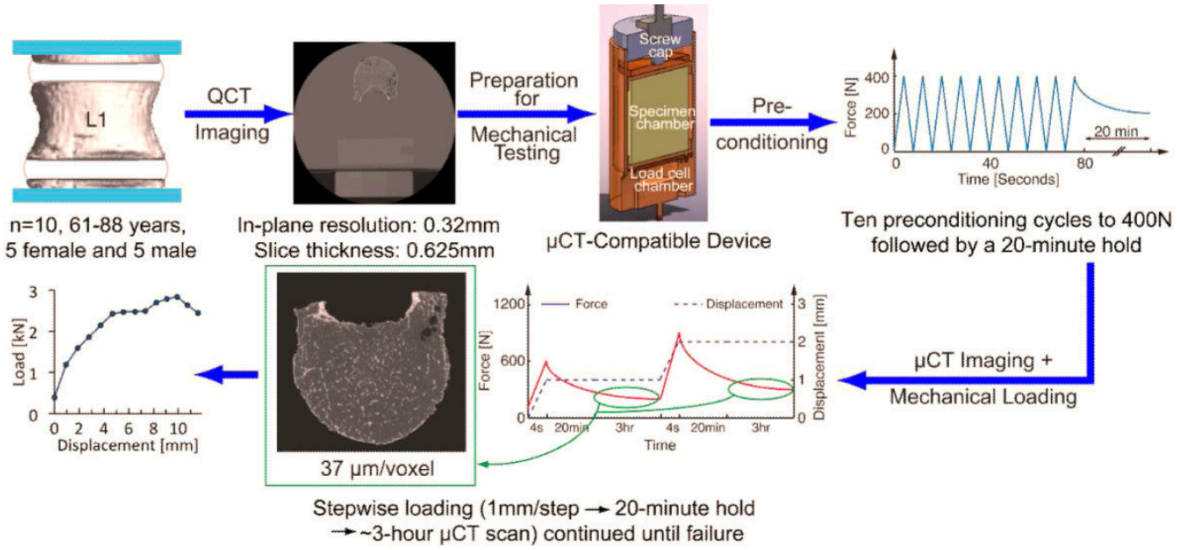



***Figure 2.5.2:*** *"Experimental procedure for mechanical testing and imaging." (Jackman et al., 2014)*

# Chapter 3 - Methods

## 3.1 Overview of Study Design

A mixed-measures study design was used to evaluate the effects of cyclic loading on the deflection of porcine cervical vertebral endplates. Loading was applied exclusively to the central, nucleus-bearing region of the endplate using a custom-fabricated specimen specific indenter shaped to match the region's unique topography. Endplate deflection was quantified by tracking the displacement of the indenter during brief, incrementally increasing static loads. Three separate linear mixed effects models were fit, each comparing the two endplates from each joint. Specifically, caudal C3 vs cranial C4, caudal C4 vs cranial C5, and caudal C5 vs cranial C6. For each model, loading magnitude (0.3 kN, 1 kN, and 3 kN whole joint equivalents), loading cycles (0, 1000, 3000), and endplate level were included as fixed effects to evaluate their influence on endplate deflection. The proportion of the nucleus-occupying region relative to the total endplate area was included as a continuous covariate. Lastly, an additional linear mixed effects model was fit to compare the effects of joint level (C3C4, C4C5, C5C6) on the difference in superior and inferior endplate deflection. Loading magnitude (0.3 kN, 1 kN, and 3 kN whole joint equivalents) and loading cycle (0, 1000, 3000) were again included as fixed effects.

## 3.2 Specimens

This study used porcine cervical vertebrae as a surrogate for the human lumbar spine due to its morphological similarities (Yingling et al., 1999). Specimens were procured from adolescent domestic hogs (5 – 10 months of age or ~110 kg) via an abattoir. All specimens were stored at -20°C and thawed at room temperature for a minimum of 12 hours. Although intact intervertebral discs are not directly involved in this work, existing literature has demonstrated a close relationship

between disc degeneration and endplate health (Chang et al., 2009; Nachemson et al., 1970). To ensure representative conditions, intervertebral discs were required to satisfy the Grade 1 criteria of the Galante scale (Galante, 1967); no breaches in the annulus fibrosis fibers and the presence of a white and gelatinous nucleus.

For the purpose of clarity, the terms superior and inferior within this document refer to the position of the endplates within a spinal joint, while cranial and caudal describe the positioning of endplates relative to an individual vertebra (Figure 3.2.1). The endplates of interest in this study included the caudal endplates of C3, C4, and C5, as well as the cranial endplates of C4, C5, and C6. These specimens were selected because they define the boundaries of the three intervertebral joints relevant to the porcine cervical spine model. Since this investigation focused on comparing superior and inferior endplate deflection within a joint, accessory structures such as the cranial endplate of C3 and the caudal endplate of C6 were excluded. These structures do not form complete functional spinal units (FSUs) within the model, making them less relevant to this study's objectives. For vertebrae with both cranial and caudal endplate deflections of interest (C4 and C5), only one endplate was mechanically tested per specimen to avoid confounding deflection measurements. Since the porcine cervical spine model consists of four vertebrae forming three spinal joints (C3C4, C4C5, and C5C6), each spine thus yields either a C3C4 and C5C6 joint (4 endplate specimens) or a C4C5 joint (2 endplate specimens) whereby C3 and C6 vertebrae are excluded (Figure 3.2.2 and 3.2.3). Due to this, the 36 endplate specimens used in this study required 36 unique vertebrae. Originally, six porcine cervical spines were intended to provide 24 specimens (C3C4 and C5C6 joints comprising endplates), and another six spines were to provide 12 specimens (C4C5 joints). However, due to errors and setbacks during data collection, only three pairs of C3C4 and C5C6 joints originated from unique spines (Figure 3.2.4). This imbalance in

specimen sourcing was either statistically accounted for or deemed inconsequential to the analyses of data (Section 3.9). No vertebra was mechanically tested more than once.

A sample size of 24 vertebrae, distributed evenly across six groups with four endplates per group, was recommended based on an *a priori* power analysis using data on superior and inferior endplate deflection measurements reported by Hulme et al. (2018) – the only available study with sufficient data to estimate an effect size. The analysis assumed an alpha level (α) of 0.05, power (1 - β) of 0.95, and an effect size of 0.29 (Cohens f). However, given that this power analysis was a rough estimate, 12 additional vertebrae were added to the sample size. This created a sample size of 36 vertebrae, distributed evenly across 6 groups with 6 endplates per group (Figure 3.2.4)

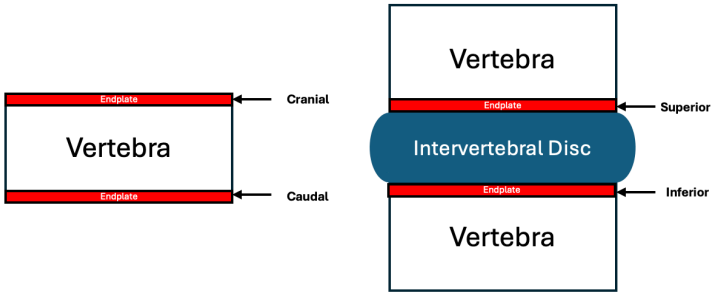



***Figure 3.2.1**: Illustration of endplate level terminology*

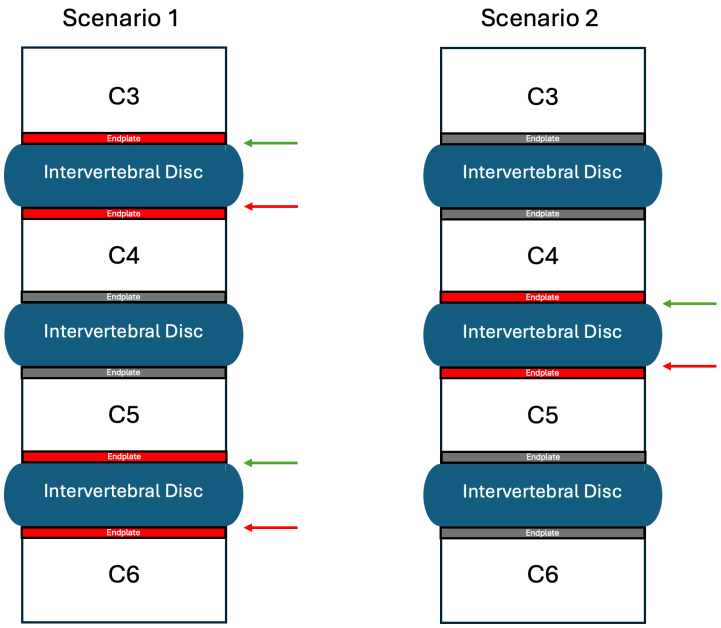



***Figure 3.2.2**: Schematic of tested endplate.*
*Green and red arrows highlighting the superior and inferior endplates of interest, respectively. Scenario 1 illustrates the endplates to be mechanically tested comprising the C3C4 and C5C6 joints within a spine. Scenario 2 illustrates endplates to be tested that comprise the C4C5 joint within a completely different spine from that of scenario 1. No vertebrae were reused at any point.*

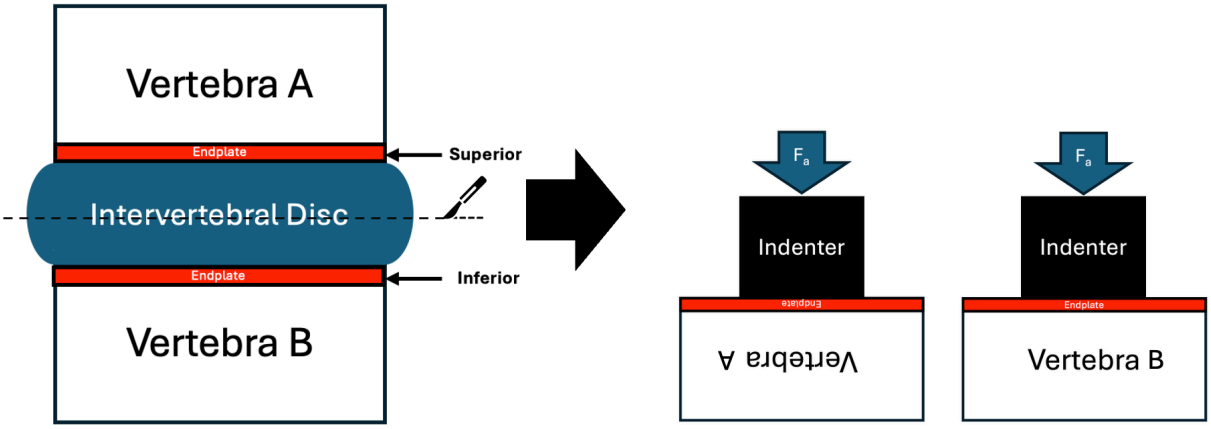



***Figure 3.2.3:** Diagram of how each endplate within a joint was mechanically loaded*

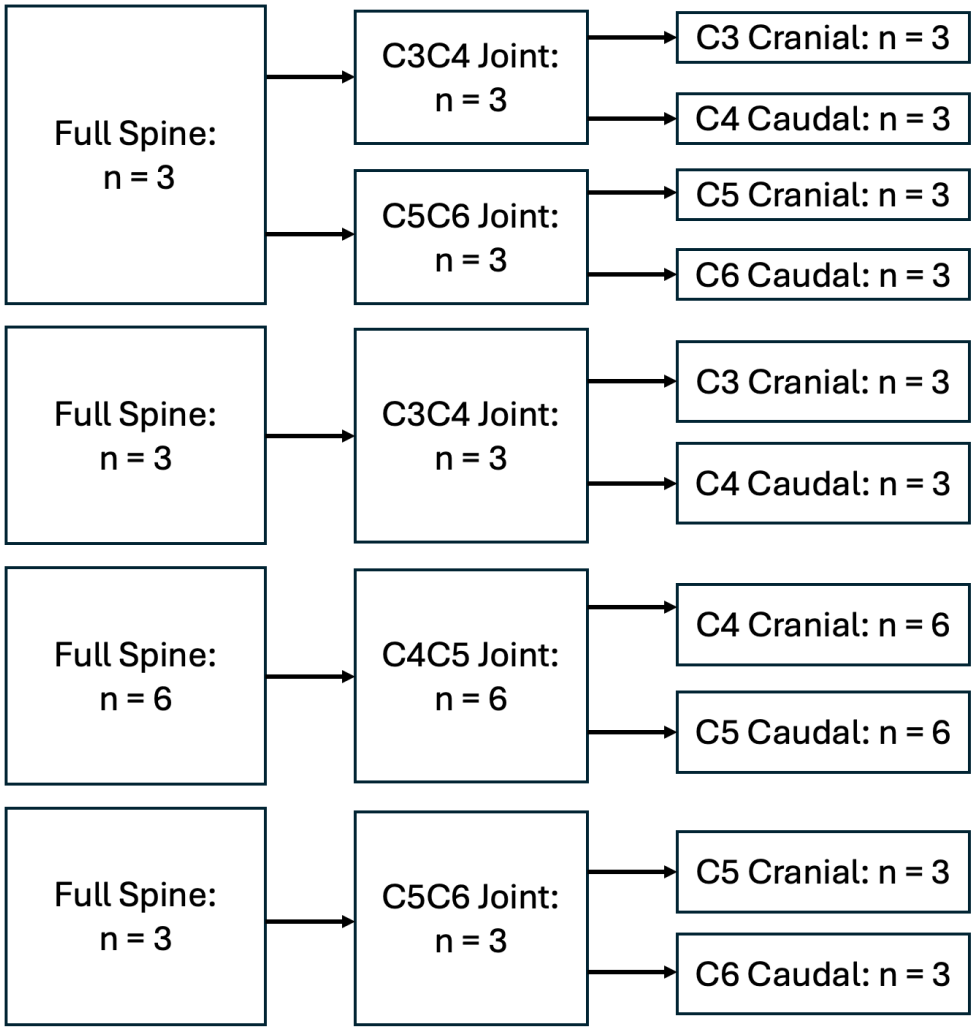



***Figure 3.2.4**: Schematic of specimen allocation*

### 3.3 Specimen Preparation

Vertebrae (C3, C4, C5, and C6) were excised. Endplates of interest were carefully cleaned of nuclear material, ensuring the peripheral annular tissue and endplate surfaces remained intact and undamaged. Given the fluid content of the tissue, the endplate surface was inherently reflective, which posed a challenge for laser profilometry (further detailed in section 3.4). This reflectivity created artifact in the 3D scan resulting in misrepresentations of the endplate surface, where areas of glare produce artificial bumps in the scan. To address this issue, a fine layer of

cornstarch powder was brushed onto the endplate surface (Figure 3.3.1). Cornstarch $(C_6H_{10}O_5)_n$ was chosen over alternatives like spray paint, industry-specific 3D scanning sprays, and titanium powder due to its availability and chemical inertness. Additionally, cornstarch minimally alters the specimen's color, a crucial factor for subsequent visual imaging steps (Section 3.5). A point can be made about the potential dehydrating effects of this substance on the endplate structure. However, as less than a gram was applied to each specimen, these effects were likely minimal. Additionally, cornstarch could be easily removed from the specimen using saline, which also replenished any fluid loss. The use of saline for this purpose is noted in Section 3.8. Therefore, while the exact influence of cornstarch application on the endplate's mechanical properties has not been experimentally tested, there is strong reason to believe that its effects were negligible.

The non-scanned endplate of each vertebra was cleaned of cartilage and soft tissue (Figure 3.3.2). Specimens were then potted in aluminum cups and secured with 19-gauge steel wire and non-exothermic dental plaster (Dentstone, Southbend, IN). The cleaned endplate was placed in direct contact with the dental plaster prior to curing allowing the compound to conform to the irregular endplate surface. This preparation minimized whole specimen vertical displacement during loading caused by fluid extrusion from cartilage and soft tissue, which could otherwise reduce the accuracy of deflection measurements (Section 3.7). A pair of painted ball bearings, each 2.33 mm in diameter, were placed on the outer annular region of the endplate surface (Figure 3.3.3). A top-down reference image was captured using a tripod-mounted camera (70D, Canon Canada, Inc., Brampton, Ontario, Canada) fitted with a macro lens to achieve a "flat" and minimally distorted image. This image served as a visual reference for selecting the nuclear region in the colorless 3D scan, as described in Section 3.5. Lastly, specimens were wrapped with saline

soaked gauze that was rehydrated every 20 minutes prior to and during mechanical loading (Figure 3.3.4).

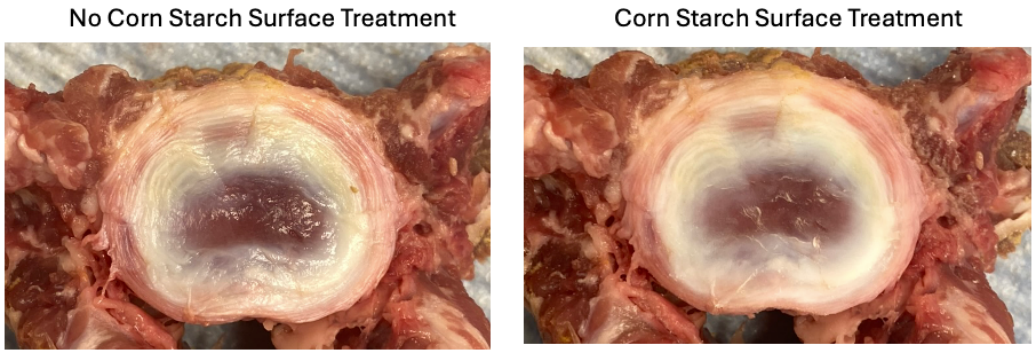



***Figure 3.3.1****: Comparative images of specimen glare: without cornstarch (left) and with cornstarch (right).*



***Figure 3.3.2****: Non-testing endplate cleaned of cartilage and soft tissue in preparation to interface with potting*

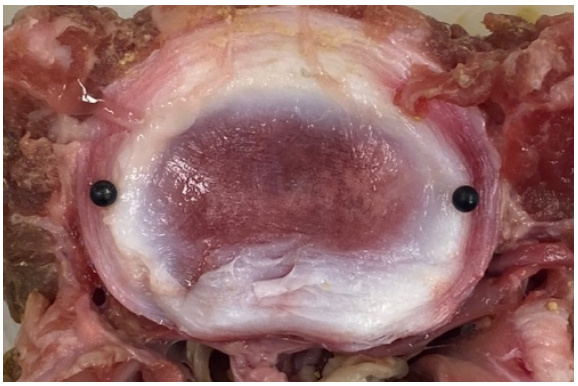


***Figure 3.3.3****: Representative image of the positioning of image markers on the specimen surface.*

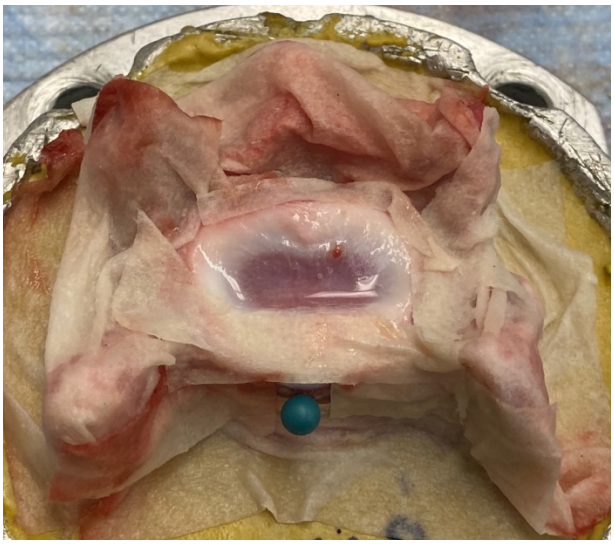


***Figure 3.3.4****: Specimen wrapped in saline-soaked gauze*

### 3.4 Surface Profilometry

To capture a point map scan of the endplate surface, potted specimens were placed on a ball screw linear rail in series with a closed loop servo motor positioned beneath a high-speed surface laser profilometer (LJ-V7080, Keyence Corporation, Osaka, Japan) (Figure 3.4.1). A micro controller (Arduino Mega 2560 Rev3, Turin, Italy) programmed with custom software (C++, Arduino IDE 2.3.2, Arduino, Turin, Italy) controlled the stepper to horizontally displace the vertebra in 1-micron increments. The laser was then triggered by the micro controller to capture a profile of the endplate surface every 47 microns of the specimen's displacement. This scanning frequency was selected based on the laser's beam width being 47 microns. The scanning apparatus featured a vertical resolution of 0.5 micron and horizontal resolution of 10 micron, both of which exceeds what is necessary to capture the macroscopic curvatures of the endplate.

A smoothing function built into the scanning laser was applied, using a 16-value moving average across each of the 800 points in a single sample along the laser's scanning path (Figure

3.4.2). This smoothing setting was experimentally determined to effectively reduce glare-induced artifact in the 3D scan while also minimizing losses in endplate topographical detail.

To ensure the profilometer was level relative to the specimen, a three-point leveling system mounted to the laser emitter was used (Figure 3.4.3). The built-in lateral angle detection of the laser, combined with an inclinometer fixed to the anterior of the system, allowed for the measurement and correction of any coronal and sagittal tilt of the emitter. Lastly, to mitigate vibrationally induced movement that would introduce noise into the 3D scan, the entire system was bolted to an aluminum plate acting as a base.

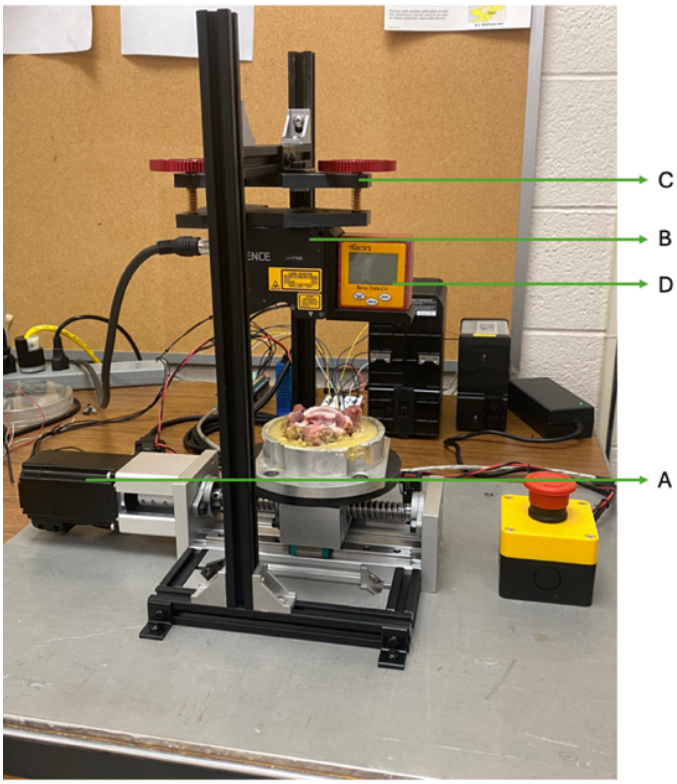



***Figure 3.4.1****: Custom constructed laser profilometry setup.*
*A – Closed loop servo motor in series with a ball screw linear rail, B – Laser profilometer, C – Three-point leveling system, D – Inclinometer*

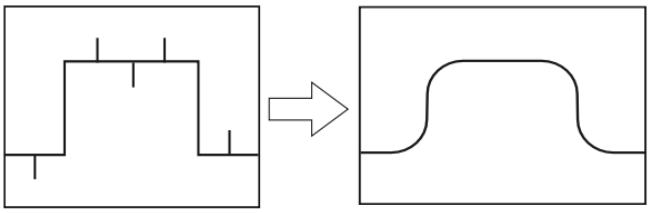


***Figure 3.4.2****: Schematic illustrating the operation of the built-in profilometry moving average smoothing algorithm. Image adapted from (Keyence, 2012)*

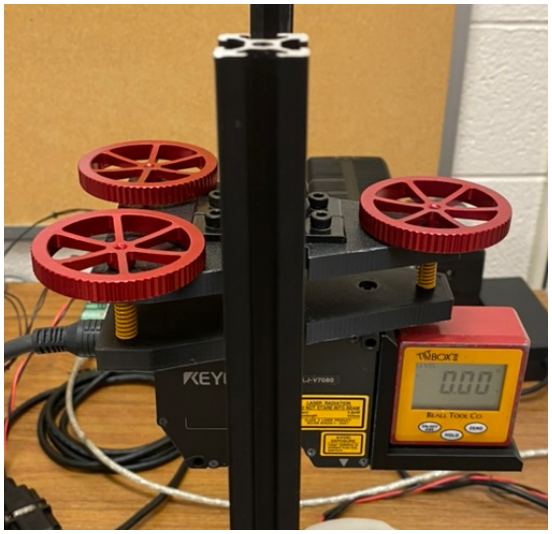


***Figure 3.4.3****: The three-point leveling mechanism ensures the scan remains square relative to the specimen's surface.*

### 3.5 Indenter Modelling

To utilize the point map scan of the endplate surface, a custom python script (Version 3.11, Python Software Foundation, Scotts Valley, CA) was employed to convert the data matrix into a 3D mesh. The resulting 3D model of the specimen was then imported into a 3D modelling program (Blender 4.21 LTS, Blender Foundation, Amsterdam, Netherlands). The top-down image of the specimen previously photographed (Section 3.5.1) was superimposed onto the model whereby the image markers (ball bearings) aligned with the position that they appeared on the scan. This step was necessary for visually determining the nuclear region of the endplate as the color of the specimen is not captured during the 3D scanning process. Visual identification of the nucleus

occupying area was performed manually via the experimentalist. This approach was preferred over automated methods due to the complexity and development costs associated with creating software capable of interpreting the highly variable specimen colours and 3D profile data from topography scans. A negative mold of the nucleus occupying endplate region was mounted to a standardized indenter base to construct the custom indenter model (Figure 3.5.2).

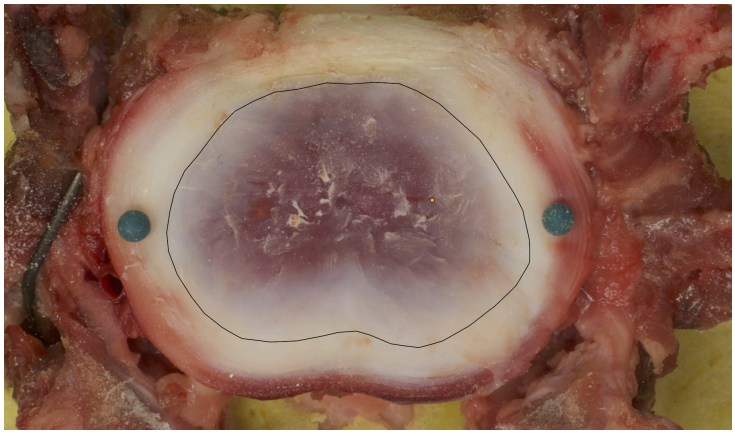


***Figure 3.5.1****: Example of a manually defined nuclear region of the endplate*

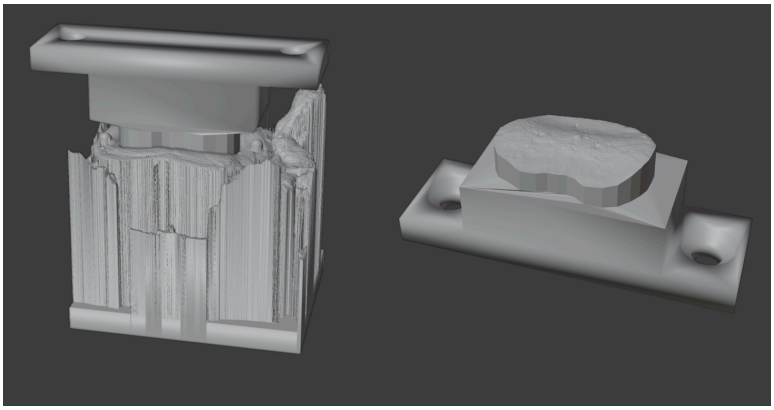


***Figure 3.5.2****: Sample of an indenter model generated from a 3D scanned endplate surface.*

### 3.6 Indenter Fabrication

The indenter was then fabricated using fused deposition modelling (FDM) 3D printing (Kobra 2 Pro, AnyCubic, Shenzhen, China). Indenters were printed with 100% infill black polylactic acid (PLA) with a layer height of 0.05 mm (Figure 3.6.1). This print resolution was experimentally optimized to balance scan fidelity and manageable fabrication time. PLA was selected for its affordability and its high stiffness amongst other 3D-printable materials (Ahmed et al., 2016). It has a compressive strength ranging from 48 to 62 MPa (Gao et al., 2022), far exceeding injurious endplate stresses (Brown et al., 2008). PLA's suitability was further confirmed through pilot testing where a non-representative endplate indenter was constructed and mechanically tested against the nucleus occupying region of the specimen (Figure 3.6.2). The endplate failed at approximately 3 kN of load, well above the loads applied in this protocol (section 3.8), while the indenter's shape remained unchanged. The structural integrity of the indenter was verified by comparing 3D profiles before and after load exposure, showing no observable differences. To confirm proper contact between the indenter and the endplate surface, the center of the indenter was marked with ink, and the minimum load used in this protocol (see Section 3.8) was applied to assess pigment transfer. Contact was verified at the center of the endplate, as this region has the thinnest cartilage (Berg-Johansen et al., 2018; Roberts et al., 1996) and thus the least ability to conform to the indenter surface, making it the most critical area for ensuring accurate surface alignment (Figure 3.6.3). An imprint of the indenter could also be seen across the entire endplate surface post loading exposure.

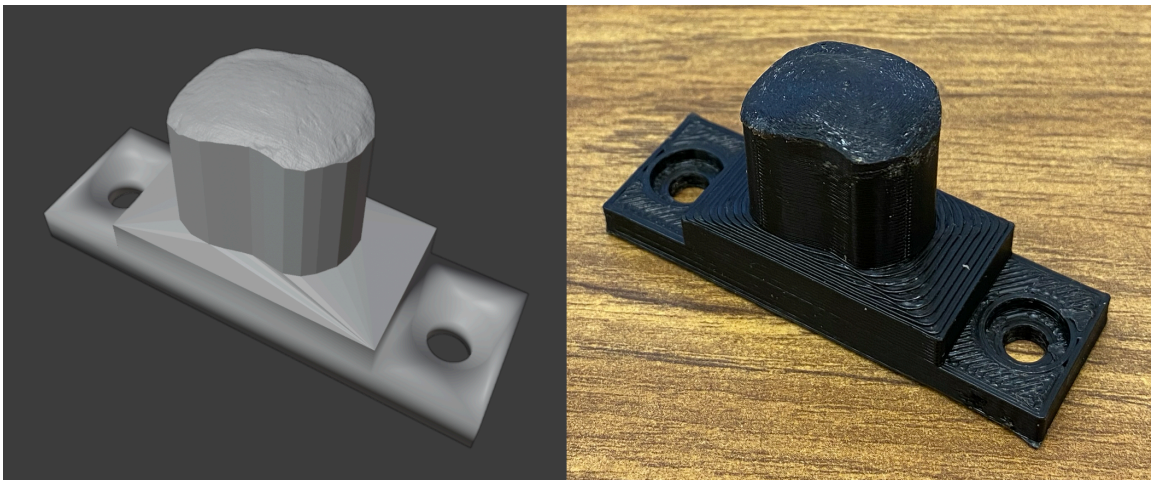


***Figure 3.6.1****: Comparison in fidelity between the modelled and fabricated indenter*

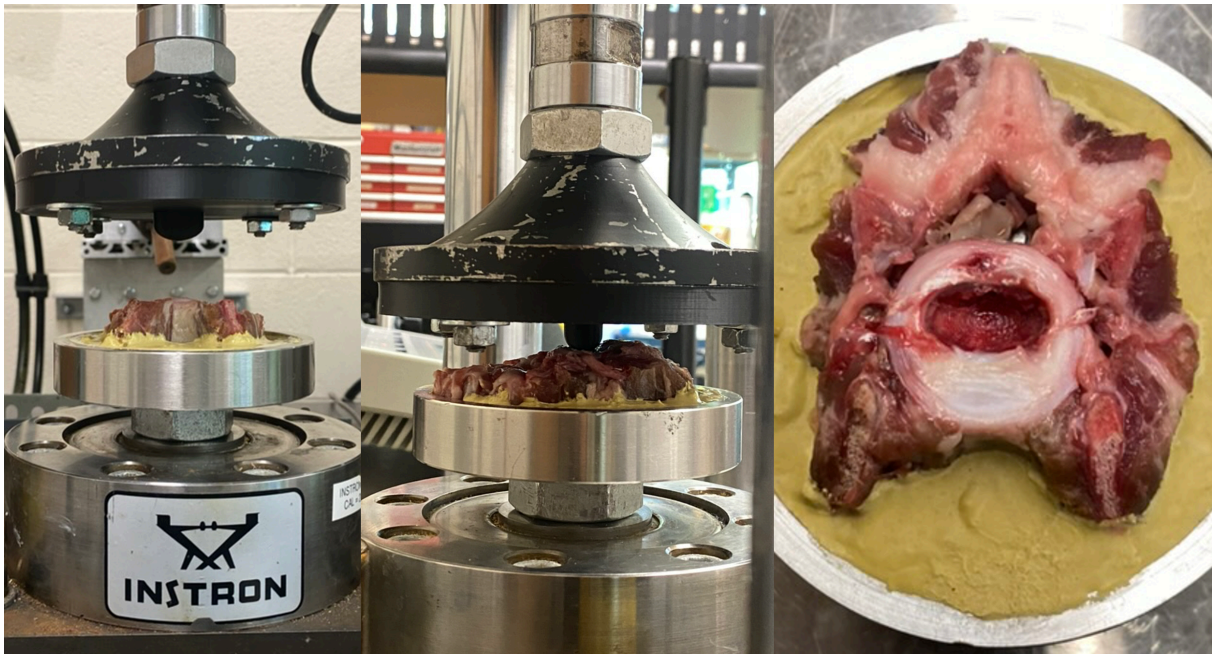



***Figure 3.6.2****: Endplate of specimen loaded within the central region to failure (Right) using a non-representative indenter (Middle and Left)*

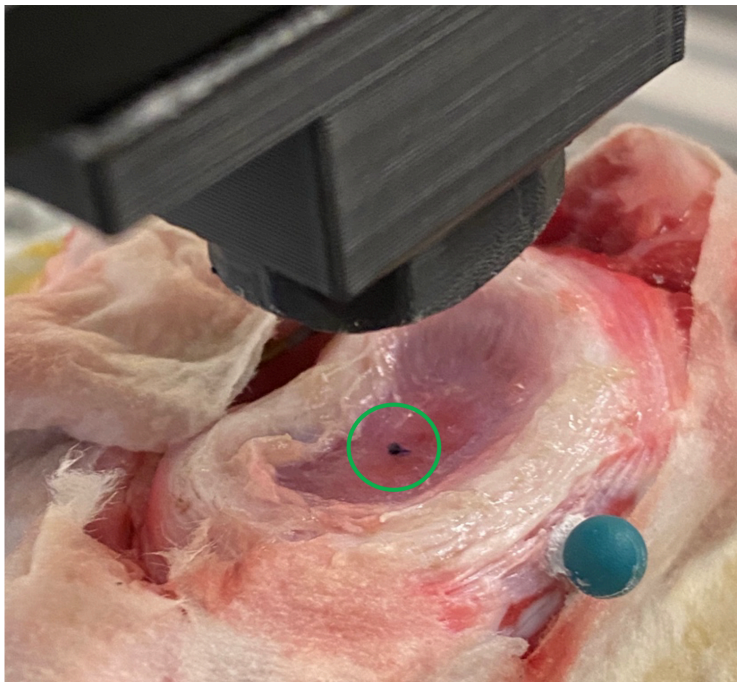


***Figure 3.6.3****: Verification of central endplate–indenter contact via ink transfer*

### 3.7 Measurement Correction

In previous work, the terms displacement, deformation, and deflection have all been used interchangeably to describe both the extent of bending and vertical change in position of the endplate (Brinckmann et al., 1983; Holmes et al., 1993; Hulme et al., 2008; Jackman et al., 2014). Owing to the lack of consistency in this nomenclature, the present study defines these terms as follows. Endplate displacement describes the translational movement of the entire endplate structure with the central and peripheral regions moving in tandem. Unless specified otherwise, it does not describe localized motion or bending within the structure. Deformation is a change in shape occurring anywhere within a structure. Lastly, deflection describes specifically the deformation in the central region of the endplate relative its outer bounds. As a result, all deflection is deformation, but not all deformation is deflection. Given this logic, the primary measurement of

this study will be defined as endplate deflection since this term describes specifically deformation in the central region of the endplate where loading was applied.

In this study, endplate deflection is derived from the difference between the indenter's displacement and the displacement of the endplate's periphery resulting from net compression of the whole system (Equation 1). This net displacement of the tested endplate can be traced to two primary sources. First, the non-tested side of the vertebra, which is in direct contact with the rigid metal potting and plaster, undergoes fluid loss during loading, particularly within cartilaginous and soft tissues. This loss results in a reduction in overall vertebral height that contributes to the indenter's measured displacement. This effect was mitigated via the removal of the cartilaginous material interfacing the potting, as described in Section 3.3. Nonetheless, settling of the entire structure remained an inevitable and notable source of measurement error. Secondly, while the majority of the load borne by the spinal vertebra is supported by the trabecular bone, a significant portion is also carried by the cortical shell (Eswaran et al., 2006). Despite cortical deformation likely being minimal, ranging from 9 to 40 micron in a 2 kN full joint loading context (Hulme et al., 2008), this factor remains a potential source of error.

Therefore, to maximize the accuracy of deflection measurements, it was necessary to account for compression across the entire vertebra. To do so, a 6 mm diameter ball bearing was affixed to the anterior of the specimen at the level of the epiphyseal plate using cyanoacrylate (Figure 3.7.1). This mounting location was chosen because it served as the boundary between the endplate and the underlying bone. The marker was mounted above the anterior cortical shell of the vertebral body given this region is free of peripheral structures such as transverse processes and pedicles, which are present in the lateral and posterior regions. These protruding structures are associated with increased localized cortical density at their attachment sites (Zhao et al., 2009),

likely resulting in greater regional stiffness of the vertebra. The absence of such structures in the anterior region of the cortical shell makes this a "worst-case scenario" for observing cortical deformation during loading thus justifying the placement of the marker in this location. The use of adhesive was chosen over more invasive methods, such as bone pins or screws, to minimize methodologically induced damage to the vertebra while maintaining the rigidity necessary to securely attach the marker. Vertical displacement of the marker during loading was quantified using a laser profilometer (LJ-V7080, Keyence Corporation, Osaka, Japan). To prevent reflection induced noise in the profilometer's readings, the marker was spray painted with a matt, minimally reflective paint (Tidal Pond Chalked Ultra Matte Paint, Rust-Oleum). The profilometer was mounted to a ball screw linear rail driven by a closed-loop stepper motor, allowing consistent positioning above the marker (Figure 3.7.2). During brief static loading periods (further discussed in section 3.8), the laser profilometer's measurement beam was repeatedly displaced in 50-micron increments above the spherical marker's surface. A 50 μm increment was selected as it was a similar value to the laser's width of 47 μm and represented a clean fraction of large measurement units, simplifying calculations, coding, and integration within the scanning system. Despite the profilometer's 1 μm resolution in the z-axis (vertical) and a repeatability of 0.5-micron, small vibrations introduced by the surrounding environment, particularly from the material testing system's hydraulic compressor, will impact measurement accuracy. To mitigate this limitation in the repeatability of gross vertical endplate displacement measurements, peak heights from 4 topographical scans of the marker were averaged. Since each scan takes around 8 seconds to complete, 4 repetitions of the scanning process provided a reasonable distribution of peak vertical positions while also only taking approximately 32 seconds to complete, a duration unlikely to significantly influence the overall mechanical response of the specimen.

$$\text{Endplate Deflection} = \text{Indenter Displacement} - \text{Peripheral Endplate Displacement}$$

***Equation 1**: Formulaic representation of endplate deflection in this experimental protocol*

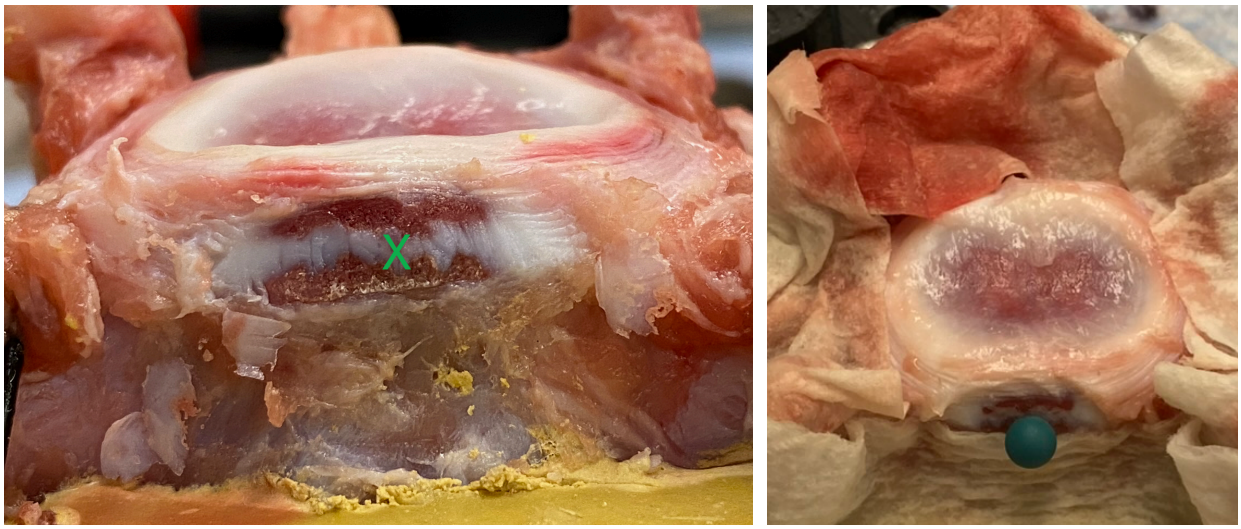


***Figure 3.7.1**: 6 mm diameter spherical marker affixed to the anterior surface of the specimen's epiphyseal plate*

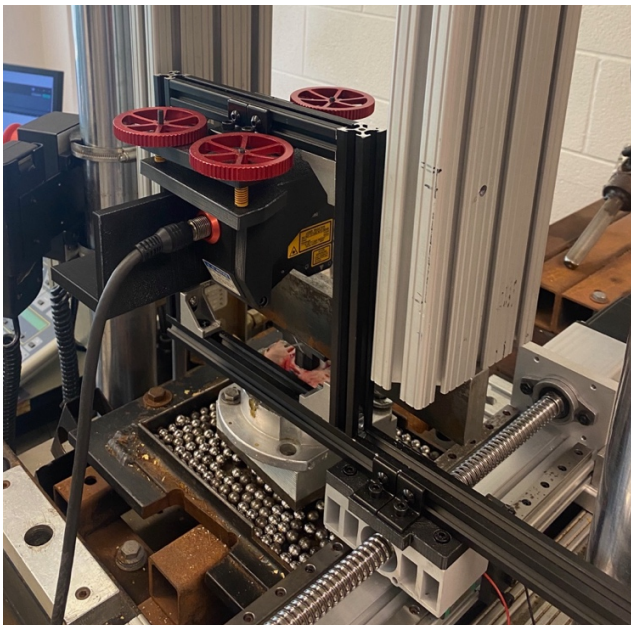


***Figure 3.7.2**: Custom constructed laser profilometry setup interfacing with the material testing system apparatus*

### 3.8 Cyclic Loading Protocol

The indenter was affixed to a hydraulic material testing system (Model 8872, Instron, Toronto, ON) with a frame stiffness of 260 kN/mm via a custom metallic fixture (Figure 3.8.1). The potted specimens then had spherical markers placed on the annulus during laser topography (Section 3.3) removed and cornstarch gently cleaned off the surface using saline. The vertebrae were then positioned such that the tested endplate was in a perpendicular position beneath the indenter. Owing to the precise fit between the indenter and endplate surface, and with the specimen's pot positioned on a bed of oiled bearings, alignment between the indenter and endplate surface was ensured as the specimen would "snap" into placed upon contact. A static 0.3 kN force was then applied for 15 minutes to equilibrate fluid within the cartilage of the endplate (Callaghan & McGill, 1995). Cyclic loading was then performed using a normalized haversine waveform (Figure 3.8.2) at magnitudes ranging from 0.3 kN to 30% of the predicted ultimate compressive tolerance (UCT) (Zehr et al., 2019; Zehr, Watson, et al., 2023). The loading cycles were applied at 1 Hz, a frequency previously used in studies of identical cyclic loading parameters (Zehr et al., 2020). The applied compression waveform represents a simulated force-time profile of lumbar spinal joints during a lifting task (Granata & Marras, 1995). The baseline load of 0.3 kN represents the approximate compressional force experienced by the lumbar spine during upright positioning of the trunk (Zehr et al., 2019), while the peak force (30% predicted UCT (Parkinson et al., 2005)) reflects typical low-back joint loading during moderately demanding repetitive lifting tasks (Gooyers et al., 2018). However, given these values are representative of whole spinal joints and this study applied load exclusively to the central region of the vertebral endplate, conversion from whole joint force to nuclear pressure was necessary. Finite element modeling from previous literature provides the relationship between whole joint compression force and nuclear pressure,

enabling the calculation of equivalent nuclear stress levels (Peng et al., 2011) (Figure 3.8.3). To determine the appropriate load for inducing such stresses, the stress parameters were normalized relative to the indenter-endplate contact area, as determined from the 3D model of the indenter (Equation 2). Sample calculations pertaining to this load-stress-load conversion is provided in Table 3.1.

The cycle-dependent changes in endplate deflection were measured at cumulative load exposures of 0, 1000, 3000, and 5000 cycles. The 1000-cycle mark approximates the load experienced during 1 hour of repeated exertion (Hansson et al., 1987) while 5000 cycles represent 94% of the joint's typical lifespan under these load magnitudes and frequency parameters (Zehr et al., 2020). Lastly, the 3000-cycle point serves as an intermediate between these exposure levels. At each time point, deflection measurements were captured based on the indenter's displacement while specimens are exposed to brief static stresses. Displacement readings had a resolution of 1 micron. Previous literature has classified spinal compressive forces during standing, walking, and moderate intensity lifting (Beach et al., 2019; Callaghan & McGill, 2001; Gooyers et al., 2018) approximately equating 0.3 kN, 1 kN, and 3 kN, respectively. As discussed previously, these whole joint equivalent forces necessitated conversion to an applied load within the indenter. A load-to-stress conversion table displaying a sample of these calculations is provided below (Table 3.2). The transition between static load thresholds were automated using a quasi-static ramp protocol with a loading rate of 0.025 kN/s (Yingling et al., 1997). As a result, this protocol took approximately 10 seconds to increase the force from 0.3 kN to the 1 kN equivalent threshold and about 30 seconds to transition between 1 kN and 3 kN equivalent thresholds (Figure 3.8.4). Upon reaching the target load during the ramping process, the system was held at that load for 10 seconds to allow both its 2$^{nd}$ order response and endplate surface to equilibrate. The material testing system

switched to position control to minimize the effect of viscoelastic creep, which would have otherwise occurred under load control during sustained static loading periods. During these static loading periods, the specimen bound marker was scanned following the protocol discussed in section 3.7. The indenter displacement was recorded at the end of the 40 second period for each force magnitude based on the material testing system's actuator position. The entirety of the cyclic, ramp protocol, and marker scanning processes were automated using both custom waveform protocols within the material testing system (WaveMatrix2, Instron, Toronto, ON) in parallel with custom python code to initiate scanning protocols. This automation ensured a high repeatability and consistency in load exposures and measurement periods across specimen.

The order of static load magnitudes (0.3 kN, 1 kN, and 3 kN whole joint equivalents) was not randomized as applying a higher load prior to lower increments would have confounded subsequent, lower magnitude endplate deflection measurements. A schematic of the entire loading protocol is illustrated in Figure 3.8.5.

Fixed stress targets during static loading, rather than values relative to the predicted UCT of each specimen, were selected as this approach aligns more closely with ergonomic recommendations which are based on absolute spinal compressive forces and not individual anatomical variations. This method allows the results of this study to be more directly applicable with current injury prevention tools and provide direct insights relevant to ergonomic guidelines and workplace risk assessment (NIOSH, 1991).

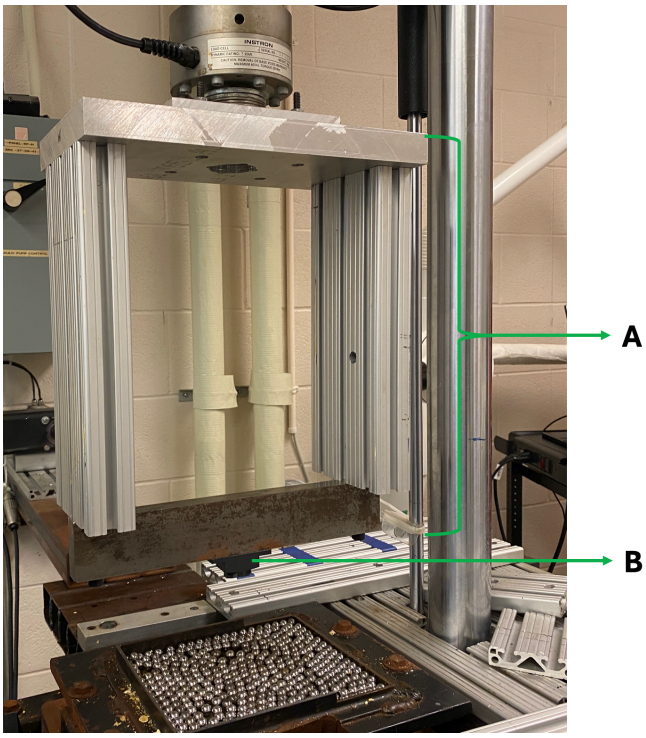



***Figure 3.8.1**: A. Metallic Fixture, B. Indenter*

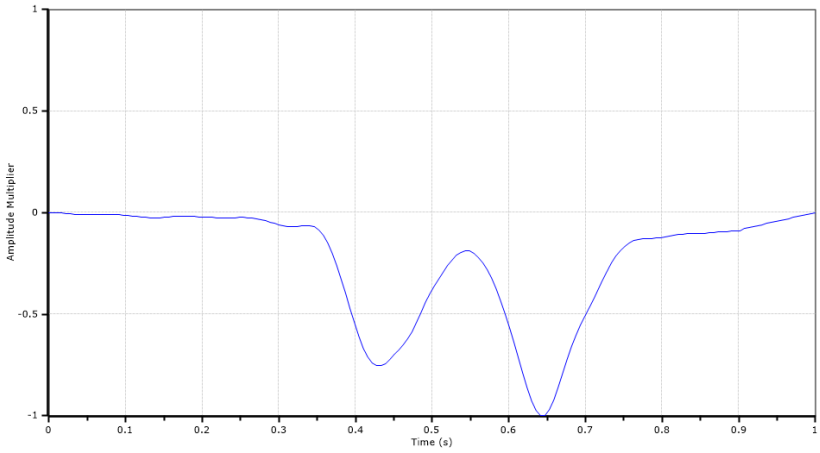



***Figure 3.8.2**: Normalized Haversine waveform representative of the force time pattern during a moderate demand repeated lifting task*

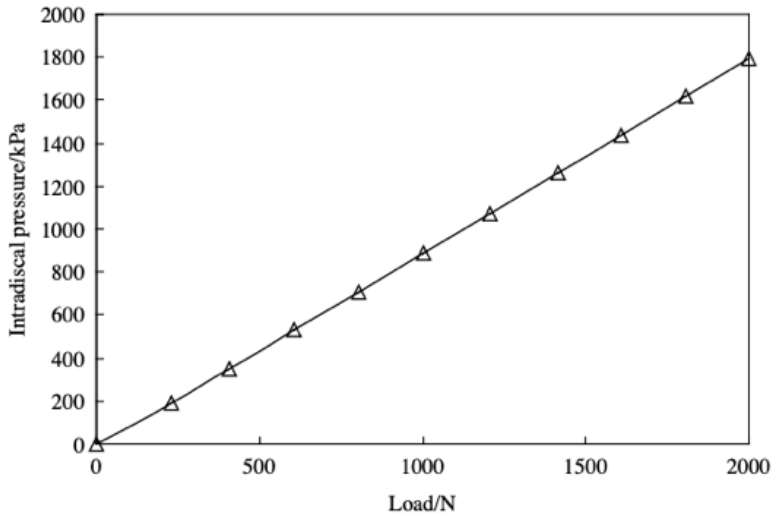



***Figure 3.8.3**: Nucleus load-pressure relationship (Peng et al., 2011)*

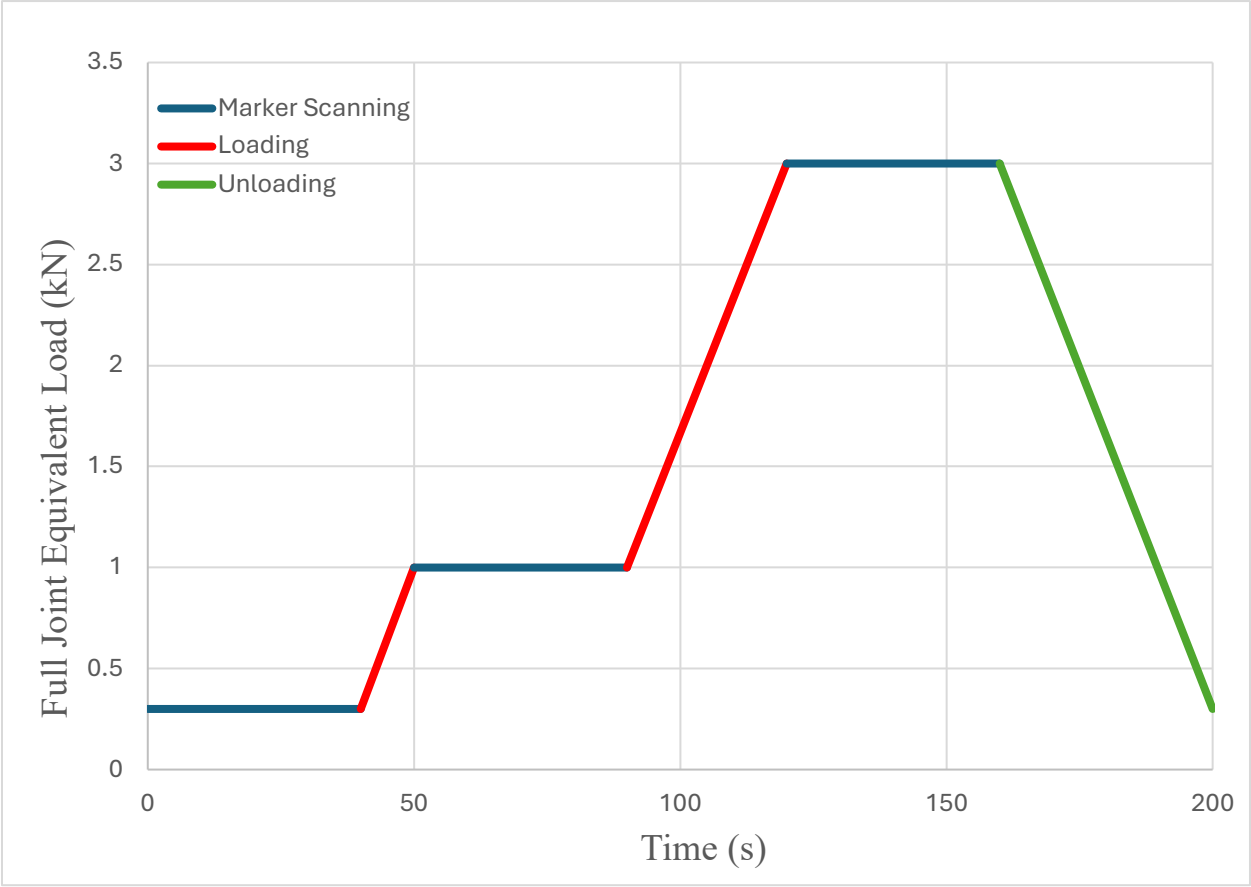



***Figure 3.8.4**: Automated static-ramp and scanning protocol*

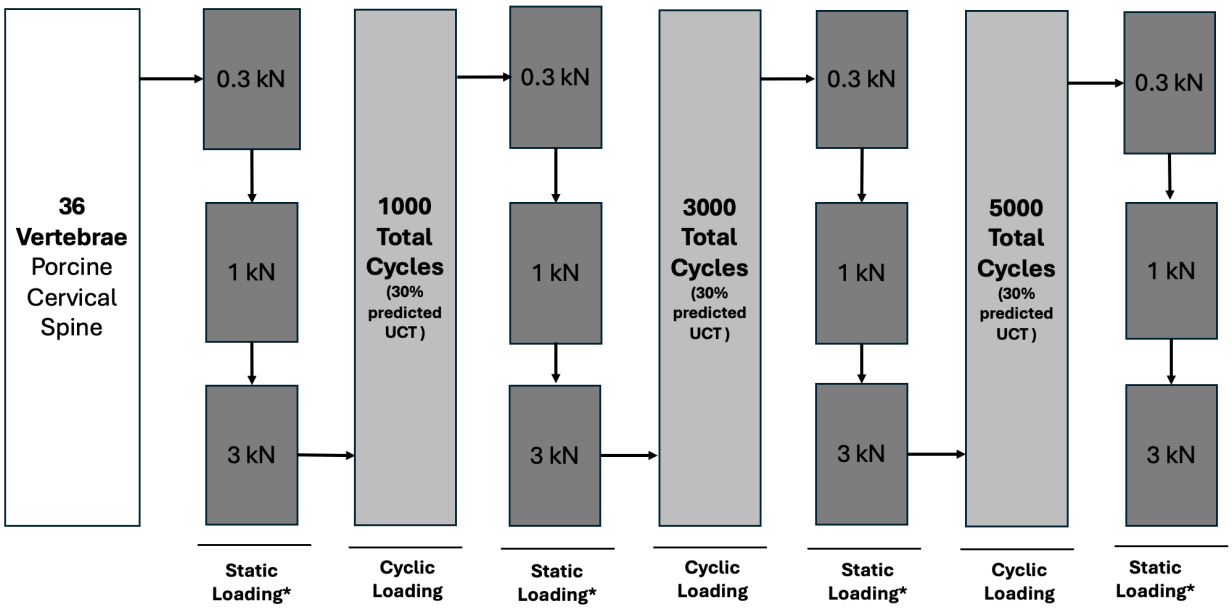



***Figure 3.8.5**: Schematic of Cyclic Loading Protocol*
**Static loads are listed as whole joint equivalent magnitudes*

| | **Whole Joint Force (kN)** | **Nuclear Equivalent Pressure (kPa)** | **Indenter Load Magnitude (kN)*** |
|---|---|---|---|
| Baseline Load | 0.3 | 270 | 0.101 |
| 30% UCT | 3 | 2700 | 1.013 |

***Table 3.1**: Sample Indenter Cyclic Load Calculation Table.*
**A nuclear area of 375 $mm^2$ (estimated average among pilot specimens) is used as an example in the indenter load magnitude column*

| **Whole Joint Force (kN)** | **Nuclear Equivalent Pressure (kPa)** | **Indenter Load Magnitude (kN)*** |
|---|---|---|
| 0.3 | 270 | 0.101 |
| 1 | 900 | 0.338 |
| 3 | 2700 | 1.013 |

***Table 3.2**: Sample Indenter Static Load Calculation Table.*
**A nuclear area of 375 $mm^2$ (estimated average among pilot specimens) is used as an example in the indenter load magnitude column*

$$\text{Indenter Area } (mm^2) \times \text{Nuclear Stress } (kPa) \times 10^{-6} = \text{Applied Load } (kN)$$

***Equation 2**: Nuclear stress to load conversion equation based on indenter area*

### 3.9 Statistical Analysis

All statistical processing was performed using R (Version 3.6.0+, R Foundation for Statistical Computing, Vienna, Austria).

#### 3.9.1 Paired-Endplate Deflection Comparisons

The 36 specimens were divided into six vertebral groups: cranial endplates (C4, C5, C6) and caudal endplates (C3, C4, C5). Endplate deflection measurements were paired for analysis as follows: caudal C3 with cranial C4, caudal C4 with cranial C5**,** and caudal C5 with cranial C6 given these structures share the same joint.

Three separate linear mixed-effects models (LMEM) were used rather than a single combined model because each comparison of interest was within a single joint (superior vs. inferior endplate). Each model analysed deflection as a function of loading magnitude (0.3 kN, 1 kN, and 3 kN), loading cycles (0, 1000, 3000, and 5000 cycles), and endplate group. The proportion of the nucleus-occupying endplate area relative to the whole endplate area was included as a covariate (continuous variable). Furthermore, a nested random-effects structure accounted for repeated measurements by allowing the model to recognize that multiple observations from the same specimen are correlated, while also capturing the fact that endplates within the same joint are of greater similarity than the specimens from other joints.

Homoscedasticity was assessed by examining residuals versus fitted values plots. The normality of residuals was evaluated visually using Normal Q-Q plots. To formally assess residual behavior while accounting for the nested structure of the data (joints within spines), DHARMa, an R package that generates standardized simulated residuals for hierarchical models, was used. Uniformity tests in DHARMa assessed whether residuals were evenly distributed and dispersion tests detected over- or under-spread. Random effects at both the spine and joint-within-spine levels

were inspected with Q-Q plots used to evaluate their approximate normality. In the event of severe violations, the response variable would be log-transformed to improve residual normality and homoscedasticity.

For each LMEM, two sets of post hoc pairwise comparisons were performed. First, estimated marginal means (EMMs) were compared between superior and inferior endplates for each combination of loading magnitude and loading cycle (e.g., Superior vs. Inferior at 0.3 kN and 0 cycles), with Tukey corrections applied to control for multiple testing. This directly assessed differences in endplate deflection between superior and inferior surfaces at each loading condition. Second, post-hoc pairwise comparisons of superior and inferior endplates were performed using differences of EMMs of deflection between consecutive loading cycles (0→1000, 1000→3000, 3000→5000) for each loading magnitude. These contrasts tested whether the rate of change in deflection between loading cycle increments differed between the superior and inferior endplates within a joint for a given loading magnitude (e.g., Superior vs Inferior rate of deflection between 0→1000 at 0.3 kN). Tukey corrections were applied to control for multiple testing.

### 3.9.2 Between Joint Differences

After performing the statistical analysis in Section 3.9.1, notable visual differences were observed in superior and inferior endplate deflection at each spinal level. This prompted investigation into whether spinal joint level influences the magnitude of difference observed between superior and inferior endplate deflection. To quantify this, the difference between superior and inferior deflection measurements was calculated for each joint across each loading condition and magnitude. Absolute differences were used rather than a relative percentage difference because, while not representing a perfect one-to-one comparison, they better highlight anatomical

and material variations between spinal levels. Even when differences are influenced by level-specific size or structural properties, these magnitudes remain physiologically meaningful.

A LMEM was then used to assess whether endplate deflection differences were statistically significant, with joint level (C3C4, C4C5, C5C6), loading magnitude (0.3 kN, 1kN, 3kN), and loading cycles (0, 1000, 3000, 5000) as fixed effects. However, the data structure presented two key challenges: repeated measures within each joint across multiple loading conditions, and the fact that several joints (three C3C4 and C5C6) originated from the same spine. These dependencies violate the assumption of independent observations required for traditional linear models. To account for this, the linear mixed-effects model included random intercepts for joints nested within spines. This allowed the model to account for correlated measurements within the same joint (repeated measures) and similarities among joints from the same spine. By modeling variability at both the spinal and joint levels, the fixed effects of joint level, loading magnitude, and loading cycles could be estimated without bias from repeated or hierarchically structured data.

Homoscedasticity was assessed by generating and examining residuals versus fitted values plots, and the normality of residuals was assessed visually using Normal Q-Q plots. In addition, DHARMa simulated residuals were used to formally test for uniformity and dispersion, which account for the random effects structure in LMEM. Random effects at both the spine and joint-within-spine levels were inspected, with Q-Q plots used to evaluate their approximate normality. In the event of severe violations, the response variable would be log-transformed to better meet model assumptions of normality and homoscedasticity of residuals. Pairwise contrasts were performed between joint levels within each combination of loading magnitude and loading cycle using EMMs, with Tukey adjustment applied to control for multiple comparisons.

# Chapter 4 – Results

## 4.1 C3C4 Endplate Deflections

Model 1 compared superior and inferior endplate deflections within the C3C4 joint. Diagnostic checks confirmed that model assumptions were met.

Significant main effects of loading magnitude and loading cycles were observed. Compared to baseline (0.3 kN, 0 cycles), deflection of both endplates increased by 49 μm at 1 kN ($p < 0.001$) and 194 μm at 3 kN ($p < 0.001$). Similarly, repeated cycles increased deflection by 71 μm at 1000 cycles, 91 μm at 3000 cycles, and 103 μm at 5000 cycles (all $p < 0.001$). The proportion of the nucleus occupying the endplate showed a trend toward predicting deflection though it did not reach significance ($p = 0.062$). Average endplate area, nucleus occupying area, proportion of the nucleus occupying area, and applied forces can be found in Table 4.1 for both endplates.

A significant two-way interaction was observed whereby after accounting for the main effects of loading magnitude and cycle count, the inferior endplate deflected 53 μm more than the superior endplate at a 3 kN loading magnitude ($p < 0.01$). No three-way interactions reached statistical significance, indicating that endplate group differences were largely consistent across loading cycles and lower loading magnitudes.

Post-hoc pairwise comparisons of superior and inferior endplate EMMs for each combination of loading magnitude and cycle count found inferior endplate deflection to be only significantly greater ($p < 0.05$) at 0 cycles with a 3 kN loading magnitude. Results, including 95% confidence intervals, are shown in Figure 4.1.1.

Post hoc pairwise comparisons of the rate of change in deflection between consecutive loading cycles (0→1000, 1000→3000, 3000→5000) for superior and inferior endplates were performed at each loading magnitude. No significant differences in the rate of deflection were

found between either endplate. Results are illustrated in Figure 4.1.2. The rate of deflection between cycle counts at both endplate levels can be seen in Table 4.2.

Model and pairwise comparison outputs can be found in the Appendices in Tables 8.1, 8.2, and 8.3

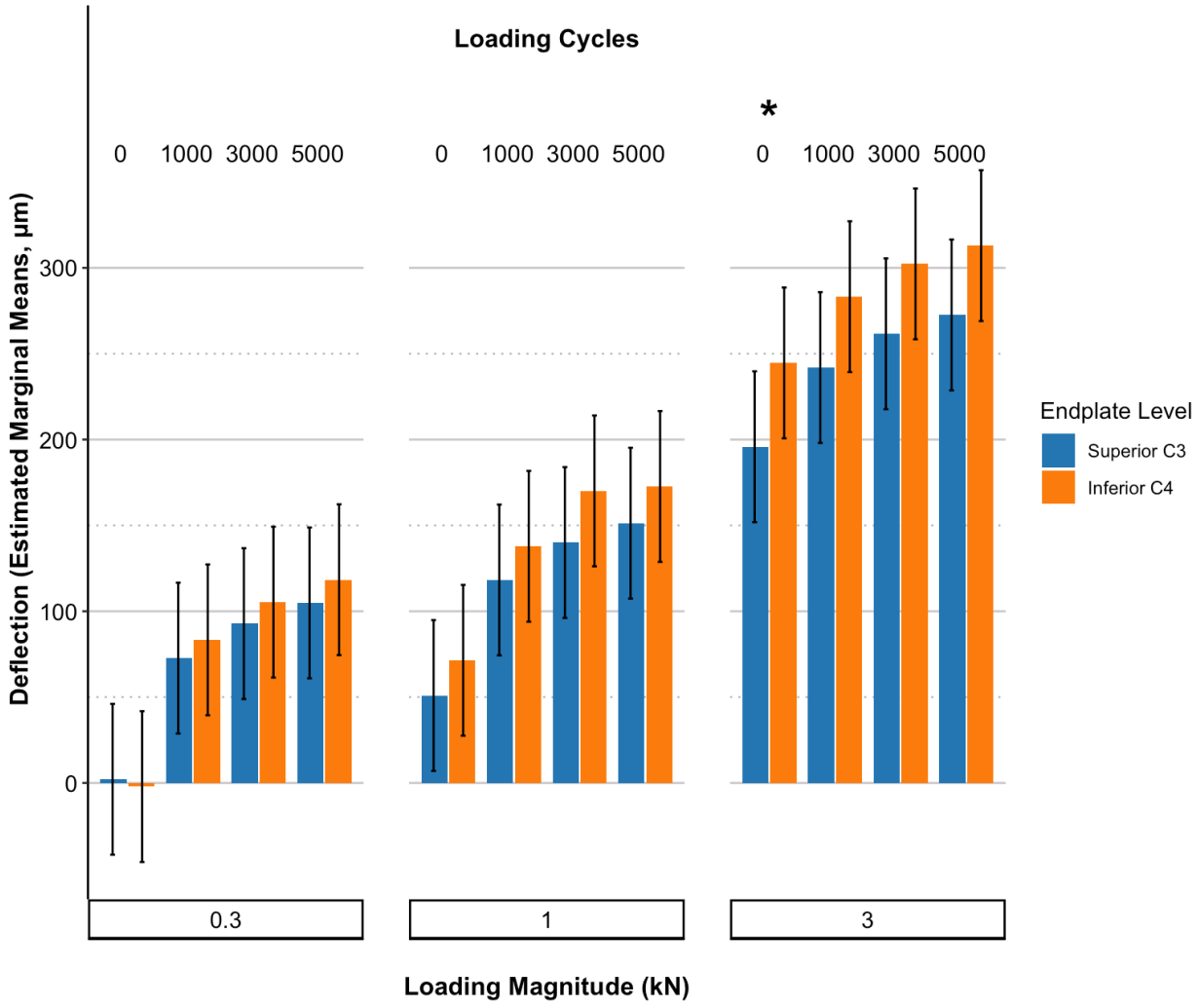



***Figure 4.1.1**: C3C4 endplate deflections measured throughout the experimental process.*

** Significant difference between endplates at the indicated measurement ($p < 0.05$)*

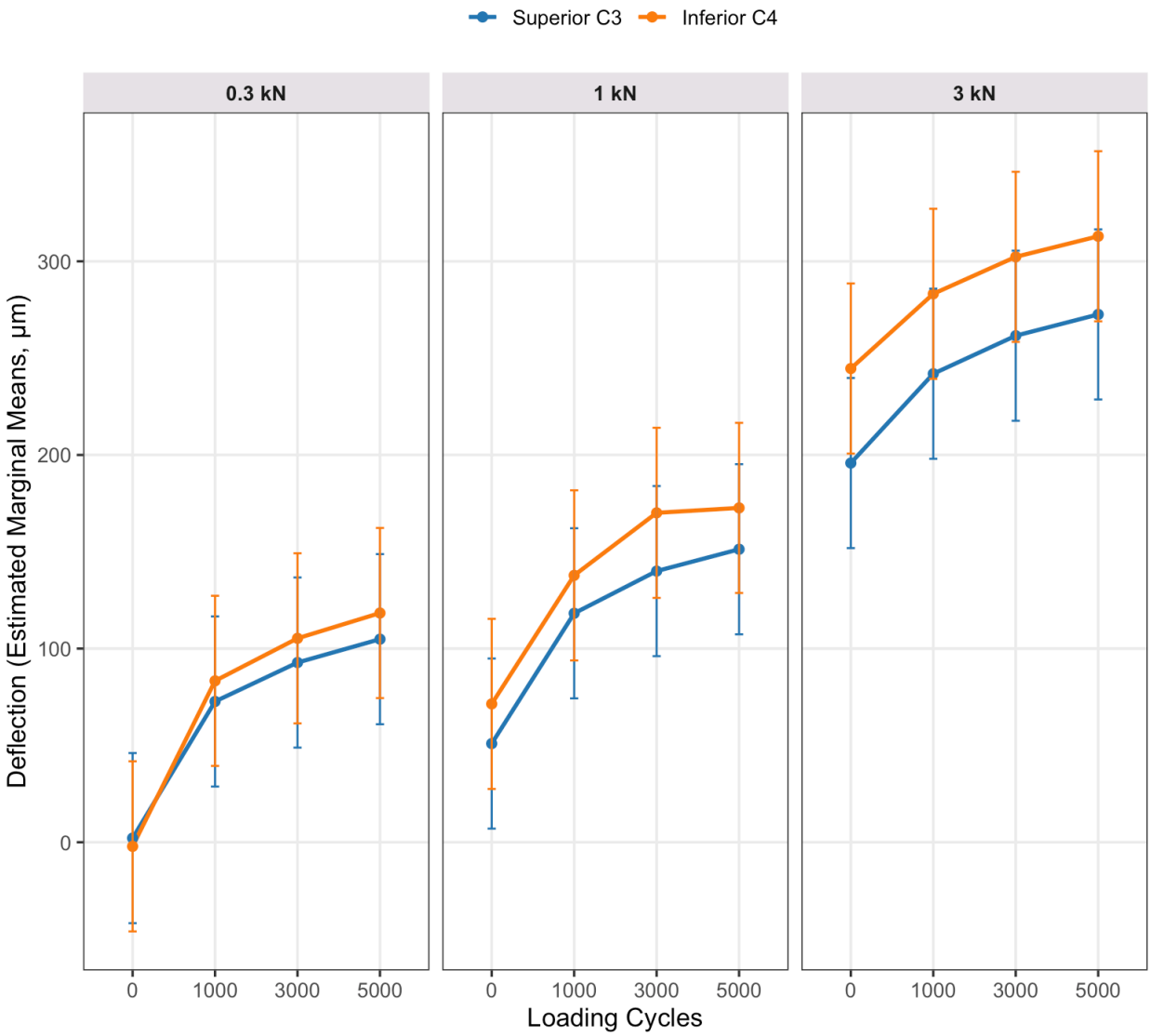



***Figure 4.1.2**: Estimated marginal means of C3C4 endplate deflection across loading cycles (0, 1000, 3000, 5000) at each loading magnitude (0.3, 1, and 3 kN) for visualizing differences in the rate of deflection.*

*No significant differences in deflection change between endplates were observed across cycle increments.*
*Error bars represent 95% confidence intervals.*

***Table 4.1**: Average Endplate Areas, Nucleus Area, Proportion of Nucleus Occupying Area, and Applied Force Magnitudes of superior C3 and inferior C4 endplates*

| | Endplate Area ($mm^2$), Mean (SD) | Nucleus Area ($mm^2$), Mean (SD) | Proportion of Nucleus Area (%), Mean (SD) | 0.3 kN Full Joint Equivalent Load (kN), Mean (SD) | 1 kN Full Joint Equivalent Load (kN), Mean (SD) | 3 kN Full Joint Equivalent Load (kN), Mean (SD) | 30% Full Joint Equivalent UCT (kN), Mean (SD) |
|---|---|---|---|---|---|---|---|
| Superior C3 | 692 (76) | 376 (77) | 54 (8) | 0.101 (0.021) | 0.338 (0.07) | 1.014 (0.211) | 1.018 (0.290) |
| Inferior C4 | 613 (53) | 339 (56) | 56 (8) | 0.092 (0.015) | 0.305 (0.051) | 0.916 (0.153) | 0.828 (0.178) |

***Table 4.2**: Rate of change in deflection between superior C3 and inferior C4 endplates at differing cycle increments*
*Blank cells indicate no significance.*

| Force (kN) | Cycle Increment | Change in Deflection (µm/1000 Cycles) | | Significance |
|---|---|---|---|---|
| | | C3 Superior | C4 Inferior | |
| 0.3 | 0 → 1000 | 71 | 85 | |
| | 1000 → 3000 | 10 | 11 | |
| | 3000 → 5000 | 3 | 7 | |
| 1 | 0 → 1000 | 67 | 66 | |
| | 1000 → 3000 | 11 | 16 | |
| | 3000 → 5000 | 6 | 1 | |
| 3 | 0 → 1000 | 46 | 39 | |
| | 1000 → 3000 | 10 | 10 | |
| | 3000 → 5000 | 6 | 5 | |

### 4.2 C4C5 Deflections

Model 2 compared superior and inferior endplate deflections within the C4C5 joint. Diagnostic checks confirmed that model assumptions were met.

Significant main effects of loading magnitude and loading cycles were observed. Relative to baseline (0.3 kN, 0 cycles), deflection of both endplates increased by 47 µm at 1 kN ($p < 0.001$)

and 170 μm at 3 kN ($p < 0.001$). Similarly, repeated cycles increased deflection by 46 μm at 1000 cycles, 60 μm at 3000 cycles, and 66 μm at 5000 cycles (all $p < 0.001$). The proportion of the nucleus occupying the endplate was not predictive of deflection ($p = 0.57$). Average endplate area, nucleus occupying area, proportion of the nucleus occupying area, and applied forces can be found in Table 4.3 for both endplates.

Several significant two-way interactions were observed between group and loading magnitude. After accounting for the main effects of loading magnitude and cycles, the inferior endplate deflected 32 μm more than its superior counterpart at 1 kN ($p < 0.05$), increasing to 105 μm at 3 kN ($p < 0.001$). With repeated cycles, the inferior endplate deflected 84, 98, and 104 μm more than the superior endplate at 1000, 3000, and 5000 cycles, respectively (all $p < 0.001$).

Three-way interactions indicated partial attenuation of group differences at high loading magnitudes with repeated cycles. At 3 kN and 1000, 3000, and 5000 cycles, the difference between superior and inferior endplates were reduced by 57, 62, and 66 μm, respectively, relative to the sum of the individual magnitude and cycle effects (all $p < 0.01$). No significant three-way interactions were observed at 1 kN.

Post-hoc pairwise comparisons of superior and inferior endplates were performed using EMMs for each combination of loading magnitude and cycle count. Inferior endplate deflection was significantly greater ($p < 0.01$) under all conditions, except at 0 cycles for 0.3 kN and 1 kN loading levels. Results, including 95% confidence intervals, are shown in Figure 4.2.1.

Post hoc pairwise comparisons of the rate of change in deflection between consecutive loading cycles (0→1000, 1000→3000, 3000→5000) for superior and inferior endplates were performed at each loading magnitude. The inferior endplate was found to deflect at a significantly greater rate between 0 and 1000 loading cycles at 0.3 kN ($p < 0.001$), 1 kN ($p < 0.001$), and 3 kN

($p < 0.05$) compared to the superior endplate. Results are illustrated in Figure 4.2.2. The rate of deflection between cycle counts at both endplate levels can be seen in Table 4.4.

Model and pairwise comparison outputs can be found in the Appendices in Tables 8.4, 8.5, and 8.6.

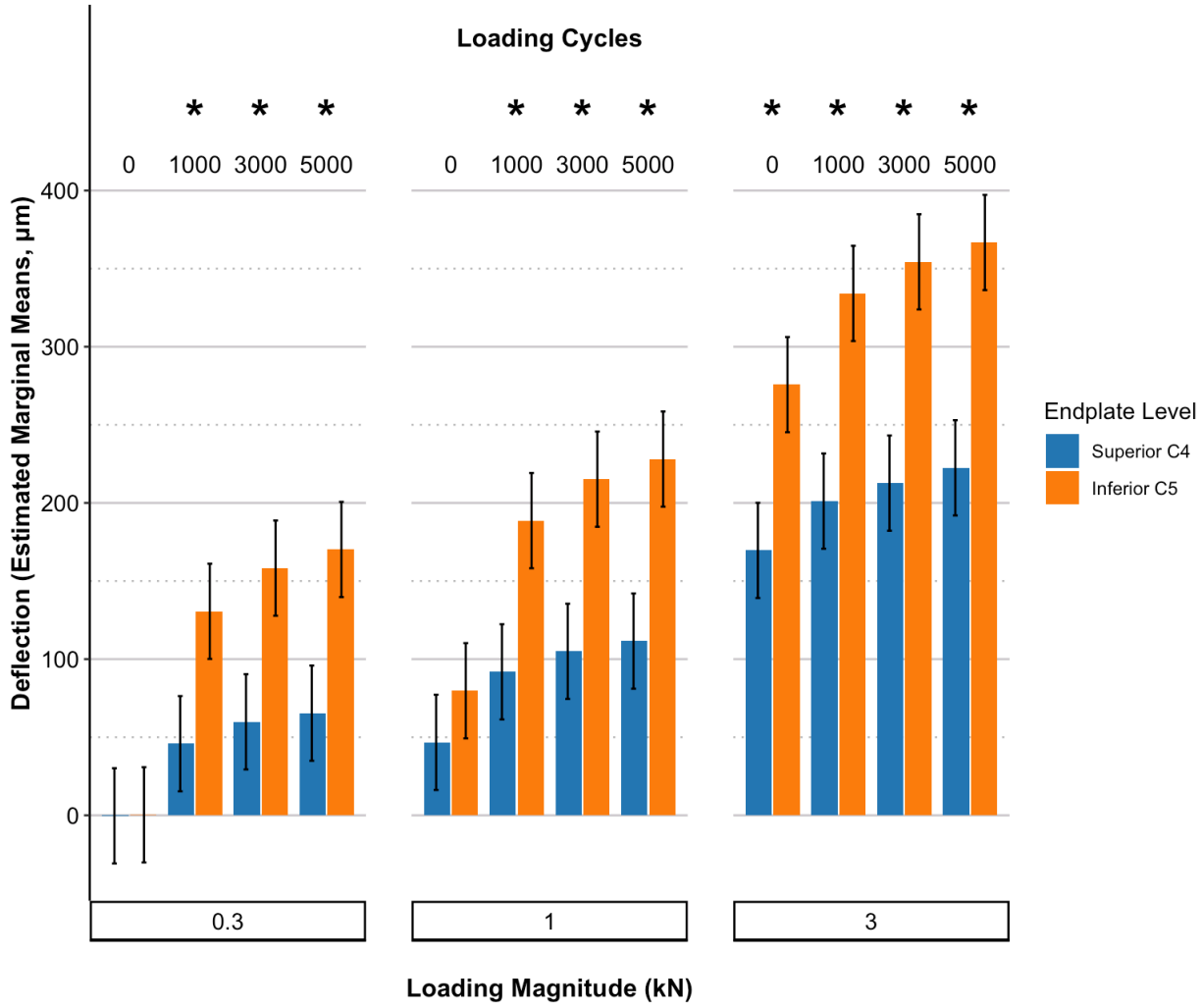



***Figure 4.2.1**: C4C5 endplate deflections measured throughout the experimental process with 95% confidence intervals.*

** Significant difference between endplates at the indicated measurement ($p < 0.01$)*

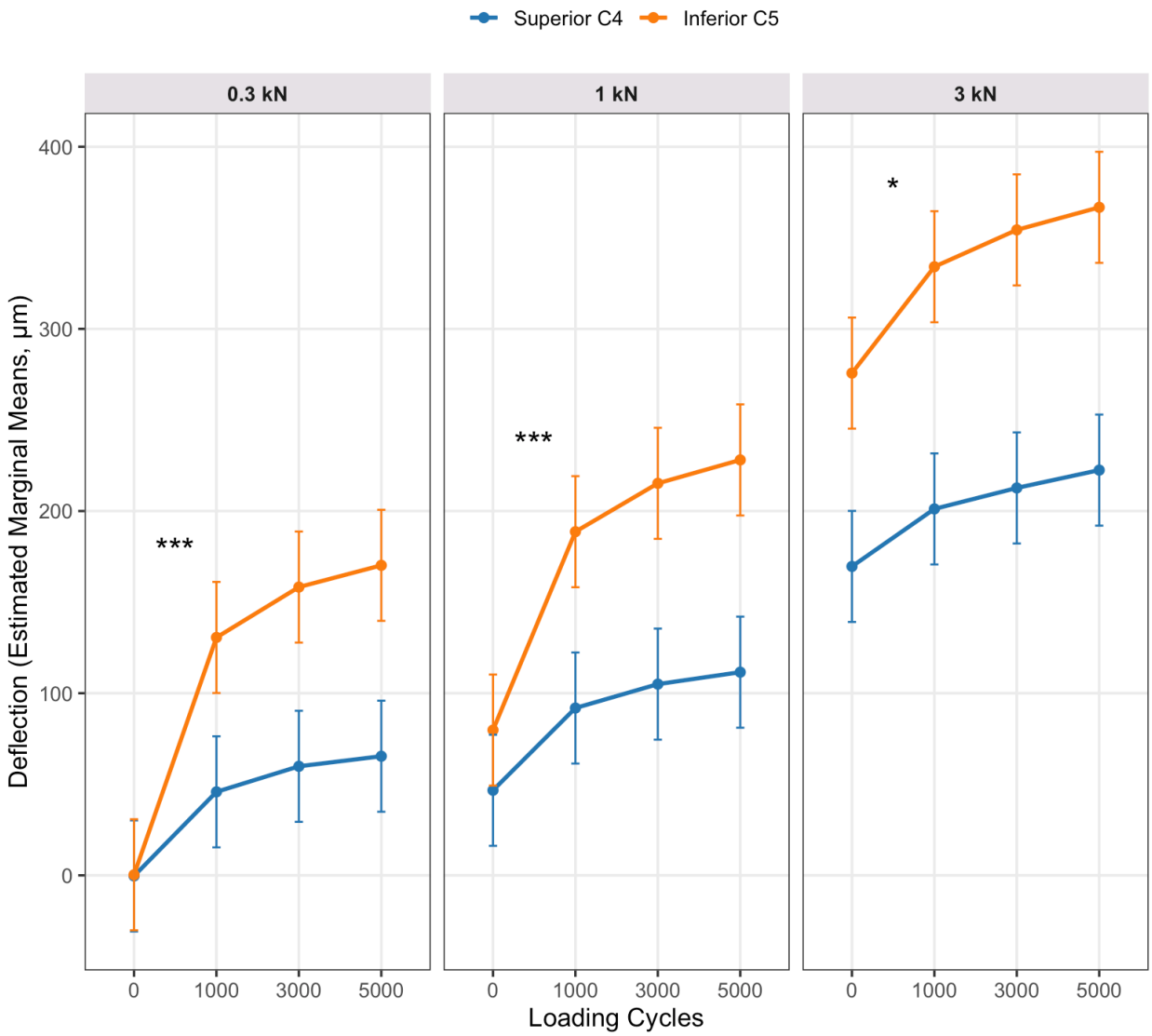



***Figure 4.2.2**: Estimated marginal means of C4C5 endplate deflection across loading cycles (0, 1000, 3000, 5000) at each loading magnitude (0.3, 1, and 3 kN) for visualizing differences in the rate of deflection.*

*Error bars represent 95% confidence intervals.*
**** ($p < 0.001$) * ($p < 0.05$)*

***Table 4.3**: Average Endplate Areas, Nucleus Area, Proportion of Nucleus Occupying Area, and Applied Force Magnitudes of superior C4 and inferior C5 endplates*

| | Endplate Area ($mm^2$), Mean (SD) | Nucleus Area ($mm^2$), Mean (SD) | Proportion of Nucleus Area (%), Mean (SD) | 0.3 kN Full Joint Equivalent Load (kN), Mean (SD) | 1 kN Full Joint Equivalent Load (kN), Mean (SD) | 3 kN Full Joint Equivalent Load (kN), Mean (SD) | 30% Full Joint Equivalent UCT (kN), Mean (SD) |
|---|---|---|---|---|---|---|---|
| Superior C4 | 718 (32) | 394 (70) | 55 (11) | 0.107 (0.019) | 0.355 (0.064) | 1.065 (0.191) | 1.109 (0.189) |
| Inferior C5 | 615 (23) | 345 (35) | 56 (7) | 0.093 (0.010) | 0.310 (0.032) | 0.931 (0.096) | 0.839 (0.080) |

***Table 4.4**: Rate of change in deflection between superior C4 and inferior C5 endplates at differing cycle increments. *** ($p < 0.001$) * ($p < 0.05$)*
*Blank cells indicate no significance.*

| Force (kN) | Cycle Increment | Change in Deflection (μm/1000 Cycles) | | Significance |
|---|---|---|---|---|
| | | C4 Superior | C5 Inferior | |
| 0.3 | 0 → 1000 | 46 | 130 | *** |
| | 1000 → 3000 | 7 | 14 | |
| | 3000 → 5000 | 3 | 6 | |
| 1 | 0 → 1000 | 45 | 109 | *** |
| | 1000 → 3000 | 7 | 14 | |
| | 3000 → 5000 | 4 | 7 | |
| 3 | 0 → 1000 | 31 | 58 | |
| | 1000 → 3000 | 6 | 10 | |
| | 3000 → 5000 | 5 | 6 | |

### 4.3 C5C6 Deflections

Model 3 compared endplates within the C5C6 joint. Diagnostic checks confirmed that model assumptions were met.

Significant main effects of both loading magnitude and loading cycles were observed. Relative to baseline (0.3 kN, 0 cycles), deflection increased by 58 μm at 1 kN ($p < 0.001$) and 205 μm at 3 kN ($p < 0.001$). Similarly, with repeated cycles, deflection rose by 64 μm at 1000 cycles,

76 μm at 3000 cycles, and 83 μm at 5000 cycles (all $p < 0.001$). The proportion of the nucleus occupying area relative to endplate size was not predictive of deflection ($p > 0.70$). Average endplate area, nucleus occupying area, proportion of the nucleus occupying area, and applied forces can be found in Table 4.5 for both endplates.

Several two-way interactions were significant. After accounting for the main effects of loading magnitude and cycles, the inferior endplate deflected 32 μm more than the superior endplate at 1 kN ($p > 0.01$), increasing to 90 μm at 3 kN ($p < 0.001$). Likewise, with repeated cycles, the inferior endplate deflected 57 μm, 64 μm, and 67 μm more than the superior endplate at 1000, 3000, and 5000 cycles, respectively (all $p < 0.001$).

Three-way interactions showed that these group differences were partially attenuated at high magnitude with repeated cycles. At 3 kN and 1000, 3000, and 5000 cycles, the difference between endplate groups was 40-45 μm beyond what would be predicted by the sum of the main effects and two-way interaction (all $p < 0.05$).

Post-hoc pairwise comparisons of superior and inferior endplates were performed using EMMs for each combination of loading magnitude and cycle count. Inferior endplate deflection was significantly greater ($p < 0.01$) under all conditions, except at 0 cycles for 0.3 kN and 1 kN loading levels. Results, including 95% confidence intervals, are shown in Figure 4.3.1.

Post hoc pairwise comparisons of the rate of change in deflection between consecutive loading cycles (0→1000, 1000→3000, 3000→5000) for superior and inferior endplates were performed at each loading magnitude. The inferior endplate was found to deflect at a significantly greater rate between 0 and 1000 loading cycles at 0.3 kN ($p < 0.001$) and 1 kN ($p < 0.01$) compared to the superior endplate. Results are summarized in Figure 4.3.2. The rate of deflection between cycle counts at both endplate levels can be seen in Table 4.6.

Model and pairwise comparison outputs can be found in the Appendices in Tables 8.7. 8.8, and 8.9.

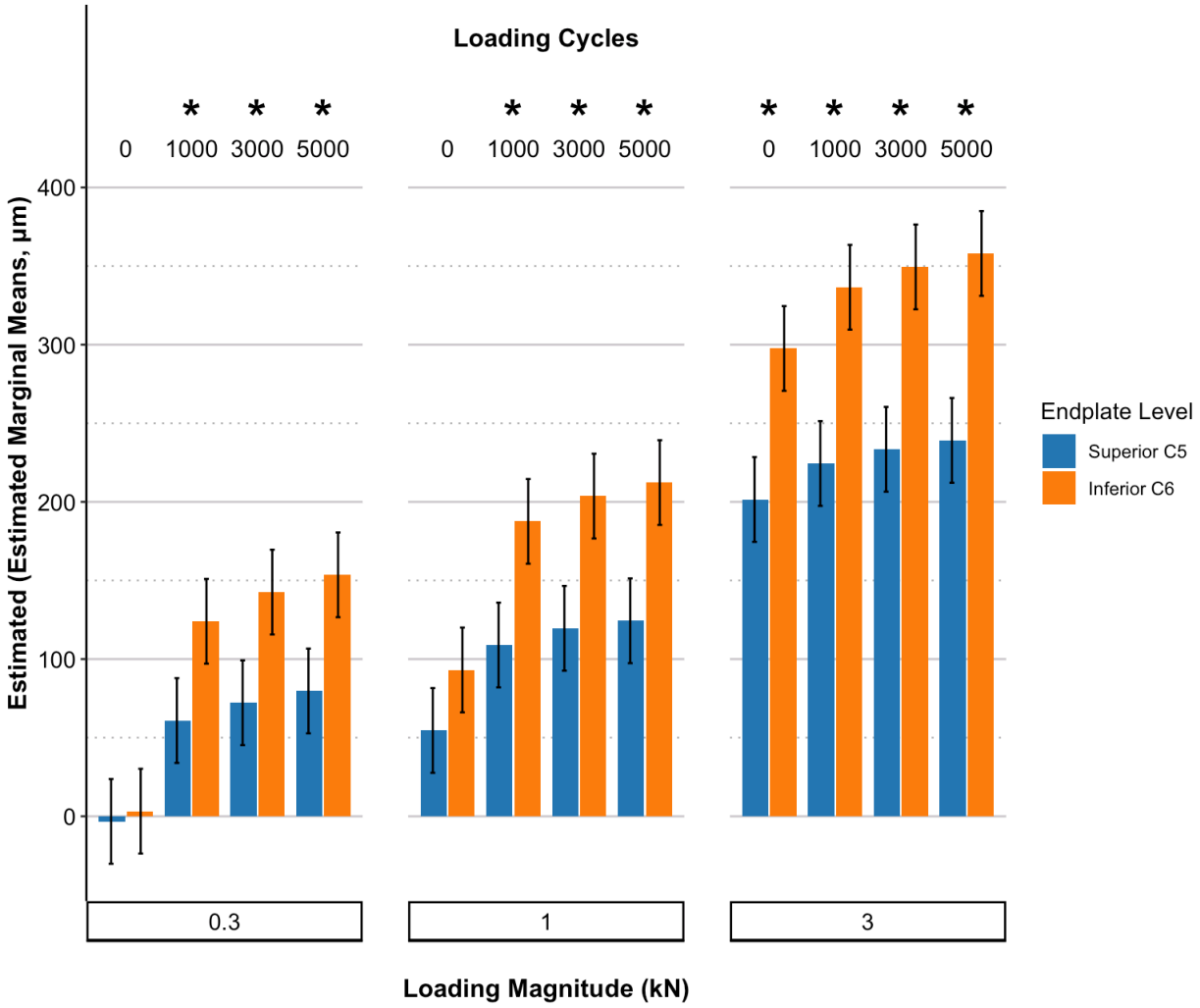



***Figure 4.3.1**: C5C6 endplate deflections measured throughout the experimental process with 95% confidence intervals.*

** Significant difference between endplates at the indicated measurement ($p < 0.01$)*

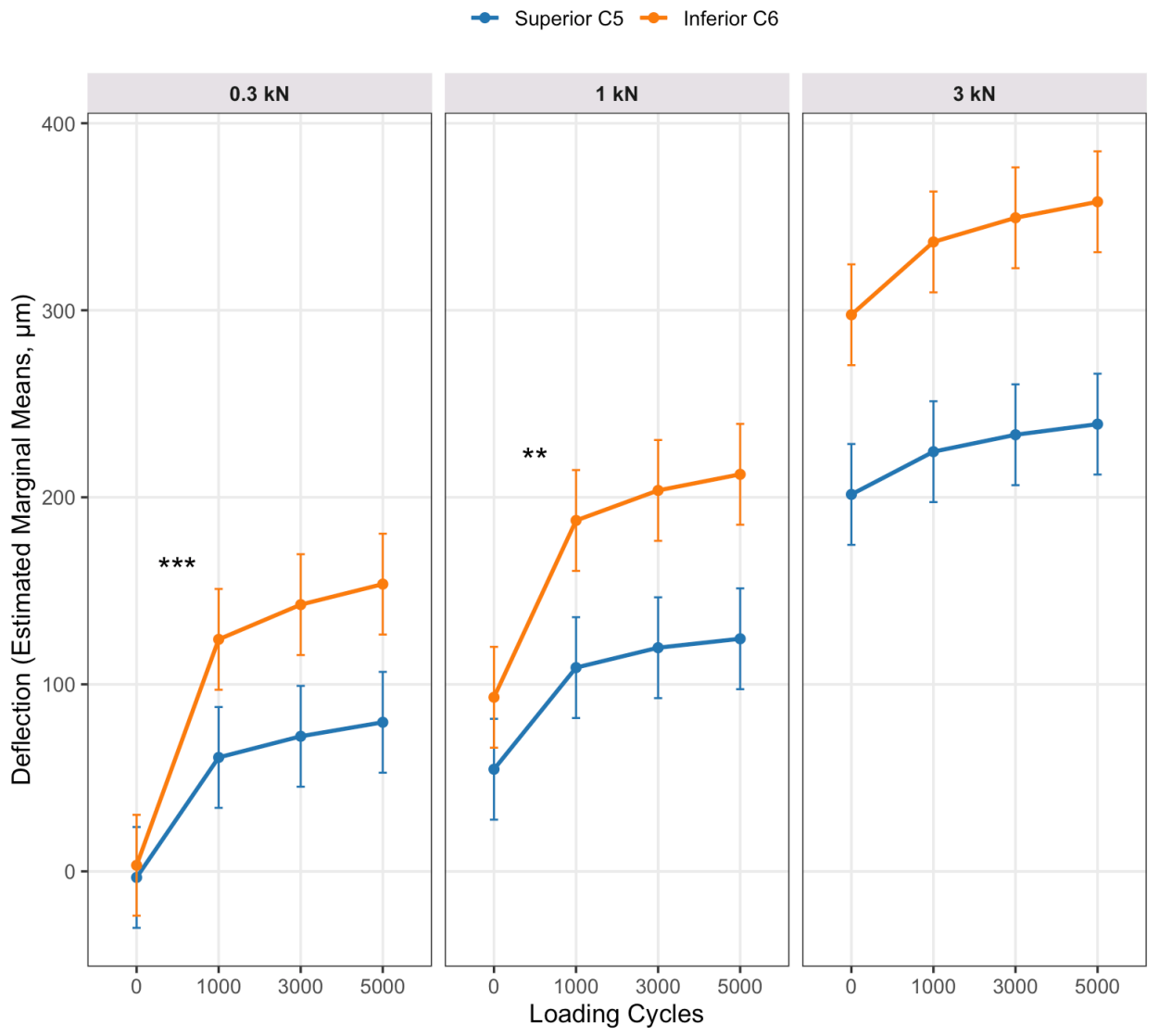



***Figure 4.3.2**: Estimated marginal means of C5C6 endplate deflection across loading cycles (0, 1000, 3000, 5000) at each loading magnitude (0.3, 1, and 3 kN) for visualizing differences in the rate of deflection.*

*Error bars represent 95% confidence intervals.*
**** ($p < 0.001$) ** ($p < 0.01$)*

***Table 4.5**: Average Endplate Areas, Nucleus Area, Proportion of Nucleus Occupying Area, and Applied Force Magnitudes of superior C5 and inferior C6 endplates*

| | Endplate Area ($mm^2$), Mean (SD) | Nucleus Area ($mm^2$), Mean (SD) | Proportion of Nucleus Area (%), Mean (SD) | 0.3 kN Full Joint Equivalent Load (kN), Mean (SD) | 1 kN Full Joint Equivalent Load (kN), Mean (SD) | 3 kN Full Joint Equivalent Load (kN), Mean (SD) | 30% Full Joint Equivalent UCT (kN), Mean (SD) |
|---|---|---|---|---|---|---|---|
| Superior C5 | 682 (68) | 376 (41) | 55 (4) | 0.101 (0.011) | 0.338 (0.037) | 1.014 (0.112) | 1.016 (0.198) |
| Inferior C6 | 613 (84) | 365 (54) | 60 (4) | 0.099 (0.015) | 0.329 (0.050) | 0.987 (0.149) | 0.904 (0.239) |

***Table 4.6**: Rate of change in deflection between superior C5 and inferior C6 endplates at differing cycle increment. *** ($p < 0.001$) ** ($p < 0.01$)*

*Blank cells indicate no significance.*

| Force (kN) | Cycle Increment | Change in Deflection (µm/1000 Cycles) | | Significance |
|---|---|---|---|---|
| | | C5 Superior | C6 Inferior | |
| 0.3 | 0 → 1000 | 64 | 130 | *** |
| | 1000 → 3000 | 6 | 14 | |
| | 3000 → 5000 | 4 | 6 | |
| 1 | 0 → 1000 | 54 | 109 | ** |
| | 1000 → 3000 | 5 | 14 | |
| | 3000 → 5000 | 2 | 7 | |
| 3 | 0 → 1000 | 23 | 58 | |
| | 1000 → 3000 | 4.5 | 10 | |
| | 3000 → 5000 | 3 | 6 | |

### 4.4 Effect of Joint Level

Model 4 compared endplates across C3C4, C4C5, and C5C6 joints. Diagnostic checks confirmed that model assumptions were met. A main effect of loading magnitude was observed, with deflection increasing by 53 µm at 3 kN ($p < 0.001$) relative to baseline. The main effect of repeated cycles was not statistically significant.

Two-way interactions, representing differences beyond the main effects of loading magnitude and cycles, showed that at 3 kN, the difference in deflection between inferior and superior endplates of C4C5 and C5C6 joints was 52 μm and 37 μm more than C3C4, respectively ($p < 0.001$, $p < 0.05$). With repeated cycles, the magnitude of the superior–inferior deflection difference in the C4C5 joint increased relative to C3C4, rising by 69 μm ($p < 0.001$) at 1000 cycles, 81 μm ($p < 0.001$) at 3000 cycles, and 86 μm ($p < 0.001$) at 5000 cycles. Similarly, C5C6 showed an increase of 42 μm ($p < 0.05$) at 1000 cycles, 47 μm at 3000 cycles ($p < 0.01$), and 50 μm at 5000 cycles ($p < 0.01$), respectively, compared to the C3C4 joint. No three-way interactions reached statistical significance.

Post-hoc pairwise comparisons of superior–inferior endplate differences across joint levels were conducted using EMMs at each loading magnitude and cycle combination. Only a significant difference existed between C3C4 and C4C5 joints ($p < 0.05$) under all conditions, except at 0 cycles for 0.3 kN, 1 kN, and 3 kN loading levels. Results, including 95% confidence intervals, are summarized in Figure 4.4.1.

Model and pairwise comparison outputs can be found in the Appendices in Tables 8.10 and 8.11.

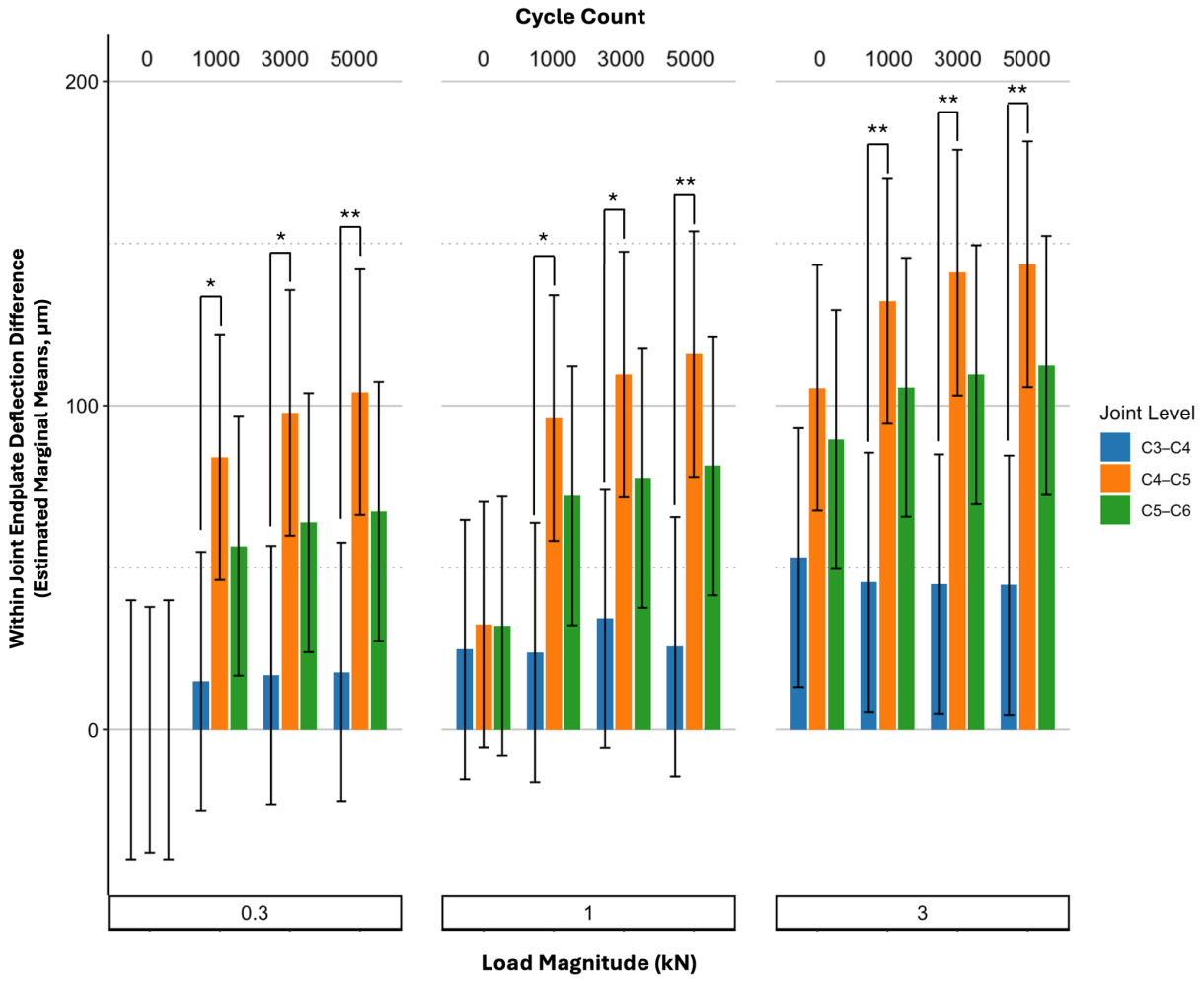



***Figure 4.4.1****: Comparison of differences in endplate deflections across C3C4, C4C5, and C5C6 joints with 95% confidence intervals.*

** ($p < 0.05$), ** ($p < 0.01$)*

# Chapter 5 - Discussion

This study developed methodology that enabled the comparison of deflection in superior and inferior spinal joint endplates in response to novel physiologically relevant cyclic loading. Partially supporting the first hypothesis of this study, FSUs at all levels beyond baseline (0 cycles, 0.3 kN) exhibited greater deflection in the inferior endplate, with only the inferior endplates of C4C5 and C5C6 showing significantly higher rates of deflection during the first 1000 cycles of cyclic loading. Partially consistent with the second hypothesis, the most centrally oriented joint (C4C5) displayed statistically greater differences between superior and inferior endplate deflection compared to C3C4 but not C5C6. Lastly, this study failed to support the third hypothesis, in that the proportion of the nucleus occupying the endplate surface was not a significant determinant of endplate deflection across all vertebral levels. The following sections will discuss the likely causes of these observations.

## 5.1 Comparison to Previously Measured Values

Hulme et al. (2008) reported similar findings to the present study, observing greater deflection in the inferior endplates of intact spinal joints using micro-CT imaging. While their experiment employed prolonged, stepwise static loading at differing magnitudes than the cyclic loading used here, some overlap exists. As summarized in Table 5.1, the present study's 1 kN and interpolated 1.75 kN whole joint equivalent loads (Figure 5.1.1) at 0 cycles showed greater endplate deflections. Notably, the magnitude of the difference between superior and inferior endplates in both studies was similar, ranging from 20 – 40 μm.

One potential cause for Hulme et al. (2008) demonstrating smaller endplate deflections overall is the use of sustained static loading required for CT scanning. Prolonged static loading

leads to reduced intradiscal fluid pressure due to water expulsion (McMillan et al., 1996), thereby diminishing endplate deformation. This relationship was evident within their study, which showed an increase ranging between 13 and 29 μm in endplate deflection when comparing 45-minute-long whole vertebral scans from a brief 8-minute endplate-only scans. In contrast, the present study's use of a rigid indenter is unaffected by fluid loss, perhaps enabling greater endplate deflections through maintained stress application. Given our inability to account for indenter deformation, as further discussed in 5.7.2, some deformation of the indenter may have contributed to magnitude differences. However, there was no plastic deformation of the indenters for the loads applied (Section 3.6) and elastic deformation is assumed to be consistent at a load level and minimal.

Another possible source for Hulme et al. (2008) observing lesser endplate deflections is the combination of intervertebral fluid loss and the use of intact FSUs, likely resulting in the offloading of stress from the central, nucleus-facing region of the endplate. This occurs through the shifting of load transmission toward the periphery of the endplate and cortical shell through contact with the adjacent vertebra (Adams et al., 1996; van Dieën et al., 2001) as well as facet joints bearing a greater proportion of the joint's load (Bashkuev et al., 2020; Fujiwara et al., 1999). Furthermore, the intact annulus of spinal joints and relatively low compression forces allows for elastic deformation of annular fibers to change the volume of the nuclear cavity and reduce nuclear pressures, thereby decreasing the load transmitted to the endplate and contributing to lower measured deflections (Biggemann et al., 1988; Brinckmann et al., 1983). These sources of reductions in endplate deflection were not possible in this project's experimental setup as the tested endplate always experienced the full stress of the indenter with no peripheral contact at any point shunting force away from the central nuclear region.

While not identical, the similarity of values between this study and Hulme et al. (2008) lends support to the precision of the present methodology and its measured outcomes. Admittedly, a 20 μm difference in a 30 μm measurement represents a large relative deviation; however, it is important to consider the true scale at hand. For reference, the width of a human hair ranges from 30 to 80 μm (Geneviève et al., 2016; Singh, 2009) meaning these discrepancies are quite literally on the scale of splitting hairs. From this perspective, one might argue that such small absolute differences are practically insignificant, particularly given the distinct experimental models, specimen histories, and measurement uncertainties involved. As discussed in Section 2.6, even the micro-CT systems previously used to assess endplate deflection had resolutions between 37 and 82 μm (Hulme et al., 2008; Jackman et al., 2014), relying on sub-voxel interpolation to achieve finer precision. Therefore, emphasizing absolute numerical differences may be inappropriate. Instead, the key takeaway here may be the general agreement in the pattern of endplate deflection observed between micro-CT and 3D printer–based indenter methods, particularly at the lower force magnitudes used in this comparison.

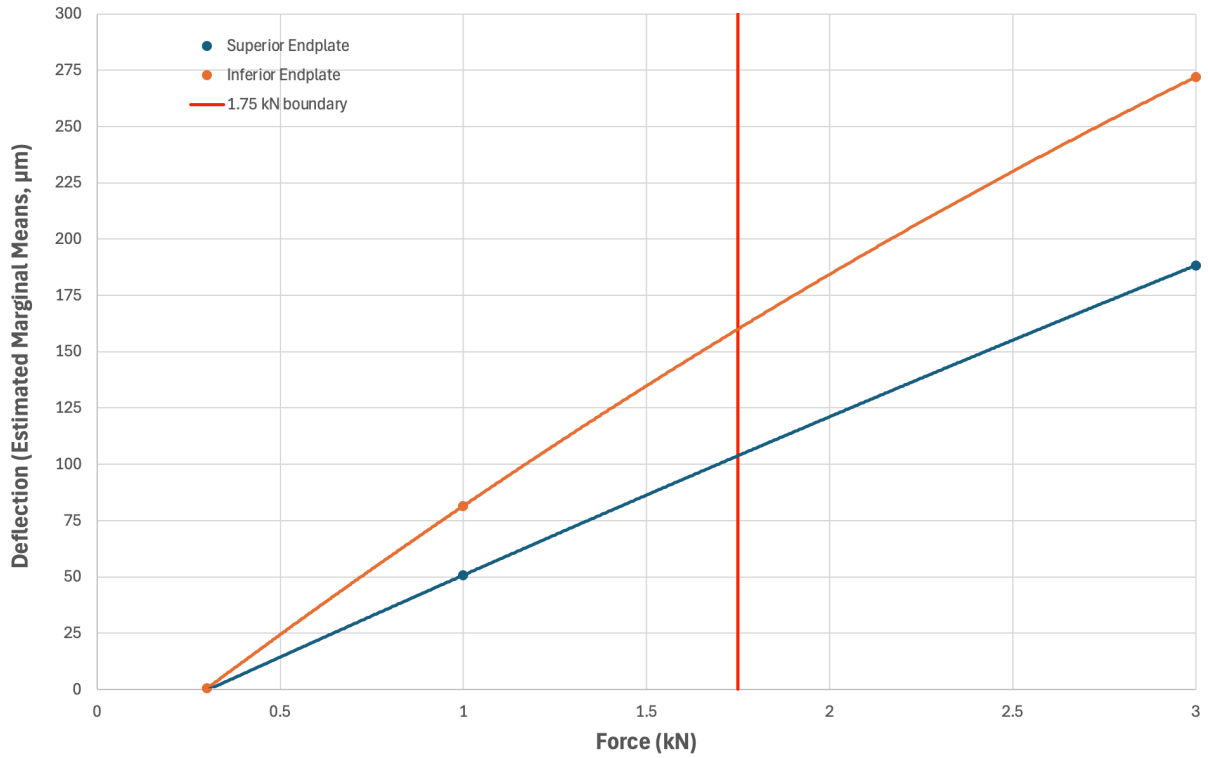



***Figure 5.1**: Interpolation of mean endplate deflection across all spinal joint levels at 0 cycles to estimate deflections corresponding to the 1.5–2 kN whole-joint load reported by Hulme et al. (2008). An intermediate value of 1.75 kN was used, as the original study reported a load range due to normalization to stress.*

***Table 5.1**: Comparison of Hulme et al.'s endplate deflection measurements at 1 and 1.75 kN with the present study's estimated endplate deflection at 0 cycles.*

| Force Magnitude (kN) | Source | Superior Endplate Deflection (µm) | Inferior Endplate Deflection (µm) |
|---|---|---|---|
| 1 | Hulme et al. (2008) | 30 | 52 |
| | This Study | 51 | 80 |
| 1.75 | Hulme et al. (2008) | 72 | 113 |
| | This Study | 113 | 158 |

## 5.2 The Validity of Assessing Injury Risk Through Endplate Deflection Patterns

The most pronounced differences in deflection rates between superior and inferior endplates occurred during the first 1,000 cycles, with the inferior endplate exhibiting a faster initial response. Both endplates follow an asymptotic relationship between deflection and cycle count, although the inferior surface responds more rapidly at the outset. This pattern, combined with greater absolute deflections suggests that the inferior endplate may develop microdamage more quickly than its superior counterpart. While this interpretation is consistent with the higher injury incidence reported for the inferior endplate (Fujiwara et al., 2019; Ortiz & Bordia, 2011), a potential critique is that the observed differences could reflect recoverable fluid loss rather than an intrinsic susceptibility to deflection-induced damage.

However, it is unlikely that fluid loss alone drives these differing deflection responses when considering the structural dimensions of the endplate components. Cartilaginous endplate thickness ranges from 0.1 to 1.6 mm, decreasing toward the central nucleus region (Berg-Johansen et al., 2018; Roberts et al., 1989). Given the high fidelity of endplate surface scans and the tight fit of the indenter (Section 3.6), the indenter center contacts the thinnest central region of the cartilaginous endplate. Maximal deflection in the inferior endplate often approached or exceeded 350 μm, far exceeding the minimal ~0.1 mm thickness of the central cartilage. Even assuming the hyaline cartilage is fully compressed to a height of 0, around 200 μm of displacement would still be taken up by the bony endplate. With the bony endplate ranging from 700 to 800 μm in thickness (Wang et al., 2011), this corresponds to roughly 25% compression of its original height. While exact failure strains for the bony endplate are not well-defined, trabecular bone typically has an ultimate strain of 1–2.5% (Chang et al., 1999; Turner, 1989). Since endplate deflection is largely dictated by the strength of this underlying cancellous structure (Holmes et al., 1993; Jackman et

al., 2014) and measured deflections likely exceed strains necessary for causing damage in the trabecular bone, it is reasonable to conclude that the inferior endplate's greater deflection indicates higher injury potential.

As a result, this link between endplate deflection and injury further challenges the notion that the superior endplate's concavity predisposes it to failure while the inferior endplate's flatter, more convex shape is protective (Section 2.4). Instead, failure patterns are likely dominated by other anatomical factors such as endplate thickness (Grant et al., 2001; Zhao et al., 2009), underlying trabecular bone strength (Holmes et al., 1993; Jackman et al., 2014), and size discrepancies, (Dudli et al., 2018) rather than curvatures.

### 5.3 The Effects of Joint Level on Endplate Deflection

While only the C3C4 and C4C5 joints showed statistically significant differences in endplate deflection, the variations observed across all joints warrant discussion. When averaged across all loading magnitudes and cycle counts, the mean difference in deflection between superior and inferior endplates was 46 μm at C3C4, 98 μm at C4C5, and 79 μm at C5C6. Although these differences may appear small, particularly given the discussion of "splitting hairs" in Section 5.1, the fact that they represent average differences across all loading conditions and cyclic exposures suggests a consistent overall trend in how adjacent joints differ in relative endplate behavior. In addition to intra-joint variations in endplate structure (Grant et al., 2001), interlevel differences in endplate thickness may also contribute to these findings. Zhao et al. (2009) reported that superior bony endplates become thicker toward lower lumbar levels, whereas inferior endplates remain relatively constant in thickness. This pattern could help explain why the C3C4 joint exhibited smaller differences in deflection than C4C5 and C5C6. At higher joint levels, the superior and

inferior endplates may be more similar in strength and stiffness than those located lower in the spine.

Wang et al. (2011) reported similar findings, noting that superior endplate thickness generally increases with descending spinal levels. Interestingly, they observed an exception at L5S1, where thickness decreased relative to L4L5 (Figure 5.3). This parallels the current study's findings, in which C5C6 exhibited a smaller difference in deflection between superior and inferior endplates than C4C5, suggesting reduced disparity in endplate strength at C5C6. However, an additional layer of complexity arises when considering variations in mineral density of the endplate's bony layer, with Wang et al. (2011) reporting the superior L3L4 endplate exhibiting the highest density among lumbar levels (Figure 5.3). Thus, although the superior L3L4 endplate may not be the thickest, its density likely contributes to its structural strength. Given the L3L4 and C4C5 joints are both most centrally located within their respective spinal sections, they may reflect similar structural principles. However, without formal literature identifying which porcine cervical vertebrae correspond most closely to human lumbar levels, pinpointing the exact cause of inter-joint differences remains challenging. Nevertheless, variations in endplate deflection across joint levels are rooted in biological differences between upper and lower spinal joints, likely involving endplate thickness and trabecular bone density.

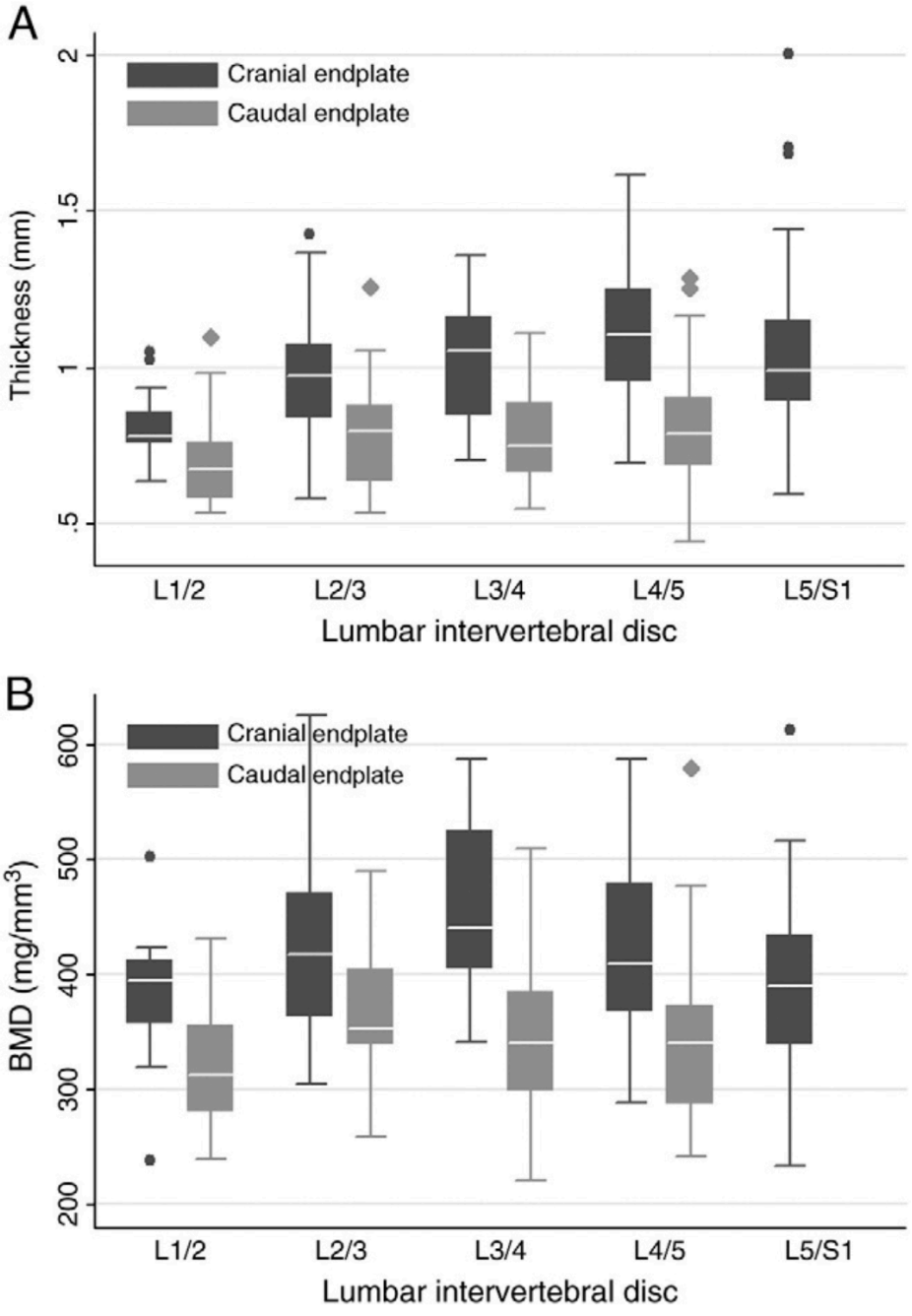



***Figure 5.3****: Superior and inferior endplate thicknesses and subchondral trabecular bone density.*

*Note, cranial and caudal are used interchangeably with this study's use of superior and inferior describing endplate levels with respect to the joint. Dots and diamonds represent outliers within the original data set. Adapted from Wang et al. 2011.*

### 5.4 The Limited Role of Nucleus-Endplate Contact Area

This study found that the proportion of nucleus area relative to the total endplate surface area was not a significant determinant of deflection. While this result may seem unsurprising given that all specimens were subjected to fixed stress targets, it warrants consideration of the vertebral endplate's heterogeneous structure. The endplate exhibits marked regional variation in thickness and strength, with the central region being the thinnest and weakest (Grant et al., 2001; Zhao et al., 2009). Accordingly, one might expect that a smaller nucleus area concentrated over these weaker central regions would result in greater deflection. In practice, however, even the smallest nucleus proportions likely extended into the stronger peripheral regions of the endplate. Moreover, the rigid indenter used in this study redirects force toward these stronger peripheral areas, reducing the influence of weaker central regions that would otherwise deflect more under load. As a result, although nucleus coverage varied substantially among specimens (40–70%), these differences were insufficient to meaningfully affect endplate deflection under the present experimental conditions.

A remaining question is whether larger nucleus–endplate contact areas influence deflection or injury risk in intact spinal joints. Theoretically, a larger contact area should reduce average stress, as the same load is distributed over a greater surface. However, *in-vivo* endplate deflection is often concentrated within small regions (Hulme et al., 2008; Jackman et al., 2014), and the endplate's nonuniform material properties likely limit the theoretical benefit of increased contact area. Although the hydrostatic pressure of the nucleus distributes relatively evenly, deformation and failure are primarily governed by the weakest local regions which typically include the central, thinner portions of the endplate (Zhao et al., 2009). Thus, even when overall endplate–nucleus contact area is larger, local deflection and failure are dictated by the spatial distribution of endplate

strength rather than global contact area. While the present study's methods do not permit direct observation of localized, point-source failures due to the rigid indenter, the lack of correlation between total deflection and nucleus area reinforces the idea that endplate deformation is driven by localized structural weakness.

### 5.5 Implications for the Validity of the Porcine Cervical Spine Model

As research using animal models to study the human lumbar spine grows in scale and complexity, the suitability of the porcine cervical spine as a surrogate warrants closer scrutiny. Significant uncertainties remain regarding how closely porcine and human vertebral endplates correspond, and what structural or mechanical consequences may result from any discrepancies. Although the outcomes of this study align with existing knowledge on endplate thickness (Wang et al., 2011; Zhao et al., 2009), strength (Grant et al., 2001), and subchondral bone properties (Hulme et al., 2008; Jackman et al., 2014), the observation that superior endplates deflect more than inferior ones and how this pattern mirrors that of the human lumbar spine represents a meaningful contribution. As the first known investigation to quantify endplate deflection in a cyclic loading context while also using the porcine model, this work provides further validation of the model's relevance for studying vertebral endplate behavior of humans.

However, as is typical with scientific pursuits, this work raises additional questions. Key determinants of endplate deflection such as endplate thickness and regional trabecular qualities remain poorly characterized in the porcine model, particularly in comparison to the human lumbar spine. Moreover, discrepancies persist in the types and locations of endplate injuries observed between species. In humans, failures are more frequently observed in inferior endplates (Fujiwara

et al., 2019; Ortiz & Bordia, 2011). In contrast, multiple studies using porcine cervical models have documented the opposite pattern under a range of loading conditions and experimental setups. For instance, Zehr et al. (2023) observed that fracture lesions developed only in the superior endplate of healthy porcine cervical vertebrae subjected to cyclic loading, contradicting the expectation that superior endplates are generally considered mechanically stronger. Similarly, Brown et al. (2008) found that experimentally increasing nucleus pressure produced a disproportionately greater incidence of injury in the superior joint endplate compared to the inferior one. Other studies also support this trend of the preferential superior endplate failure in porcine models across diverse loading contexts (Gooyers et al., 2015; Watson et al., 2024). Findings like these which challenge intuitive expectations underscore the need for further investigation into the structural and mechanical distinctions between porcine and human spinal models beyond superficial morphological features and gross load-bearing properties. As a result, these discrepancies raise important questions about the deeper validity of the porcine model in emulating human tissue.

### 5.6 Experimental Cost and Accessibility Considerations

An important aspect of scientific research is the effort to democratize access to both the information and tools necessary for experimentation. This study demonstrates the potential utility of a methodology constructed from readily available electronics and mechanical hardware. The custom-built setup, which included a profilometer, servomotor, ball screw linear rail, and 3D printer, had a total cost of roughly $2,500 CAD, making it far more accessible than micro-CT systems which typically cost hundreds of thousands of dollars. Traditional systems also incur

additional expenses for technician salaries, maintenance, and infrastructure, further raising the financial barrier to entry.

Admittedly, the reported cost of this apparatus does not include a full material testing system, which represents a substantial additional expense. The intent, however, is not to claim equivalence to enterprise-grade X-ray imaging systems, but to demonstrate that meaningful mechanical and structural data can be obtained using comparatively low-cost and modular components. In many research environments where basic testing infrastructure already exists, this approach could substantially reduce the marginal cost of experimentation. With further refinement, particularly through improved indenter technology as discussed in Section 5.8.1, this methodology could evolve into a highly affordable and adaptable platform for studying endplate mechanics. By lowering both financial and technical barriers, such systems could broaden participation in biomechanical research and enable exploratory studies that would otherwise remain confined to well-funded laboratories.

## 5.7 Orthopedic Applications

During total disc arthroplasties, both the intervertebral disc and cartilaginous endplates are completely excised and replaced with an artificial implant designed to restore height and preserve physiological motion between adjacent vertebrae (Salzmann et al., 2017; Sandhu et al., 2020). Long-term implant success is threatened by subsidence, the sinking or settling of the implant into the vertebral endplate, which occurs when contact between the implant and bony endplate is uneven or insufficient to distribute loads uniformly (Lee, 2007).

Previous studies of intact spinal joints show that the inferior endplate exhibits greater localized deflections, driven by point-source weaknesses exploited by the fluid nucleus (Grant et al., 2001;

Hulme et al., 2007; Jackman et al., 2014). By using a rigid indenter, this study also demonstrates that the inferior endplate tends to undergo more global deflection, with the entire nucleus-occupying region showing greater overall compliance than the superior endplate. For disc replacement implants interfacing with endplates via rigid metal plates, this global deflection is arguably more relevant than the localized deflections expected *in vivo*. These findings emphasize the need for implant manufacturers to account for the generally higher compliance of the inferior endplate, particularly at lower spinal levels, where this study observed the largest differences in endplate deflection.

## 5.8 Limitations

### 5.8.1 Consequences of a Rigid Indenter

The primary limitation of this study lies in the indenter design. It is unsurprising that a rigid plastic structure fails to replicate the fluid and surface conforming behaviour of the spinal joint's nucleus. Although this study's premise was partly based on the rationale that cyclic loading could help maintain fluid pressure more effectively than static loading protocols previously employed to measure endplate deflection, fluid loss still occurs under dynamic loading conditions (Gooyers & Callaghan, 2015; Gooyers et al., 2012). Consequently, the indenter fails to reproduce the effects of nucleus fluid loss, particularly under prolonged cyclic loading. This may lead to an over estimation of endplate deflection at higher cycle counts and loading magnitudes. Another limitation is in the rigidity of the indenter which enforces an even stress distribution. As localized weaknesses in the endplate begin to deform or fail, stress redistributes to stronger peripheral regions the indenter contacts. The resulting deflection measured in this study therefore reflects a global deformation pattern rather than a localized deflection that would otherwise occur in an intact spinal joint. While

the severity of these limitations stemming from the indenter's design is difficult to quantify, it is conceptually clear that this method does not perfectly model the injury mechanisms typical of endplate failure. This is supported by the absence of observable macroscopic damage after 5000 loading cycles using parameters typically sufficient to cause failure in an intact spinal joint (Zehr et al., 2020; Zehr, Watson, et al., 2023). Without insight into the microdamage occurring, it remains uncertain to what extent this study's loading protocol reflects true whole-joint conditions.

If more accurate deflection measurements are to be achieved, two hypothetical avenues can be considered. The first involves developing an indenter that better mimics the native nucleus by dynamically conforming to the endplate surface while maintaining a consistent stress distribution. One conceptual design draws inspiration from a pin art toy, where a field of independently moving pins record their relative displacements as the endplate surface they contact deforms under load. In this setup, greater displacement of individual pins could both indicate and measure the initiation of a localized deflection, more closely replicating the deformation and failure mechanisms that occur in the presence of the nucleus. More ideally, a micro-CT system capable of capturing a snapshot mid-loading cycle, without the need for prolonged scan times, would provide the most direct visualization of endplate deformation. Although both ideas remain theoretical, they illustrate interesting ideas about how future iterations of this work might one day be approached.

### 5.8.2 Errors in Measurement Corrections

Vertical compression of the system was subtracted out of the indenter's displacement by tracking a spherical marker attached to the anterior of the specimen. However, the profilometer system could not account for any tilting of the specimen during the loading process, which may have misrepresented the vertical displacement of the bearing. Although vertebral potting and

fastening strategies were implemented to minimize this effect (Section 3.3), small, visually imperceptible tilts may have occurred, representing a potential source of error in the corrected endplate deflection measurements.

Similarly, deformation of the indenter under load could not be feasibly accounted for either. Since each indenter differed in geometry and structural stiffness, mechanical testing to obtain an indenter-specific stress-strain curve would require creating a negative replica of each indenter to provide uniform contact and avoid unrepresentative stress concentrations and deformations. While this is theoretically possible, fabricating such replicas would be laborious and costly, necessitating CNC machining of a material significantly stiffer than the indenter, likely a metal. An alternative approach involved testing flat indenters with cross-sectional areas equivalent to the original ones they are based upon, but with a flat face contacting the material testing system bed. However, inevitable imperfections in surface mating and alignment between the flat indenter and testing surface alters the stress–strain response, particularly within the toe region where most forces in this study were applied. Even small deviations in this region could substantially affect the correction factors applied to measured deflections. Moreover, this approach neglects the effects of differing indenter geometries arising from the distinct curvatures of superior and inferior endplates. For these reasons, indenter deformation could not be corrected for in this study, likely resulting in small elastic deformations of the indenter contributing to the measured endplate deflections. However, as shown in Section 3.6, loads exceeding those applied in this study by 300% produced no measurable plastic deformation of the indenter. Therefore, although elastic deformations of the indenter contributed to deflection measurements, their effect is constant between measures of the same magnitude. This indicates that the observed increases in deflection with loading cycles reflect genuine changes in endplate deformation rather than artifacts from the indenter.

### 5.9 Sources of Curiosity and Future Avenues of Research

Given both the limited ability to explain the differences in endplate deflection across spinal joint heights (Section 5.2) and the assumption that human lumbar endplate thickness and vertebral bone mineral density are comparable to those of the porcine cervical spine, future work should examine how well these two structures truly align in these respects. Such data would help further validate the porcine cervical spine as an appropriate surrogate for the human lumbar spine and provide context for the between-joint differences observed in this study. Additionally, investigations into how the more exaggerated endplate curvatures of the porcine cervical spine influence loading behavior and failure patterns, relative to the human lumbar spine, may further clarify the differences in failure locations and types observed between the two models.

Another avenue for future work lies in examining how spinal joint height loss influences endplate mechanics. Reductions in joint height, whether from sustained loading (Gooyers et al., 2012) or degenerative processes, can cause endplates within a joint to contact one another in peripheral annular regions (Massey et al., 2012). Such contact shunts compressive stress away from the nucleus toward the periphery (van Dieën et al., 2001), thereby decreasing central endplate deflection. Developing an apparatus capable of selectively loading either the nucleus-containing region or including the peripheral annular regions would allow targeted investigation of the effects of the edge-loading scenarios. This could clarify how individuals with degenerative disc disorders might experience reduced deflection-related endplate injury risk due to increased peripheral support.

Lastly, because this study applied relatively low compressive forces compared to those typically required to produce whole joint failure, it would be valuable to compare this method's

endplate deflection measurements with micro-CT data obtained at higher loads approaching endplate failure. At these higher compressive forces, the signal-to-noise ratio would likely improve, making true differences between measurement methodologies more apparent. Conducting such a comparison would require developing an approach capable of continuously recording total vertebral compression during ramp-to-failure testing to maximize deflection measurement accuracy. This data could help clarify how the relative stiffness and compliance of the superior and inferior endplates change across load magnitudes, and at what points their respective deformation trajectories begin to converge or diverge.

# Chapter 6 – Conclusions

This study aimed to quantify and compare superior and inferior endplate deflection under cyclic loading using the porcine cervical spine as a surrogate for the human lumbar spine. Across all tested levels (C3C4, C4C5, and C5C6), the inferior endplate consistently exhibited greater deflection than the superior endplate. This finding aligns with previous studies of human lumbar joints that have reported similar within-joint differences under static loading conditions. Further, a significantly greater rate of accumulation in inferior endplate deflection was only observed in the first 1000 cycles of the C4C5 and C5C6 joints. As the first investigation of endplate deflection using the porcine cervical spine model, this work strengthens the evidence supporting its suitability for replicating human cadaveric endplate mechanics in this specific context.

A relationship between spinal level and the magnitude of discrepancy in endplate deflection was also demonstrated, with the C4C5 joint exhibiting the greatest difference between inferior and superior endplates, followed by C5C6 and C3C4. This trend suggests that variations in inferior–superior endplate compliance depend on spinal level, likely reflecting inter-joint anatomical and structural differences that influence susceptibility to injury. Additionally, this work found no relationship between the proportion of the nucleus-occupying region and endplate deflection, indicating that deflection behavior is likely governed more by localized structural weaknesses than by the relative area of nucleus occupation.

Lastly, this study developed a novel method using custom 3D-printable indenters that enabled the measure of endplate deflection patterns under cyclic loading. This approach builds on previous investigations that relied strictly on prolonged stepwise loading and micro-CT imaging, methods that can cause excess joint fluid loss and alter deflection measurements. In contrast, the present method is both non-destructive to the vertebral bone and yielded deflection measurements

similar to costly imaging systems. Given this experimental setup can be fabricated using readily available consumer hardware, it offers a financially accessible and practical alternative for assessing certain endplate mechanics. While this system by no means replaces CT-based imaging, it represents a successful proof of concept for a low-cost and novel endplate deflection measurement technique.

## References


Adams, M. A., McNally, D. S., & Dolan, P. (1996). 'Stress' distributions inside intervertebral discs. The effects of age and degeneration. *J Bone Joint Surg Br*, *78*(6), 965-972. https://doi.org/10.1302/0301-620x78b6.1287

Agur, A. M. R., & Dalley, A. F. (2017). *Grant's atlas of anatomy* (Edition 14. ed.). Wolters Kluwer.

Ahmed, M., Islam, M., Vanhoose, J., Hewavitharana, L., Stanich, A., & Hossain, M. (2016). *Comparisons of Bending Stiffness of 3D Printed Samples of Different Materials*. https://doi.org/10.1115/IMECE2016-65119

Aita, D., Milani, G., & Taliercio, A. (2024). Fast Limit Analysis of Domes Belonging to the Architectural Heritage Under Different Hypotheses on Masonry Strength. *International Journal of Architectural Heritage*, 1-33. https://doi.org/10.1080/15583058.2024.2412606

Arlot, M. E., Burt-Pichat, B., Roux, J. P., Vashishth, D., Bouxsein, M. L., & Delmas, P. D. (2008). Microarchitecture influences microdamage accumulation in human vertebral trabecular bone. *J Bone Miner Res*, *23*(10), 1613-1618. https://doi.org/10.1359/jbmr.080517

Ashinsky, B. G., Bonnevie, E. D., Mandalapu, S. A., Pickup, S., Wang, C., Han, L., Mauck, R. L., Smith, H. E., & Gullbrand, S. E. (2020). Intervertebral Disc Degeneration Is Associated With Aberrant Endplate Remodeling and Reduced Small Molecule Transport. *J Bone Miner Res*, *35*(8), 1572-1581. https://doi.org/10.1002/jbmr.4009

Bashkuev, M., Reitmaier, S., & Schmidt, H. (2020). Relationship between intervertebral disc and facet joint degeneration: A probabilistic finite element model study. *Journal of Biomechanics*, *102*, 109518. https://doi.org/https://doi.org/10.1016/j.jbiomech.2019.109518

Beach, T. A. C., Frost, D. M., Zehr, J. D., Howarth, S. J., McGill, S. M., & Callaghan, J. P. (2019). Spine loading during laboratory-simulated fireground operations - inter-individual variation and method of load quantification. *Ergonomics*, *62*(11), 1426-1438. https://doi.org/10.1080/00140139.2019.1657183

Berg-Johansen, B., Han, M., Fields, A. J., Liebenberg, E. C., Lim, B. J., Larson, P. E., Gunduz-Demir, C., Kazakia, G. J., Krug, R., & Lotz, J. C. (2018). Cartilage Endplate Thickness Variation Measured by Ultrashort Echo-Time MRI Is Associated With Adjacent Disc Degeneration. *Spine (Phila Pa 1976)*, *43*(10), E592-e600. https://doi.org/10.1097/brs.0000000000002432

Bernick, S., & Cailliet, R. (1982). Vertebral end-plate changes with aging of human vertebrae. *Spine (Phila Pa 1976)*, *7*(2), 97-102. https://doi.org/10.1097/00007632-198203000-00002

Bevill, G., Eswaran, S. K., Farahmand, F., & Keaveny, T. M. (2009). The influence of boundary conditions and loading mode on high-resolution finite element-computed trabecular tissue properties. *Bone*, *44*(4), 573-578. https://doi.org/10.1016/j.bone.2008.11.015

Biggemann, M., Hilweg, D., & Brinckmann, P. (1988). Prediction of the compressive strength of vertebral bodies of the lumbar spine by quantitative computed tomography. *Skeletal Radiology*, *17*(4), 264-269. https://doi.org/10.1007/BF00401809

Brinckmann, P., Frobin, W., Hierholzer, E., & Horst, M. (1983). Deformation of the vertebral end-plate under axial loading of the spine. *Spine (Phila Pa 1976)*, *8*(8), 851-856. https://doi.org/10.1097/00007632-198311000-00007

Brown, S. H., Gregory, D. E., & McGill, S. M. (2008). Vertebral end-plate fractures as a result of high rate pressure loading in the nucleus of the young adult porcine spine. *J Biomech*, *41*(1), 122-127. https://doi.org/10.1016/j.jbiomech.2007.07.005

Callaghan, J. P., & McGill, S. M. (1995). Frozen storage increases the ultimate compressive load of porcine vertebrae. *Journal of Orthopaedic Research*, *13*(5), 809-812. https://doi.org/https://doi.org/10.1002/jor.1100130522

Callaghan, J. P., & McGill, S. M. (2001). Low back joint loading and kinematics during standing and unsupported sitting. *Ergonomics*, *44*(3), 280-294. https://doi.org/10.1080/00140130118276

Cassidy, J. J., Hiltner, A., & Baer, E. (1989). Hierarchical structure of the intervertebral disc. *Connect Tissue Res*, *23*(1), 75-88. https://doi.org/10.3109/03008208909103905

Chang, C. W., Lai, P. H., Yip, C. M., & Hsu, S. S. (2009). Spontaneous regression of lumbar herniated disc. *J Chin Med Assoc*, *72*(12), 650-653. https://doi.org/10.1016/s1726-4901(09)70449-6

Chang, W. C., Christensen, T. M., Pinilla, T. P., & Keaveny, T. M. (1999). Uniaxial yield strains for bovine trabecular bone are isotropic and asymmetric. *J Orthop Res*, *17*(4), 582-585. https://doi.org/10.1002/jor.1100170418

Crump, K. B., Alminnawi, A., Bermudez-Lekerika, P., Compte, R., Gualdi, F., McSweeney, T., Muñoz-Moya, E., Nüesch, A., Geris, L., Dudli, S., Karppinen, J., Noailly, J., Le Maitre, C., & Gantenbein, B. (2023). Cartilaginous endplates: A comprehensive review on a neglected structure in intervertebral disc research. *JOR Spine*, *6*(4), e1294. https://doi.org/10.1002/jsp2.1294

DeLucca, J. F., Cortes, D. H., Jacobs, N. T., Vresilovic, E. J., Duncan, R. L., & Elliott, D. M. (2016). Human cartilage endplate permeability varies with degeneration and intervertebral disc site. *Journal of Biomechanics*, *49*(4), 550-557. https://doi.org/10.1016/j.jbiomech.2016.01.007

Dudli, S., Enns-Bray, W., Pauchard, Y., Römmeler, A., Fields, A. J., Ferguson, S. J., & Helgason, B. (2018). Larger vertebral endplate concavities cause higher failure load and work at failure under high-rate impact loading of rabbit spinal explants. *Journal of the Mechanical Behavior of Biomedical Materials*, *80*, 104-110. https://doi.org/https://doi.org/10.1016/j.jmbbm.2018.01.019

Eswaran, S. K., Gupta, A., Adams, M. F., & Keaveny, T. M. (2006). Cortical and trabecular load sharing in the human vertebral body. *J Bone Miner Res*, *21*(2), 307-314. https://doi.org/10.1359/jbmr.2006.21.2.307

Ferguson, S. J., & Steffen, T. (2003). Biomechanics of the aging spine. *Eur Spine J*, *12 Suppl 2*(Suppl 2), S97-s103. https://doi.org/10.1007/s00586-003-0621-0

Fields, A. J., Lee, G. L., & Keaveny, T. M. (2010). Mechanisms of initial endplate failure in the human vertebral body. *J Biomech*, *43*(16), 3126-3131. https://doi.org/10.1016/j.jbiomech.2010.08.002

Fields, A. J., Lee, G. L., Liu, X. S., Jekir, M. G., Guo, X. E., & Keaveny, T. M. (2011). Influence of vertical trabeculae on the compressive strength of the human vertebra. *J Bone Miner Res*, *26*(2), 263-269. https://doi.org/10.1002/jbmr.207

Fujiwara, A., Tamai, K., Yamato, M., An, H. S., Yoshida, H., Saotome, K., & Kurihashi, A. (1999). The relationship between facet joint osteoarthritis and disc degeneration of the lumbar spine: an MRI study. *Eur Spine J*, *8*(5), 396-401. https://doi.org/10.1007/s005860050193

Fujiwara, T., Akeda, K., Yamada, J., Kondo, T., & Sudo, A. (2019). Endplate and intervertebral disc injuries in acute and single level osteoporotic vertebral fractures: is there any association with the process of bone healing? *BMC Musculoskelet Disord*, *20*(1), 336. https://doi.org/10.1186/s12891-019-2719-5

Galante, J. O. (1967). Tensile properties of the human lumbar annulus fibrosus. *Acta Orthop Scand*, Suppl 100:101-191. https://doi.org/10.3109/ort.1967.38.suppl-100.01

Gao, G., Xu, F., Xu, J., & Liu, Z. (2022). Study of Material Color Influences on Mechanical Characteristics of Fused Deposition Modeling Parts. *Materials (Basel)*, *15*(19). https://doi.org/10.3390/ma15197039

Geneviève, L., Isabelle, L., Ségolène, P., Catherine, C., Charles El, R., & Gilles, G. (2016). Diversity in human hair growth, diameter, colour and shape. An in vivo study on young adults from 24 different ethnic groups observed in the five continents. *European Journal of Dermatology*, *26*(2), 144-154. https://doi.org/10.1684/ejd.2015.2726

Gooyers, C. E., Beach, T. A. C., Frost, D. M., Howarth, S. J., & Callaghan, J. P. (2018). Identifying interactive effects of task demands in lifting on estimates of in vivo low back joint loads. *Appl Ergon*, *67*, 203-210. https://doi.org/10.1016/j.apergo.2017.10.005

Gooyers, C. E., & Callaghan, J. P. (2015). Exploring interactions between force, repetition and posture on intervertebral disc height loss and bulging in isolated porcine cervical functional spinal units from sub-acute-failure magnitudes of cyclic compressive loading. *Journal of Biomechanics*, *48*(13), 3701-3708. https://doi.org/10.1016/j.jbiomech.2015.08.023

Gooyers, C. E., McMillan, E. M., Noguchi, M., Quadrilatero, J., & Callaghan, J. P. (2015). Characterizing the combined effects of force, repetition and posture on injury pathways and micro-structural damage in isolated functional spinal units from sub-acute-failure magnitudes of cyclic compressive loading. *Clin Biomech (Bristol, Avon)*, *30*(9), 953-959. https://doi.org/10.1016/j.clinbiomech.2015.07.003

Gooyers, C. E., McMillan, R. D., Howarth, S. J., & Callaghan, J. P. (2012). The impact of posture and prolonged cyclic compressive loading on vertebral joint mechanics. *Spine 37*(17), E1023-1029. https://doi.org/10.1097/BRS.0b013e318256f9e6

Granata, K. P., & Marras, W. S. (1995). An EMG-assisted model of trunk loading during free-dynamic lifting. *J Biomech*, *28*(11), 1309-1317. https://doi.org/10.1016/0021-9290(95)00003-z

Grant, J. P., Oxland, T. R., & Dvorak, M. F. (2001). Mapping the structural properties of the lumbosacral vertebral endplates. *Spine (Phila Pa 1976)*, *26*(8), 889-896. https://doi.org/10.1097/00007632-200104150-00012

Hansson, T. H., Keller, T. S., & Spengler, D. M. (1987). Mechanical behavior of the human lumbar spine. II. Fatigue strength during dynamic compressive loading. *J Orthop Res*, *5*(4), 479-487. https://doi.org/10.1002/jor.1100050403

Hart, N. H., Nimphius, S., Rantalainen, T., Ireland, A., Siafarikas, A., & Newton, R. U. (2017). Mechanical basis of bone strength: influence of bone material, bone structure and muscle action. *J Musculoskelet Neuronal Interact*, *17*(3), 114-139.

Hickman, T. T., Rathan-Kumar, S., & Peck, S. H. (2022). Development, Pathogenesis, and Regeneration of the Intervertebral Disc: Current and Future Insights Spanning Traditional to Omics Methods. *Front Cell Dev Biol*, *10*, 841831. https://doi.org/10.3389/fcell.2022.841831

Holmes, A. D., Hukins, D. W., & Freemont, A. J. (1993). End-plate displacement during compression of lumbar vertebra-disc-vertebra segments and the mechanism of failure. *Spine (Phila Pa 1976)*, *18*(1), 128-135. https://doi.org/10.1097/00007632-199301000-00019

Hulme, P. A., Boyd, S. K., & Ferguson, S. J. (2007). Regional variation in vertebral bone morphology and its contribution to vertebral fracture strength. *Bone*, *41*(6), 946-957. https://doi.org/10.1016/j.bone.2007.08.019

Hulme, P. A., Ferguson, S. J., & Boyd, S. K. (2008). Determination of vertebral endplate deformation under load using micro-computed tomography. *J Biomech*, *41*(1), 78-85. https://doi.org/10.1016/j.jbiomech.2007.07.018

Jackman, T. M., Hussein, A. I., Adams, A. M., Makhnejia, K. K., & Morgan, E. F. (2014). Endplate deflection is a defining feature of vertebral fracture and is associated with properties of the underlying trabecular bone. *J Orthop Res*, *32*(7), 880-886. https://doi.org/10.1002/jor.22620

Keyence. (2012). Ultra-High Speed In-line Profilometer: LJ-V7000 Series User's Manual *Version 2*.

Kishimoto, M., Akeda, K., Sudo, A., Espinoza Orías, A. A., & Inoue, N. (2016). In vivo measurement of vertebral endplate surface area along the whole-spine. *J Orthop Res*, *34*(8), 1418-1430. https://doi.org/10.1002/jor.23354

Lambers, F. M., Bouman, A. R., Rimnac, C. M., & Hernandez, C. J. (2013). Microdamage caused by fatigue loading in human cancellous bone: relationship to reductions in bone biomechanical performance. *PLOS ONE*, *8*(12), e83662. https://doi.org/10.1371/journal.pone.0083662

Lee, C. K. (2007). Osteopenia and total disc prosthesis subsidence: inclusion/exclusion criteria for total disc replacement. *Sas j*, *1*(2), 82-84. https://doi.org/10.1016/sasj-2007-0104-rr

Lee, K. K., & Teo, E. C. (2004). Poroelastic analysis of lumbar spinal stability in combined compression and anterior shear. *Journal of Spinal Disorders and Techniques*, *17*(5), 429-438. https://doi.org/10.1097/01.bsd.0000109835.59382.9c

MacLean, J. J., Owen, J. P., & Iatridis, J. C. (2007). Role of endplates in contributing to compression behaviors of motion segments and intervertebral discs. *J Biomech*, *40*(1), 55-63. https://doi.org/10.1016/j.jbiomech.2005.11.013

Massey, C. J., van Donkelaar, C. C., Vresilovic, E., Zavaliangos, A., & Marcolongo, M. (2012). Effects of aging and degeneration on the human intervertebral disc during the diurnal cycle: a finite element study. *J Orthop Res*, *30*(1), 122-128. https://doi.org/10.1002/jor.21475

Masuoka, K., Michalek, A. J., MacLean, J. J., Stokes, I. A., & Iatridis, J. C. (2007). Different effects of static versus cyclic compressive loading on rat intervertebral disc height and water loss in vitro. *Spine (Phila Pa 1976)*, *32*(18), 1974-1979. https://doi.org/10.1097/BRS.0b013e318133d591

McMillan, D. W., Garbutt, G., & Adams, M. A. (1996). Effect of sustained loading on the water content of intervertebral discs: implications for disc metabolism. *Ann Rheum Dis*, *55*(12), 880-887. https://doi.org/10.1136/ard.55.12.880

Mirzaali, M. J., Libonati, F., Böhm, C., Rinaudo, L., Cesana, B. M., Ulivieri, F. M., & Vergani, L. (2020). Fatigue-caused damage in trabecular bone from clinical, morphological and mechanical perspectives. *International Journal of Fatigue*, *133*, 105451. https://doi.org/https://doi.org/10.1016/j.ijfatigue.2019.105451

Mow, V. C., Holmes, M. H., & Lai, W. M. (1984). Fluid transport and mechanical properties of articular cartilage: a review. *Journal of Biomechanics*, *17*(5), 377-394. https://doi.org/10.1016/0021-9290(84)90031-9

Nachemson, A., Lewin, T., Maroudas, A., & Freeman, M. A. (1970). In vitro diffusion of dye through the end-plates and the annulus fibrosus of human lumbar inter-vertebral discs. *Acta Orthop Scand*, *41*(6), 589-607. https://doi.org/10.3109/17453677008991550

Nagaraja, S., Couse, T. L., & Guldberg, R. E. (2005). Trabecular bone microdamage and microstructural stresses under uniaxial compression. *Journal of Biomechanics*, *38*(4), 707-716. https://doi.org/https://doi.org/10.1016/j.jbiomech.2004.05.013

Niebur, G. L., Feldstein, M. J., Yuen, J. C., Chen, T. J., & Keaveny, T. M. (2000). High-resolution finite element models with tissue strength asymmetry accurately predict failure of trabecular bone. *J Biomech*, *33*(12), 1575-1583. https://doi.org/10.1016/s0021-9290(00)00149-4

NIOSH, N. I. f. O. S. a. H. (1991). Scientific Support Documentation for the Revised 1991 NIOSH Lifting Equation: Technical Contract Reports. 1–282.

Ortiz, A. O., & Bordia, R. (2011). Injury to the vertebral endplate-disk complex associated with osteoporotic vertebral compression fractures. *AJNR Am J Neuroradiol*, *32*(1), 115-120. https://doi.org/10.3174/ajnr.A2223

Osterhoff, G., Morgan, E. F., Shefelbine, S. J., Karim, L., McNamara, L. M., & Augat, P. (2016). Bone mechanical properties and changes with osteoporosis. *Injury*, *47 Suppl 2*(Suppl 2), S11-20. https://doi.org/10.1016/s0020-1383(16)47003-8

Palepu, V., Rayaprolu, S. D., & Nagaraja, S. (2019). Differences in Trabecular Bone, Cortical Shell, and Endplate Microstructure Across the Lumbar Spine. *Int J Spine Surg*, *13*(4), 361-370. https://doi.org/10.14444/6049

Parkinson, R. J., Durkin, J. L., & Callaghan, J. P. (2005). Estimating the compressive strength of the porcine cervical spine: an examination of the utility of DXA. *Spine*, *30*(17), E492-498. https://doi.org/10.1097/01.brs.0000176246.54774.54

Peng, X., Wang, Y., Guo, Z., & Shi, S. (2011). Numerical validation of a fiber-reinforced hyperelastic constitutive model for human intervertebral disc annulus fibrosus. *Journal of Mechanics in Medicine and Biology*, *11*(01), 163-176. https://doi.org/10.1142/s0219519410003691

Perey, O. (1957). Fracture of the vertebral end-plate in the lumbar spine; an experimental biochemical investigation. *Acta Orthop Scand Suppl*, *25*, 1-101. https://doi.org/10.3109/ort.1957.28.suppl-25.01

Roberts, S., McCall, I. W., Menage, J., Haddaway, M. J., & Eisenstein, S. M. (1997). Does the thickness of the vertebral subchondral bone reflect the composition of the intervertebral disc? *Eur Spine J*, *6*(6), 385-389. https://doi.org/10.1007/bf01834064

Roberts, S., Menage, J., & Urban, J. P. (1989). Biochemical and structural properties of the cartilage end-plate and its relation to the intervertebral disc. *Spine (Phila Pa 1976)*, *14*(2), 166-174. https://doi.org/10.1097/00007632-198902000-00005

Roberts, S., Urban, J. P., Evans, H., & Eisenstein, S. M. (1996). Transport properties of the human cartilage endplate in relation to its composition and calcification. *Spine (Phila Pa 1976)*, *21*(4), 415-420. https://doi.org/10.1097/00007632-199602150-00003

Rodriguez, A. G., Rodriguez-Soto, A. E., Burghardt, A. J., Berven, S., Majumdar, S., & Lotz, J. C. (2012). Morphology of the human vertebral endplate. *J Orthop Res*, *30*(2), 280-287. https://doi.org/10.1002/jor.21513

Salzmann, S. N., Plais, N., Shue, J., & Girardi, F. P. (2017). Lumbar disc replacement surgery-successes and obstacles to widespread adoption. *Curr Rev Musculoskelet Med*, *10*(2), 153-159. https://doi.org/10.1007/s12178-017-9397-4

Sampson, S. L., Sylvia, M., & Fields, A. J. (2019). Effects of dynamic loading on solute transport through the human cartilage endplate. *J Biomech*, *83*, 273-279. https://doi.org/10.1016/j.jbiomech.2018.12.004

Sandhu, F. A., Dowlati, E., & Garica, R. (2020). Lumbar Arthroplasty: Past, Present, and Future. *Neurosurgery*, *86*(2), 155-169. https://doi.org/10.1093/neuros/nyz439

Singh, B. J. (2009). Comparative Study of Human and Animal Hair in Relation with Diameter and Medullary Index.

Tsai, K. H., Lin, R. M., & Chang, G. L. (1998). Rate-related fatigue injury of vertebral disc under axial cyclic loading in a porcine body-disc-body unit. *Clin Biomech (Bristol)*, *13*(1 Suppl 1), S32-s39. https://doi.org/10.1016/s0268-0033(98)80134-4

Turner, C. H. (1989). Yield behavior of bovine cancellous bone. *J Biomech Eng*, *111*(3), 256-260. https://doi.org/10.1115/1.3168375

Twomey, L., & Taylor, J. (1982). Flexion creep deformation and hysteresis in the lumbar vertebral column. *Spine (Phila Pa 1976)*, *7*(2), 116-122. https://doi.org/10.1097/00007632-198203000-00005

van Dieën, J. H., Kingma, I., Meijer, R., Hänsel, L., & Huiskes, R. (2001). Stress distribution changes in bovine vertebrae just below the endplate after sustained loading. *Clin*

*Biomech (Bristol)*, *16 Suppl 1*, S135-142. https://doi.org/10.1016/s0268-0033(00)00105-4

Velnar, T., & Gradisnik, L. (2023). Endplate role in the degenerative disc disease: A brief review. *World J Clin Cases*, *11*(1), 17-29. https://doi.org/10.12998/wjcc.v11.i1.17

Wang, Y., Battié, M. C., Boyd, S. K., & Videman, T. (2011). The osseous endplates in lumbar vertebrae: thickness, bone mineral density and their associations with age and disk degeneration. *Bone*, *48*(4), 804-809. https://doi.org/10.1016/j.bone.2010.12.005

Wang, Y., Battié, M. C., & Videman, T. (2012). A morphological study of lumbar vertebral endplates: radiographic, visual and digital measurements. *European Spine Journal*, *21*(11), 2316-2323. https://doi.org/10.1007/s00586-012-2415-8

Watson, M. I., Zehr, J. D., & Callaghan, J. P. (2024). Experimentally Dissociating the Acute Mechanisms of Endplate Fracture Lesions and Schmorl's node Injuries Using a Porcine Cervical Spine Model. *Spine (Phila Pa 1976)*. https://doi.org/10.1097/brs.0000000000005026

Wenzel, T. E., Schaffler, M. B., & Fyhrie, D. P. (1996). In vivo trabecular microcracks in human vertebral bone. *Bone*, *19*(2), 89-95. https://doi.org/10.1016/8756-3282(96)88871-5

Wong, J., Sampson, S. L., Bell-Briones, H., Ouyang, A., Lazar, A. A., Lotz, J. C., & Fields, A. J. (2019). Nutrient supply and nucleus pulposus cell function: effects of the transport properties of the cartilage endplate and potential implications for intradiscal biologic therapy. *Osteoarthritis Cartilage*, *27*(6), 956-964. https://doi.org/10.1016/j.joca.2019.01.013

Wu, Y., Cisewski, S. E., Wegner, N., Zhao, S., Pellegrini, V. D., Jr., Slate, E. H., & Yao, H. (2016). Region and strain-dependent diffusivities of glucose and lactate in healthy human cartilage endplate. *J Biomech*, *49*(13), 2756-2762. https://doi.org/10.1016/j.jbiomech.2016.06.008

Xiang, P., Luo, Z. P., & Che, Y. J. (2024). Insights into the mechanical microenvironment within the cartilaginous endplate: An emerging role in maintaining disc homeostasis and normal function. *Heliyon*, *10*(10), e31162. https://doi.org/10.1016/j.heliyon.2024.e31162

Yingling, V. R., Callaghan, J. P., & McGill, S. M. (1997). Dynamic loading affects the mechanical properties and failure site of porcine spines. *Clinical Biomechanics*, *12*(5), 301-305. https://doi.org/10.1016/s0268-0033(97)00009-0

Yingling, V. R., Callaghan, J. P., & McGill, S. M. (1999). The porcine cervical spine as a model of the human lumbar spine: an anatomical, geometric, and functional comparison. *J Spinal Disord*, *12*(5), 415-423.

Zehr, J. D., Barrett, J. M., & Callaghan, J. P. (2022). Cyclic loading history alters the joint compression tolerance and regional indentation responses in the cartilaginous endplate. *J Mech Behav Biomed Mater*, *136*, 105542. https://doi.org/10.1016/j.jmbbm.2022.105542

Zehr, J. D., Buchman-Pearle, J. M., & Callaghan, J. P. (2020). Joint fatigue-failure: A demonstration of viscoelastic responses to rate and frequency loading parameters using the porcine cervical spine. *Journal of Biomechanics*, *113*, 110081. https://doi.org/10.1016/j.jbiomech.2020.110081

Zehr, J. D., Quadrilatero, J., & Callaghan, J. P. (2023). Incidence of Compression-Induced Microinjuries in the Cartilage Endplate of the Spine. *Spine*, *48*(9), E122-E129. https://doi.org/10.1097/brs.0000000000004521

Zehr, J. D., Quadrilatero, J., & Callaghan, J. P. (2024). Indentation mechanics and native collagen content in the cartilaginous endplate: A comparison between porcine cervical and human lumbar spines. *J Mech Behav Biomed Mater*, *150*, 106334. https://doi.org/10.1016/j.jmbbm.2023.106334

Zehr, J. D., Rahman, F. A., Callaghan, J. P., & Quadrilatero, J. (2022). Mechanically induced histochemical and structural damage in the annulus fibrosus and cartilaginous endplate: a multi-colour immunofluorescence analysis. *Cell and Tissue Research*, *390*(1), 59-70. https://doi.org/10.1007/s00441-022-03649-2

Zehr, J. D., Tennant, L. M., & Callaghan, J. P. (2019). Examining endplate fatigue failure during cyclic compression loading with variable and consistent peak magnitudes using a force weighting adjustment approach: an in vitro study. *Ergonomics*, *62*(10), 1339-1348. https://doi.org/10.1080/00140139.2019.1648879

Zehr, J. D., Watson, M. I., & Callaghan, J. P. (2023). Experimentally dissociating the overuse mechanisms of endplate fracture lesions and Schmorl's node injuries using the porcine cervical spine model. *Clinical Biomechanics*, *104*, 105946. https://doi.org/10.1016/j.clinbiomech.2023.105946

Zehra, U., Robson-Brown, K., Adams, M. A., & Dolan, P. (2015). Porosity and Thickness of the Vertebral Endplate Depend on Local Mechanical Loading. *Spine (Phila Pa 1976)*, *40*(15), 1173-1180. https://doi.org/10.1097/brs.0000000000000925

Zhao, F. D., Pollintine, P., Hole, B. D., Adams, M. A., & Dolan, P. (2009). Vertebral fractures usually affect the cranial endplate because it is thinner and supported by less-dense trabecular bone. *Bone*, *44*(2), 372-379. https://doi.org/https://doi.org/10.1016/j.bone.2008.10.048

# Appendices

***Table 8.1**: Outputs of linear mixed effects model comparing superior and inferior endplate deflection in the C3C4 joint.*

```
Fixed effects:
                                             Estimate Std. Error       df t value Pr(>|t|)
(Intercept)                                  -157.837     75.543    8.638  -2.089  0.06754 .
loading_magnitude1                             48.821     14.172  110.000   3.445  0.00081 ***
loading_magnitude3                            193.697     14.172  110.000  13.667  < 2e-16 ***
loading_cycles1000                             70.568     14.172  110.000   4.979 2.38e-06 ***
loading_cycles3000                             90.669     14.172  110.000   6.398 3.96e-09 ***
loading_cycles5000                            102.738     14.172  110.000   7.249 6.16e-11 ***
groupInfC4                                     -4.258     19.774   14.830  -0.215  0.83244
nucleus_proportion                            292.013    134.862    8.122   2.165  0.06177 .
loading_magnitude1:loading_cycles1000          -3.298     20.043  110.000  -0.165  0.86961
loading_magnitude3:loading_cycles1000         -24.451     20.043  110.000  -1.220  0.22509
loading_magnitude1:loading_cycles3000          -1.592     20.043  110.000  -0.079  0.93683
loading_magnitude3:loading_cycles3000         -24.916     20.043  110.000  -1.243  0.21645
loading_magnitude1:loading_cycles5000          -2.385     20.043  110.000  -0.119  0.90549
loading_magnitude3:loading_cycles5000         -25.983     20.043  110.000  -1.296  0.19756
loading_magnitude1:groupInfC4                  24.748     20.043  110.000   1.235  0.21955
loading_magnitude3:groupInfC4                  53.067     20.043  110.000   2.648  0.00929 **
loading_cycles1000:groupInfC4                  14.902     20.043  110.000   0.744  0.45875
loading_cycles3000:groupInfC4                  16.766     20.043  110.000   0.837  0.40468
loading_cycles5000:groupInfC4                  17.762     20.043  110.000   0.886  0.37743
loading_magnitude1:loading_cycles1000:groupInfC4 -15.794     28.344  110.000  -0.557  0.57850
loading_magnitude3:loading_cycles1000:groupInfC4 -22.441     28.344  110.000  -0.792  0.43022
loading_magnitude1:loading_cycles3000:groupInfC4  -7.170     28.344  110.000  -0.253  0.80076
loading_magnitude3:loading_cycles3000:groupInfC4 -24.849     28.344  110.000  -0.877  0.38257
loading_magnitude1:loading_cycles5000:groupInfC4 -16.895     28.344  110.000  -0.596  0.55237
loading_magnitude3:loading_cycles5000:groupInfC4 -26.210     28.344  110.000  -0.925  0.35715
---
Signif. codes:  0 ‘***’ 0.001 ‘**’ 0.01 ‘*’ 0.05 ‘.’ 0.1 ‘ ’ 1
```

***Table 8.2**: Pairwise comparisons between endplates of the C3C4 joint within each loading magnitude × cycle combination (Tukey-adjusted)*

```
loading_magnitude = 0.3, loading_cycles = 0:
 contrast      estimate   SE   df lower.CL upper.CL t.ratio p.value
 SupC3 - InfC4     4.26 19.8 14.5    -38.1    46.63   0.215  0.8329

loading_magnitude = 1, loading_cycles = 0:
 contrast      estimate   SE   df lower.CL upper.CL t.ratio p.value
 SupC3 - InfC4   -20.49 19.8 14.5    -62.9    21.89  -1.034  0.3182

loading_magnitude = 3, loading_cycles = 0:
 contrast      estimate   SE   df lower.CL upper.CL t.ratio p.value
 SupC3 - InfC4   -48.81 19.8 14.5    -91.2    -6.43  -2.463  0.0269

loading_magnitude = 0.3, loading_cycles = 1000:
 contrast      estimate   SE   df lower.CL upper.CL t.ratio p.value
 SupC3 - InfC4   -10.64 19.8 14.5    -53.0    31.73  -0.537  0.5994

loading_magnitude = 1, loading_cycles = 1000:
 contrast      estimate   SE   df lower.CL upper.CL t.ratio p.value
 SupC3 - InfC4   -19.60 19.8 14.5    -62.0    22.78  -0.989  0.3390

loading_magnitude = 3, loading_cycles = 1000:
 contrast      estimate   SE   df lower.CL upper.CL t.ratio p.value
 SupC3 - InfC4   -41.27 19.8 14.5    -83.6     1.11  -2.082  0.0555

loading_magnitude = 0.3, loading_cycles = 3000:
 contrast      estimate   SE   df lower.CL upper.CL t.ratio p.value
 SupC3 - InfC4   -12.51 19.8 14.5    -54.9    29.87  -0.631  0.5378

loading_magnitude = 1, loading_cycles = 3000:
 contrast      estimate   SE   df lower.CL upper.CL t.ratio p.value
 SupC3 - InfC4   -30.09 19.8 14.5    -72.5    12.29  -1.518  0.1505

loading_magnitude = 3, loading_cycles = 3000:
 contrast      estimate   SE   df lower.CL upper.CL t.ratio p.value
 SupC3 - InfC4   -40.73 19.8 14.5    -83.1     1.65  -2.055  0.0584

loading_magnitude = 0.3, loading_cycles = 5000:
 contrast      estimate   SE   df lower.CL upper.CL t.ratio p.value
 SupC3 - InfC4   -13.50 19.8 14.5    -55.9    28.87  -0.681  0.5064

loading_magnitude = 1, loading_cycles = 5000:
 contrast      estimate   SE   df lower.CL upper.CL t.ratio p.value
 SupC3 - InfC4   -21.36 19.8 14.5    -63.7    21.02  -1.078  0.2988

loading_magnitude = 3, loading_cycles = 5000:
 contrast      estimate   SE   df lower.CL upper.CL t.ratio p.value
 SupC3 - InfC4   -40.36 19.8 14.5    -82.7     2.01  -2.037  0.0604

Degrees-of-freedom method: kenward-roger
Confidence level used: 0.95
```

***Table 8.3**: Pairwise comparisons of changes in deflection between superior C3 and inferior C4 endplates across loading magnitudes and consecutive cycle intervals (Tukey-adjusted).*

```
loading_magnitude = 0.3, contrast = 0→1000:
 contrast1     estimate SE  df t.ratio p.value
 SupC3 - InfC4  -14.902 20 110  -0.744  0.4588

loading_magnitude = 1, contrast = 0→1000:
 contrast1     estimate SE  df t.ratio p.value
 SupC3 - InfC4    0.892 20 110   0.045  0.9646

loading_magnitude = 3, contrast = 0→1000:
 contrast1     estimate SE  df t.ratio p.value
 SupC3 - InfC4    7.539 20 110   0.376  0.7075

loading_magnitude = 0.3, contrast = 1000→3000:
 contrast1     estimate SE  df t.ratio p.value
 SupC3 - InfC4   -1.864 20 110  -0.093  0.9261

loading_magnitude = 1, contrast = 1000→3000:
 contrast1     estimate SE  df t.ratio p.value
 SupC3 - InfC4  -10.488 20 110  -0.523  0.6018

loading_magnitude = 3, contrast = 1000→3000:
 contrast1     estimate SE  df t.ratio p.value
 SupC3 - InfC4    0.544 20 110   0.027  0.9784

loading_magnitude = 0.3, contrast = 3000→5000:
 contrast1     estimate SE  df t.ratio p.value
 SupC3 - InfC4   -0.996 20 110  -0.050  0.9604

loading_magnitude = 1, contrast = 3000→5000:
 contrast1     estimate SE  df t.ratio p.value
 SupC3 - InfC4    8.728 20 110   0.435  0.6641

loading_magnitude = 3, contrast = 3000→5000:
 contrast1     estimate SE  df t.ratio p.value
 SupC3 - InfC4    0.364 20 110   0.018  0.9855
```

***Table 8.4**: Outputs of linear mixed effects model comparing superior and inferior endplate deflection in the C4C5 joint.*

```
Fixed effects:
                                             Estimate Std. Error       df t value Pr(>|t|)
(Intercept)                                   34.7338    59.4459   6.6201   0.584 0.578380
loading_magnitude1                            47.0361     9.1065 110.0001   5.165 1.08e-06 ***
loading_magnitude3                           169.9241     9.1065 110.0001  18.660  < 2e-16 ***
loading_cycles1000                            46.1788     9.1065 110.0001   5.071 1.62e-06 ***
loading_cycles3000                            60.1954     9.1065 110.0001   6.610 1.43e-09 ***
loading_cycles5000                            65.7308     9.1065 110.0001   7.218 7.20e-11 ***
groupInfC5                                     0.6605    18.1983   8.0818   0.036 0.971927
nucleus_proportion                           -62.9735   104.7171   6.3801  -0.601 0.568334
loading_magnitude1:loading_cycles1000         -1.0230    12.8786 110.0001  -0.079 0.936831
loading_magnitude3:loading_cycles1000        -14.6058    12.8786 110.0001  -1.134 0.259212
loading_magnitude1:loading_cycles3000         -1.9185    12.8786 110.0001  -0.149 0.881852
loading_magnitude3:loading_cycles3000        -17.1080    12.8786 110.0001  -1.328 0.186792
loading_magnitude1:loading_cycles5000         -0.8939    12.8786 110.0001  -0.069 0.944790
loading_magnitude3:loading_cycles5000        -12.8501    12.8786 110.0001  -0.998 0.320569
loading_magnitude1:groupInfC5                 32.3936    12.8786 110.0001   2.515 0.013338 *
loading_magnitude3:groupInfC5                105.4767    12.8786 110.0001   8.190 5.16e-13 ***
loading_cycles1000:groupInfC5                 84.0885    12.8786 110.0001   6.529 2.11e-09 ***
loading_cycles3000:groupInfC5                 97.7405    12.8786 110.0001   7.589 1.11e-11 ***
loading_cycles5000:groupInfC5                104.1357    12.8786 110.0001   8.086 8.82e-13 ***
loading_magnitude1:loading_cycles1000:groupInfC5 -20.3399    18.2130 110.0001  -1.117 0.266523
loading_magnitude3:loading_cycles1000:groupInfC5 -57.2734    18.2130 110.0001  -3.145 0.002139 **
loading_magnitude1:loading_cycles3000:groupInfC5 -20.5599    18.2130 110.0001  -1.129 0.261413
loading_magnitude3:loading_cycles3000:groupInfC5 -62.2143    18.2130 110.0001  -3.416 0.000892 ***
loading_magnitude1:loading_cycles5000:groupInfC5 -20.6682    18.2130 110.0001  -1.135 0.258925
loading_magnitude3:loading_cycles5000:groupInfC5 -66.0148    18.2130 110.0001  -3.625 0.000440 ***
---
Signif. codes:  0 ‘***’ 0.001 ‘**’ 0.01 ‘*’ 0.05 ‘.’ 0.1 ‘ ’ 1
```

***Table 8.5**: Pairwise comparisons between endplates of the C4C5 joint within each loading magnitude × cycle combination (Tukey-adjusted)*

```
loading_magnitude = 0.3, loading_cycles = 0:
 contrast      estimate   SE  df lower.CL upper.CL t.ratio p.value
 SupC4 - InfC5   -0.661 18.2 7.8    -42.8    41.52  -0.036  0.9720

loading_magnitude = 1, loading_cycles = 0:
 contrast      estimate   SE  df lower.CL upper.CL t.ratio p.value
 SupC4 - InfC5  -33.054 18.2 7.8    -75.2     9.12  -1.815  0.1080

loading_magnitude = 3, loading_cycles = 0:
 contrast      estimate   SE  df lower.CL upper.CL t.ratio p.value
 SupC4 - InfC5 -106.137 18.2 7.8   -148.3   -63.96  -5.829  0.0004

loading_magnitude = 0.3, loading_cycles = 1000:
 contrast      estimate   SE  df lower.CL upper.CL t.ratio p.value
 SupC4 - InfC5  -84.749 18.2 7.8   -126.9   -42.57  -4.654  0.0017

loading_magnitude = 1, loading_cycles = 1000:
 contrast      estimate   SE  df lower.CL upper.CL t.ratio p.value
 SupC4 - InfC5  -96.803 18.2 7.8   -139.0   -54.63  -5.316  0.0008

loading_magnitude = 3, loading_cycles = 1000:
 contrast      estimate   SE  df lower.CL upper.CL t.ratio p.value
 SupC4 - InfC5 -132.952 18.2 7.8   -175.1   -90.78  -7.301  0.0001

loading_magnitude = 0.3, loading_cycles = 3000:
 contrast      estimate   SE  df lower.CL upper.CL t.ratio p.value
 SupC4 - InfC5  -98.401 18.2 7.8   -140.6   -56.23  -5.404  0.0007

loading_magnitude = 1, loading_cycles = 3000:
 contrast      estimate   SE  df lower.CL upper.CL t.ratio p.value
 SupC4 - InfC5 -110.235 18.2 7.8   -152.4   -68.06  -6.054  0.0003

loading_magnitude = 3, loading_cycles = 3000:
 contrast      estimate   SE  df lower.CL upper.CL t.ratio p.value
 SupC4 - InfC5 -141.663 18.2 7.8   -183.8   -99.49  -7.780  0.0001

loading_magnitude = 0.3, loading_cycles = 5000:
 contrast      estimate   SE  df lower.CL upper.CL t.ratio p.value
 SupC4 - InfC5 -104.796 18.2 7.8   -147.0   -62.62  -5.755  0.0005

loading_magnitude = 1, loading_cycles = 5000:
 contrast      estimate   SE  df lower.CL upper.CL t.ratio p.value
 SupC4 - InfC5 -116.522 18.2 7.8   -158.7   -74.35  -6.399  0.0002

loading_magnitude = 3, loading_cycles = 5000:
 contrast      estimate   SE  df lower.CL upper.CL t.ratio p.value
 SupC4 - InfC5 -144.258 18.2 7.8   -186.4  -102.08  -7.922  0.0001

Degrees-of-freedom method: kenward-roger
Confidence level used: 0.95
```

***Table 8.6**: Pairwise comparisons of changes in deflection between superior C4 and inferior C5 endplates across loading magnitudes and consecutive cycle intervals (Tukey-adjusted).*

```
loading_magnitude = 0.3, contrast = 0→1000:
 contrast1     estimate   SE  df t.ratio p.value
 SupC5 - InfC6   -84.09 12.9 110  -6.529  <.0001

loading_magnitude = 1, contrast = 0→1000:
 contrast1     estimate   SE  df t.ratio p.value
 SupC5 - InfC6   -63.75 12.9 110  -4.950  <.0001

loading_magnitude = 3, contrast = 0→1000:
 contrast1     estimate   SE  df t.ratio p.value
 SupC5 - InfC6   -26.82 12.9 110  -2.082  0.0396

loading_magnitude = 0.3, contrast = 1000→3000:
 contrast1     estimate   SE  df t.ratio p.value
 SupC5 - InfC6   -13.65 12.9 110  -1.060  0.2914

loading_magnitude = 1, contrast = 1000→3000:
 contrast1     estimate   SE  df t.ratio p.value
 SupC5 - InfC6   -13.43 12.9 110  -1.043  0.2992

loading_magnitude = 3, contrast = 1000→3000:
 contrast1     estimate   SE  df t.ratio p.value
 SupC5 - InfC6    -8.71 12.9 110  -0.676  0.5002

loading_magnitude = 0.3, contrast = 3000→5000:
 contrast1     estimate   SE  df t.ratio p.value
 SupC5 - InfC6    -6.40 12.9 110  -0.497  0.6205

loading_magnitude = 1, contrast = 3000→5000:
 contrast1     estimate   SE  df t.ratio p.value
 SupC5 - InfC6    -6.29 12.9 110  -0.488  0.6264

loading_magnitude = 3, contrast = 3000→5000:
 contrast1     estimate   SE  df t.ratio p.value
 SupC5 - InfC6    -2.59 12.9 110  -0.201  0.8407
```

***Table 8.7**: Outputs of linear mixed effects model comparing superior and inferior endplate deflection in the C5C6 joint.*

```
Fixed effects:
                                                Estimate Std. Error       df t value Pr(>|t|)
(Intercept)                                       82.475     95.106    7.048   0.867 0.414384
loading_magnitude1                                57.849      8.577  110.000   6.745 7.42e-10 ***
loading_magnitude3                               204.785      8.577  110.000  23.877  < 2e-16 ***
loading_cycles1000                                64.164      8.577  110.000   7.481 1.92e-11 ***
loading_cycles3000                                75.468      8.577  110.000   8.799 2.18e-14 ***
loading_cycles5000                                82.956      8.577  110.000   9.673  < 2e-16 ***
groupInfC6                                         6.509     16.287    8.786   0.400 0.698986
nucleus_proportion                              -149.475    171.033    6.939  -0.874 0.411365
loading_magnitude1:loading_cycles1000             -9.822     12.129  110.000  -0.810 0.419812
loading_magnitude3:loading_cycles1000            -41.303     12.129  110.000  -3.405 0.000923 ***
loading_magnitude1:loading_cycles3000            -10.491     12.129  110.000  -0.865 0.388945
loading_magnitude3:loading_cycles3000            -43.563     12.129  110.000  -3.592 0.000493 ***
loading_magnitude1:loading_cycles5000            -13.195     12.129  110.000  -1.088 0.279031
loading_magnitude3:loading_cycles5000            -45.370     12.129  110.000  -3.741 0.000293 ***
loading_magnitude1:groupInfC6                     31.974     12.129  110.000   2.636 0.009597 **
loading_magnitude3:groupInfC6                     89.543     12.129  110.000   7.383 3.16e-11 ***
loading_cycles1000:groupInfC6                     56.618     12.129  110.000   4.668 8.64e-06 ***
loading_cycles3000:groupInfC6                     63.884     12.129  110.000   5.267 6.95e-07 ***
loading_cycles5000:groupInfC6                     67.366     12.129  110.000   5.554 1.96e-07 ***
loading_magnitude1:loading_cycles1000:groupInfC6 -16.436     17.153  110.000  -0.958 0.340068
loading_magnitude3:loading_cycles1000:groupInfC6 -40.538     17.153  110.000  -2.363 0.019867 *
loading_magnitude1:loading_cycles3000:groupInfC6 -18.267     17.153  110.000  -1.065 0.289221
loading_magnitude3:loading_cycles3000:groupInfC6 -43.929     17.153  110.000  -2.561 0.011791 *
loading_magnitude1:loading_cycles5000:groupInfC6 -17.925     17.153  110.000  -1.045 0.298322
loading_magnitude3:loading_cycles5000:groupInfC6 -44.534     17.153  110.000  -2.596 0.010710 *
---
Signif. codes:  0 ‘***’ 0.001 ‘**’ 0.01 ‘*’ 0.05 ‘.’ 0.1 ‘ ’ 1
```

***Table 8.8**: Pairwise comparisons between endplates of the C5C6 joint within each loading magnitude × cycle combination (Tukey-adjusted)*

```
loading_magnitude = 0.3, loading_cycles = 0:
 contrast      estimate   SE   df lower.CL upper.CL t.ratio p.value
 SupC5 - InfC6    -6.51 16.9 8.43    -45.2   32.135  -0.385  0.7098

loading_magnitude = 1, loading_cycles = 0:
 contrast      estimate   SE   df lower.CL upper.CL t.ratio p.value
 SupC5 - InfC6   -38.48 16.9 8.43    -77.1    0.161  -2.276  0.0508

loading_magnitude = 3, loading_cycles = 0:
 contrast      estimate   SE   df lower.CL upper.CL t.ratio p.value
 SupC5 - InfC6   -96.05 16.9 8.43   -134.7  -57.408  -5.682  0.0004

loading_magnitude = 0.3, loading_cycles = 1000:
 contrast      estimate   SE   df lower.CL upper.CL t.ratio p.value
 SupC5 - InfC6   -63.13 16.9 8.43   -101.8  -24.483  -3.734  0.0052

loading_magnitude = 1, loading_cycles = 1000:
 contrast      estimate   SE   df lower.CL upper.CL t.ratio p.value
 SupC5 - InfC6   -78.66 16.9 8.43   -117.3  -40.021  -4.653  0.0014

loading_magnitude = 3, loading_cycles = 1000:
 contrast      estimate   SE   df lower.CL upper.CL t.ratio p.value
 SupC5 - InfC6  -112.13 16.9 8.43   -150.8  -73.488  -6.633  0.0001

loading_magnitude = 0.3, loading_cycles = 3000:
 contrast      estimate   SE   df lower.CL upper.CL t.ratio p.value
 SupC5 - InfC6   -70.39 16.9 8.43   -109.0  -31.749  -4.164  0.0028

loading_magnitude = 1, loading_cycles = 3000:
 contrast      estimate   SE   df lower.CL upper.CL t.ratio p.value
 SupC5 - InfC6   -84.10 16.9 8.43   -122.7  -45.455  -4.975  0.0009

loading_magnitude = 3, loading_cycles = 3000:
 contrast      estimate   SE   df lower.CL upper.CL t.ratio p.value
 SupC5 - InfC6  -116.01 16.9 8.43   -154.6  -77.363  -6.862  0.0001

loading_magnitude = 0.3, loading_cycles = 5000:
 contrast      estimate   SE   df lower.CL upper.CL t.ratio p.value
 SupC5 - InfC6   -73.88 16.9 8.43   -112.5  -35.232  -4.370  0.0021

loading_magnitude = 1, loading_cycles = 5000:
 contrast      estimate   SE   df lower.CL upper.CL t.ratio p.value
 SupC5 - InfC6   -87.92 16.9 8.43   -126.6  -49.281  -5.201  0.0007

loading_magnitude = 3, loading_cycles = 5000:
 contrast      estimate   SE   df lower.CL upper.CL t.ratio p.value
 SupC5 - InfC6  -118.88 16.9 8.43   -157.5  -80.240  -7.032  0.0001

Degrees-of-freedom method: kenward-roger
Confidence level used: 0.95
```

***Table 8.9**: Pairwise comparisons of changes in deflection between superior C5 and inferior C6 endplates across loading magnitudes and consecutive cycle intervals (Tukey-adjusted).*

```
loading_magnitude = 0.3, contrast = 0→1000:
 contrast1     estimate   SE  df t.ratio p.value
 SupC5 - InfC6   -56.62 12.1 110  -4.668  <.0001

loading_magnitude = 1, contrast = 0→1000:
 contrast1     estimate   SE  df t.ratio p.value
 SupC5 - InfC6   -40.18 12.1 110  -3.313  0.0013

loading_magnitude = 3, contrast = 0→1000:
 contrast1     estimate   SE  df t.ratio p.value
 SupC5 - InfC6   -16.08 12.1 110  -1.326  0.1877

loading_magnitude = 0.3, contrast = 1000→3000:
 contrast1     estimate   SE  df t.ratio p.value
 SupC5 - InfC6    -7.27 12.1 110  -0.599  0.5504

loading_magnitude = 1, contrast = 1000→3000:
 contrast1     estimate   SE  df t.ratio p.value
 SupC5 - InfC6    -5.43 12.1 110  -0.448  0.6550

loading_magnitude = 3, contrast = 1000→3000:
 contrast1     estimate   SE  df t.ratio p.value
 SupC5 - InfC6    -3.88 12.1 110  -0.319  0.7500

loading_magnitude = 0.3, contrast = 3000→5000:
 contrast1     estimate   SE  df t.ratio p.value
 SupC5 - InfC6    -3.48 12.1 110  -0.287  0.7746

loading_magnitude = 1, contrast = 3000→5000:
 contrast1     estimate   SE  df t.ratio p.value
 SupC5 - InfC6    -3.83 12.1 110  -0.315  0.7531

loading_magnitude = 3, contrast = 3000→5000:
 contrast1     estimate   SE  df t.ratio p.value
 SupC5 - InfC6    -2.88 12.1 110  -0.237  0.8129
```

***Table 8.10**: Outputs of linear mixed effects model comparing magnitude of differences between endplate of C3C4, C4C5, and C5C6 joints*

```
Fixed effects:
                                                         Estimate Std. Error         df t value Pr(>|t|)
(Intercept)                                             2.054e-12  1.837e+01  2.436e+01   0.000 1.000000
joint_levelC4C5                                        -2.720e-12  2.598e+01  2.436e+01   0.000 1.000000
joint_levelC5C6                                        -7.378e-13  2.598e+01  2.436e+01   0.000 1.000000
loading_magnitude1                                      2.475e+01  1.267e+01  1.650e+02   1.953 0.052547 .
loading_magnitude3                                      5.307e+01  1.267e+01  1.650e+02   4.187 4.59e-05 ***
loading_cycles1000                                      1.490e+01  1.267e+01  1.650e+02   1.176 0.241360
loading_cycles3000                                      1.677e+01  1.267e+01  1.650e+02   1.323 0.187706
loading_cycles5000                                      1.776e+01  1.267e+01  1.650e+02   1.401 0.162944
joint_levelC4C5:loading_magnitude1                      7.646e+00  1.792e+01  1.650e+02   0.427 0.670247
joint_levelC5C6:loading_magnitude1                      7.226e+00  1.792e+01  1.650e+02   0.403 0.687361
joint_levelC4C5:loading_magnitude3                      5.241e+01  1.792e+01  1.650e+02   2.924 0.003940 **
joint_levelC5C6:loading_magnitude3                      3.648e+01  1.792e+01  1.650e+02   2.035 0.043440 *
joint_levelC4C5:loading_cycles1000                      6.919e+01  1.792e+01  1.650e+02   3.860 0.000162 ***
joint_levelC5C6:loading_cycles1000                      4.172e+01  1.792e+01  1.650e+02   2.327 0.021155 *
joint_levelC4C5:loading_cycles3000                      8.097e+01  1.792e+01  1.650e+02   4.518 1.19e-05 ***
joint_levelC5C6:loading_cycles3000                      4.712e+01  1.792e+01  1.650e+02   2.629 0.009376 **
joint_levelC4C5:loading_cycles5000                      8.637e+01  1.792e+01  1.650e+02   4.819 3.25e-06 ***
joint_levelC5C6:loading_cycles5000                      4.960e+01  1.792e+01  1.650e+02   2.768 0.006293 **
loading_magnitude1:loading_cycles1000                  -1.579e+01  1.792e+01  1.650e+02  -0.881 0.379481
loading_magnitude3:loading_cycles1000                  -2.244e+01  1.792e+01  1.650e+02  -1.252 0.212320
loading_magnitude1:loading_cycles3000                  -7.170e+00  1.792e+01  1.650e+02  -0.400 0.689634
loading_magnitude3:loading_cycles3000                  -2.485e+01  1.792e+01  1.650e+02  -1.386 0.167493
loading_magnitude1:loading_cycles5000                  -1.689e+01  1.792e+01  1.650e+02  -0.943 0.347260
loading_magnitude3:loading_cycles5000                  -2.621e+01  1.792e+01  1.650e+02  -1.462 0.145555
joint_levelC4C5:loading_magnitude1:loading_cycles1000 -4.546e+00  2.535e+01  1.650e+02  -0.179 0.857899
joint_levelC5C6:loading_magnitude1:loading_cycles1000 -6.415e-01  2.535e+01  1.650e+02  -0.025 0.979840
joint_levelC4C5:loading_magnitude3:loading_cycles1000 -3.483e+01  2.535e+01  1.650e+02  -1.374 0.171245
joint_levelC5C6:loading_magnitude3:loading_cycles1000 -1.810e+01  2.535e+01  1.650e+02  -0.714 0.476259
joint_levelC4C5:loading_magnitude1:loading_cycles3000 -1.339e+01  2.535e+01  1.650e+02  -0.528 0.598039
joint_levelC5C6:loading_magnitude1:loading_cycles3000 -1.110e+01  2.535e+01  1.650e+02  -0.438 0.662102
joint_levelC4C5:loading_magnitude3:loading_cycles3000 -3.737e+01  2.535e+01  1.650e+02  -1.474 0.142353
joint_levelC5C6:loading_magnitude3:loading_cycles3000 -1.908e+01  2.535e+01  1.650e+02  -0.753 0.452676
joint_levelC4C5:loading_magnitude1:loading_cycles5000 -3.774e+00  2.535e+01  1.650e+02  -0.149 0.881835
joint_levelC5C6:loading_magnitude1:loading_cycles5000 -1.030e+00  2.535e+01  1.650e+02  -0.041 0.967637
joint_levelC4C5:loading_magnitude3:loading_cycles5000 -3.981e+01  2.535e+01  1.650e+02  -1.570 0.118242
joint_levelC5C6:loading_magnitude3:loading_cycles5000 -1.832e+01  2.535e+01  1.650e+02  -0.723 0.470738
---
Signif. codes:  0 ‘***’ 0.001 ‘**’ 0.01 ‘*’ 0.05 ‘.’ 0.1 ‘ ’ 1
```

***Table 8.11**: Pairwise comparisons of endplate deflection between joints for each magnitude × cycle combination (Tukey-adjusted)*

```
loading_magnitude = 0.3, loading_cycles = 0:
 contrast    estimate   SE   df t.ratio p.value
 C3C4 - C4C5     0.00 26.7 24.4   0.000  1.0000
 C3C4 - C5C6     0.00 27.4 11.8   0.000  1.0000
 C4C5 - C5C6     0.00 26.7 24.4   0.000  1.0000

loading_magnitude = 1, loading_cycles = 0:
 contrast    estimate   SE   df t.ratio p.value
 C3C4 - C4C5    -7.65 26.7 24.4  -0.286  0.9559
 C3C4 - C5C6    -7.23 27.4 11.8  -0.264  0.9625
 C4C5 - C5C6     0.42 26.7 24.4   0.016  0.9999

loading_magnitude = 3, loading_cycles = 0:
 contrast    estimate   SE   df t.ratio p.value
 C3C4 - C4C5   -52.41 26.7 24.4  -1.963  0.1429
 C3C4 - C5C6   -36.48 27.4 11.8  -1.332  0.4060
 C4C5 - C5C6    15.93 26.7 24.4   0.597  0.8231

loading_magnitude = 0.3, loading_cycles = 1000:
 contrast    estimate   SE   df t.ratio p.value
 C3C4 - C4C5   -69.19 26.7 24.4  -2.592  0.0407
 C3C4 - C5C6   -41.72 27.4 11.8  -1.523  0.3159
 C4C5 - C5C6    27.47 26.7 24.4   1.029  0.5661

loading_magnitude = 1, loading_cycles = 1000:
 contrast    estimate   SE   df t.ratio p.value
 C3C4 - C4C5   -72.29 26.7 24.4  -2.708  0.0316
 C3C4 - C5C6   -48.30 27.4 11.8  -1.763  0.2238
 C4C5 - C5C6    23.99 26.7 24.4   0.898  0.6464

loading_magnitude = 3, loading_cycles = 1000:
 contrast    estimate   SE   df t.ratio p.value
 C3C4 - C4C5   -86.76 26.7 24.4  -3.250  0.0091
 C3C4 - C5C6   -60.09 27.4 11.8  -2.194  0.1134
 C4C5 - C5C6    26.67 26.7 24.4   0.999  0.5845

loading_magnitude = 0.3, loading_cycles = 3000:
 contrast    estimate   SE   df t.ratio p.value
 C3C4 - C4C5   -80.97 26.7 24.4  -3.033  0.0151
 C3C4 - C5C6   -47.12 27.4 11.8  -1.720  0.2386
 C4C5 - C5C6    33.86 26.7 24.4   1.268  0.4261

loading_magnitude = 1, loading_cycles = 3000:
 contrast    estimate   SE   df t.ratio p.value
 C3C4 - C4C5   -75.23 26.7 24.4  -2.818  0.0247
 C3C4 - C5C6   -43.25 27.4 11.8  -1.579  0.2923
 C4C5 - C5C6    31.98 26.7 24.4   1.198  0.4656

loading_magnitude = 3, loading_cycles = 3000:
 contrast    estimate   SE   df t.ratio p.value
 C3C4 - C4C5   -96.02 26.7 24.4  -3.597  0.0039
 C3C4 - C5C6   -64.51 27.4 11.8  -2.355  0.0866
 C4C5 - C5C6    31.51 26.7 24.4   1.180  0.4759
```

```
loading_magnitude = 0.3, loading_cycles = 5000:
 contrast    estimate   SE   df t.ratio p.value
 C3C4 - C4C5   -86.37 26.7 24.4  -3.235  0.0094
 C3C4 - C5C6   -49.60 27.4 11.8  -1.811  0.2083
 C4C5 - C5C6    36.77 26.7 24.4   1.377  0.3680

loading_magnitude = 1, loading_cycles = 5000:
 contrast    estimate   SE   df t.ratio p.value
 C3C4 - C4C5   -90.25 26.7 24.4  -3.380  0.0066
 C3C4 - C5C6   -55.80 27.4 11.8  -2.037  0.1464
 C4C5 - C5C6    34.45 26.7 24.4   1.290  0.4140

loading_magnitude = 3, loading_cycles = 5000:
 contrast    estimate   SE   df t.ratio p.value
 C3C4 - C4C5   -98.98 26.7 24.4  -3.707  0.0030
 C3C4 - C5C6   -67.76 27.4 11.8  -2.473  0.0708
 C4C5 - C5C6    31.22 26.7 24.4   1.170  0.4821
```